UNIVERSITY OF LIVERPOOL

Simultaneous Communication and Power Transfer for WBAN/WPAN Applications

by

Zhenzhen Jiang

A thesis submitted in accordance with the requirements for the award of the degree of Doctor of Philosophy of the University of Liverpool

April 2021

I would like to dedicate this thesis to you

as you complete me

Declaration

I hereby declare that except where specific reference is made to the work of others, the contents of this dissertation are original and have not been submitted in whole or in part for consideration for any other degree or qualification in this, or any other University. This dissertation is the result of my own work and includes nothing which is the outcome of work done in collaboration, except where specifically indicated in the text.

Zhenzhen Jiang

2021

Acknowledgements

I am aware that I could have just simply followed the common structure for this part, but I also have been told this I can write anything I'd like to here. Therefore, I decided to record what I had in my mind at this moment.

In the past when anyone asked me why I chose to pursue the sciences, I replied because of the scholarship. If not for Dr. Zhao Wang and Dr. Mark Leach, who recognised my potential and encouraged me, I would not have dared to think of who I could be one day. For their support during the darkest and the most difficult times, I have no words to adequately express my appreciation. It is them, who never made let me feel I do not matter or belong. It is them, who convinced me that I have the right to be exactly who I am. It is them, who let me know everything is going to be fine. And just like they said, "It is okay to be scared, we just have to keep going." They taught me a lot and it was by their example I found the courage to succeed in this exciting chapter of my life.

What I have accomplished, does not only belong to me. Nothing could be further from the truth if I say all accomplishments were mine alone. I have been encouraged, sustained, inspired, and tolerated, not only by my supervision team (Dr. Zhao Wang, Dr. Mark Leach, Prof. Eng Gee Lim, and Prof. Yi Huang), but by the greatest group of friends anyone ever had. Before I met you all, I always felt like a neutrino, destined to be alone forever. Thankfully, I was wrong. I would not be here if it weren't for some very important people in my life, beginning with my parents, my supervisors, my colleagues, and my other family (close friends), who I'm so happy and grateful to have with me throughout my life. I apologise if I haven't been the friend you deserve, but I want you to know, in my way, I LOVE YOU ALL.

For any of my colleagues or friends that are nervous about their future, know that you are not alone. Try to be brave and determined, this has helped me and will continue to do so as I navigate the next new and exciting phase of my life.

ABSTRACT

Wireless body and personal area networks have become commonplace in recent years in industrial, medical, and consumer-based applications, allowing a collection of devices such as medical sensors to be distributed around a person's body or within their direct vicinity, to communicate with each other or a network controller to provide convenient personal services. Distributed devices are typically compact and can even be located within the human body. This produces several bottlenecks relating to RF ability and power availability which are addressed here.

In this thesis, two antennas are developed. The first is designed for implantable and ingestible applications offering robust wideband performance, covering all the useable licenced operating bands, in the complex material characteristic environment of the human body. The radiation characteristics of the proposed antenna outperform other published work with a smaller size, achieved through the novel application of split-ring resonators. The second is an off-body antenna which concurrently provides appropriately polarised bands for indoor and outdoor localisation and data communication. For its minimised size and wide bandwidth, this antenna also outperforms other antennas for WPAN applications published in the literature.

Two methods for simultaneous wireless information and power transfer have been proposed in this work, based on novel theoretical ideas and hardware implementations. A symbol splitting system separates the information- and non-information- carrying components of a signal, using each for data reception and energy harvesting, respectively. The second method makes use of the characteristic of the requisite rectifier in the power conversion from RF to DC, recycling the inevitable third harmonic for data reception. The hardware required to achieve both methodologies utilise couplers and each architecture has been proven feasible through simulation and measurement. They provide comparable performance to other published systems, offering a compact, efficient, and convenient route to simultaneous wireless information and power transfer.

Contents

CHAPTER 1. Introduction 1
1.1 Research Background 1
1.2 Research Motivation 7
1.3 Aims and Objectives 10
1.4 Chapter Outline 11
1.5 References 12
CHAPTER 2. Literature Review 17
2.1 Overview of Antennas for WBAN 17
2.1.1 Implantable Antennas 18
2.1.2 Ingestible Antennas 25
2.1.3 Metamaterials for Bio-medical Applications 31
2.2 Design of Antennas for Localisation in WPAN Applications 33
2.3 Previous Studies of SWIPT 38
2.3.1 Techniques for SWIPT 40
2.3.2 RF WPT Architecture 43
2.4 Summary 46
2.5 References 48
CHAPTER 3. A Novel Compact Wideband Antenna with Split-ring Resonators for Implantable/Ingestible Applications 59
3.1 Antenna Background 60
3.2 Design Optimisation 62
3.2.1 Influence of Capsule Dimensions 66
3.2.2 Influence of Internal Batteries 67
3.2.3 Influence of Biocompatible Insulation 67
3.2.4 Influence of Different Organs 69
3.2.5 Possible usage for implants 70
3.3 Radiation Efficiencies and SAR Values 71
3.3.1 Evaluation of Gain and Radiation Efficiency 71
3.3.2 Evaluation of Specific Absorption Rate 75

3.4 Realisation and Measurements 76
3.5 Novelty 78
3.6 Summary 81
3.7 References 82
CHAPTER 4. A Compact Dual-Polarised Antenna for WPANs with Indoor/Outdoor Localisation 86
4.1 Introduction 87
4.2 Design Configuration and Working Mechanism 88
4.2.1 Antenna Design 90
4.2.2 Parametric Analysis 91
4.2.3 Circular Polarisation Mechanism 94
4.3 Realisation and Measurements 97
4.3.1 Evaluation of Return Loss 98
4.3.2 Evaluation of CP Characteristic 99
4.3.3 Evaluation of Radiation Patterns 102
4.3.4 Evaluations of Efficiency 108
4.4 Novelty 108
4.5 Summary 110
4.6 References 111
CHAPTER 5. Two Novel SWIPT Methods with Hardware Implementations 114
5.1 Introduction 115
5.2 WPT Module 117
5.2.1 Analysis of Rectifier Topologies 118
5.2.2 Design Process of Rectifier in ADS2017 120
5.3 SWIPT by Symbol-Splitting Technique 122
5.3.1 Rat-race Coupler-based IRR Topology 122
5.3.2 Mechanism of SS 124
5.3.3 Rectifier Design 126
5.4 SWIPT by Recycling Third Harmonics 127
5.4.1 Branch-line Coupler-based IRR Topology 128
5.4.2 Generation & Extraction of Third Harmonics 130
5.4.3 Viable Modulation Schemes 132
5.4.4 Rectifier Design 133

5.5 IRR Realisation and Measurements 134
5.5.1 Validation of IRR for SS Technique 134
5.5.2 IRR Realisation for Recycling Third Harmonics 139
5.6 Summary 142
5.7 References 144
CHAPTER 6. Conclusions & Future Work 148
6.1 Conclusions 148
6.2 Original Contributions 152
6.3 Future Work 155

List of Figures

Fig. 1-1: A general architecture of WBAN/WPAN in healthcare application (adapted from) [3]. 2
Fig. 1-2: WPAN device as a personal server contacts with WBAN devices around human body..... 9
Fig. 1-3: An external server contacts with both WBAN and WPAN devices. 9
Fig. 2-1: Implantable and ingestible devices for biomedical telemetry [4]. 18
Fig. 2-2: Size miniaturisation by using shorting pins and open-ended slots on the ground plane: Antenna structure in (a) [13]; (b) [14]; (c) [20]. 20
Fig. 2-3: Size miniaturisation by radiator stacking to increase radiator current paths [22]. 21
Fig. 2-4: Size miniaturisation by using stub loading and capacitive coupling [12]. 21
Fig. 2-5: Examples of bandwidth enhancement: (a) [14]; (b) [22]; (c) [23]. 23
Fig. 2-6: An example of achieving biocompatibility by coating the implantable antenna with a thin biocompatible insulating film [26]. 24
Fig. 2-7: Overview of a typical WCE operational path [49]..... 26
Fig. 2-8: Example of a capacitance-loaded embedded antenna for WCE [36]: (a) Geometry structure of the antenna; (b) Geometry structure of the WCE model; (c) Performance in different organs. 27
Fig. 2-9: Examples of embedded antenna for WCE: (a) [37]; (b) [38]..... 28
Fig. 2-10: Examples of conformal antennas placing on the inner wall of a WCE: (a) microstrip antenna [39]; (b) loop antenna [40]..... 29
Fig. 2-11: Examples of the conformal antennas with loop structure placing on the outer wall of a WCE: (a) [45]; (b) [46]. 30
Fig. 2-12: Examples of conformal antenna placing on the outer wall of a WCE: (a) helix antenna [48]; (b) PIFA antenna [49]. 31
Fig. 2-13: Example of a compact CSRR loaded CP implantable antenna: (a) antenna structure; (b) Reflection coefficients [56]. 32
Fig. 2-14: Example of a compact SRR loaded slot antenna [57]. 33
Fig. 2-15: Example of a GNSS-enabled dual-feed antenna [63]: (a) Antenna geometry; (b) Simulated AR for three different conditions; (c) Fabricated antenna and torso phantom (wearing the antenna integrated into the military beret); (d) Measured and simulated reflection coefficients. 35
Fig. 2-16: Example of a GNSS-enabled single-feed antenna [61]: (a) Antenna geometry; (b) Measured and simulated reflection coefficients; (c) Fabricated prototype; (d) Simulated and measured AR in dB. 36
Fig. 2-17: Example of a GNSS-enabled antenna with CSRR [62]: (a) Antenna geometry; (b) Fabricated prototype; (c) Measured and simulated reflection coefficients; (d) Simulated and measured AR in dB. 37
Fig. 2-18: Types of WIPT: (a) SWIPT; (b) WPCNs; (c) WPBC [68], [69]. 39

Fig. 2-19: Separated receivers technique for SWIPT [70]. 40
Fig. 2-20: TS technique for SWIPT [70]. 41
Fig. 2-21: PS technique for SWIPT [70]. 42
Fig. 2-22: AS technique for SWIPT [70]. 43
Fig. 2-23: General hardware implementation of a far-field RF WPT system [89]. 44
Fig. 2-24: Four typical impedance matching scenarios: (a) A single band rectenna; (b) A multiband rectenna with matching network and rectifying circuit per frequency band; (c) A broadband rectenna with a broadband matching network; (d) A broadband rectenna with separate matching networks for each frequency band [89]. 46
Fig. 3-1: Schematic of the optimisation process. 62
Fig. 3-2: (a) Planar design of the proposed antenna. (b) 3-D conformal model of the designed antenna (substrate colour here is set to be transparent blue for display purpose). 64
Fig. 3-3: S_{11} with and without SRRs in the simplified body phantom. 65
Fig. 3-4: Top view of the E-field distribution around the proposed antenna in the simplified body phantom at 403 MHz: (a) with SRRs, (b) without SRRs. . 65
Fig. 3-5: Effects on S_{11} with varying radii. 66
Fig. 3-6: Simulated S_{11} with internal batteries of different heights. 67
Fig. 3-7: Effects on S_{11} with different thicknesses of the coating material. 68
Fig. 3-8: Effects on S_{11} with Al_2O_3 substrate and superstrate. 69
Fig. 3-9: Effects on S_{11} with different biological tissues. 69
Fig. 3-10: Simulated S_{11} when the antenna is implanted inside the human arm. . 71
Fig. 3-11: Gustav voxel body model for CST anatomical simulations. 72
Fig. 3-12: Simulated 2-D patterns of the proposed antenna over *E-plane* and *H-plane* at (a) 403 MHz; (b) 433 MHz in the small intestine; (c) 2.45 GHz in the arm. 73
Fig. 3-13: (a) Photograph of the fabricated superstrate and antenna (b) Measurement of the proposed antenna in the tissue-simulating liquid. 77
Fig. 3-14: Measured and simulated S_{11} of the proposed antenna. 78
Fig. 4-1: Evolution of the proposed structure: from (a) an elliptical cross dipole to (b) a modified multi-loop dipole. 89
Fig. 4-2: Simulated S_{11} of the reference antenna and the proposed antenna. 89
Fig. 4-3: Geometry of the proposed antenna: (a) top view with feeding structure; (b) bottom view; (c) side view; (d) 3-D view. 90
Fig. 4-4: Effects on S_{11} with different values of w_1. 92
Fig. 4-5: Effects on S_{11} with different values of w_2 and w_3. 93
Fig. 4-6: Effects on S_{11} with different values of w_6. 93
Fig. 4-7: Effects on S_{11} with different values of *gap*. 94
Fig. 4-8: Surface current distribution on the top side of the proposed antenna at 1.57 GHz at (a) 0°, (b) 90°, (c) 180°, and (d) 270°. 95

Fig. 4-9: Surface current distribution on the bottom side of the proposed antenna at 1.57 GHz at (a) 0°, (b) 90°, (c) 180°, and (d) 270°. 96
Fig. 4-10: Performance of simulated AR at 1570 MHz. 97
Fig. 4-11: Bottom and top views of the manufactured prototypes. 97
Fig. 4-12: S_{11} measurement setup of the proposed antenna. 98
Fig. 4-13: Simulated and measured S_{11} of the proposed design. 99
Fig. 4-14: (a) Schematic of the measurement setup; (b) AUT placed at 0°; and (c) AUT placed at 90°. 100
Fig. 4-15: Measured $|S_{21}|$ when placing the AUT at 0° and 90° and their differences. 101
Fig. 4-16: Measured and simulated AR. 101
Fig. 4-17: Schematic of the measurement setup. 102
Fig. 4-18: Measurement setup in the anechoic chamber: (a) place the AUT at two positions P_1 and P_2; (b) place the transmitting horn at two positions H_1 and V_1. 103
Fig. 4-19: 3D simulated radiation pattern and 2D simulated and measured radiation patterns over (a) *xoz* plane at 1.40 GHz, (b) *yoz* plane at 1.40 GHz. 104
Fig. 4-20: Simulated and measured radiation patterns over (a) *xoz* plane at 1.17 GHz, (b) *yoz* plane at 1.17 GHz, (c) *xoz* plane at 1.57 GHz, (d) *yoz* plane at 1.57 GHz, (e) *xoz* plane at 2.40 GHz, and (f) *yoz* plane at 2.40 GHz. 105
Fig. 4-21: Measurement setup in the anechoic chamber with the proposed antenna used as transmitter and receiver. 106
Fig. 4-22: Simulated radiation patterns at 1.57 GHz (a) on *xoz* plane, (b) on *yoz* plane; Measured radiation pattern at 1.57 GHz (c) when the received antenna places at P_1, (d) when the received antenna places at P_2. 107
Fig. 4-23: Simulated total efficiency of the proposed antenna. 108
Fig. 5-1: Splitting techniques for SWIPT: (a) time switching; (b) power splitting; (c) antenna switching; (d) frequency splitting. 116
Fig. 5-2: General structure of a WPT receiver [20]. 117
Fig. 5-3: Configuration of a conventional single series diode topology. 118
Fig. 5-4: Configuration of a bridge rectifying circuit. 119
Fig. 5-5: Configuration of a voltage doubler rectifying circuit. 119
Fig. 5-6: Configuration of a full-wave Greinacher rectifying circuit. 120
Fig. 5-7: Schematic of the proposed topology with a rat-race coupler. 123
Fig. 5-8: Simulated *S*-parameters of the rat-race coupler designed on RT/Duroid 5880: (a) magnitudes of S_{11}, S_{21}, S_{31}, S_{41}, S_{44} and (b) phases of S_{21}, S_{31}. 124
Fig. 5-9: Frequency response of (a) base signal; (b) carrier signal; (c) modulated BPSK signal [28]. 126
Fig. 5-10: Layout of the rectifying circuit. 127

Fig. 5-11: Block diagram of the proposed IRR topology based on a branch-line coupler. 128
Fig. 5-12: Simulated *S*-parameters of a branch-line coupler designed on RT/Duroid 5880: (a) magnitudes of S_{11}, S_{21}, S_{31}, S_{41}, S_{44} and (b) phases of S_{21}, S_{31}. 130
Fig. 5-13: Layout of the rectifying circuit for the proposed system. 133
Fig. 5-14: Topology and fabricated prototype of the proposed IRR system. 134
Fig. 5-15: Realisation of experimental validation setup with the fabricated prototype. 135
Fig. 5-16: Voltage waveforms of the (a) simulated base signal, (b) simulated transmitted signal, (c) simulated incoming signal at ports P_2 & P_3, (d) simulated output signal from port P_4 and (e) measured output signal from port P_4 within 20 ns. 136
Fig. 5-17: Simulated and measured PCEs versus input power level for CW case. 137
Fig. 5-18: Measured PCEs versus input power level and three data rates for BPSK cases. 137
Fig. 5-19: fabricated prototype of the proposed IRR system. 139
Fig. 5-20: Measurement setup of the fabricated system for validation. 140
Fig. 5-21: Measured voltage waveforms of (a) the incoming signal and (b) the third harmonic in a transient period. 141
Fig. 5-22: Measured and simulated PCE at three input power levels. 141
Fig. 5-23: Simulated and measured PCE vs. CW at varying input power levels. 142

List of Tables

Table 1-1: Licensed Frequency Bands for Implantable/Ingestible Antenna 4
Table 1-2: Allocated GNSS Frequency Bands for Localisation.....6
Table 2-1: Summary of Published Research on Optimisations of an RF WPT System.....44
Table 3-1: Optimised Antenna Dimensions (Millimetre).....64
Table 3-2: Radiation Efficiency and Realised Gain with and Without SRRs 74
Table 3-3: SAR Values for the Proposed Antenna.....76
Table 3-4: Recipes for the Tissue-Simulating Liquids 77
Table 3-5: Comparisons of the Proposed Antenna with Other Metamaterial Work 79
Table 3-6: Comparisons of the Proposed Antenna with Other Work.....80
Table 4-1: Optimised Dimensions of the Proposed Antenna (Millimetre).....91
Table 4-2: HPBW of the Proposed Antenna at Desired Frequency.....106
Table 4-3: Comparisons of the Proposed Antenna with Other Work.....109
Table 5-1: Optimised Circuit Dimensions (Millimetre) 127
Table 5-2: Optimised Circuit Dimensions (Millimetre) 133
Table 5-3: Relation of PCEs versus R_b with the same Input Power Level 138
Table 5-4: Comparison with Other Published SWIPT Systems 138

Acronyms

ADS	Advanced Design System
AR	Axial Ratio
ARBW	Axial Ratio Beamwidth
ARSK	Amplitude Ratio Shift Keying
AS	Antenna Switching
ASK	Amplitude Shift Keying
AUT	Antenna Under Test
AVG SAR	Averaged SAR
BANs	Body Area Networks
BPSK	Binary Phase Shift Keying
CP	Circular Polarisation
CPBW	Circular Polarisation Beamwidth
CSRR	Complementary Split-Ring Resonator
CST	Computer Simulation Technology
CW	Continuous Wave
DC	Direct Current
ECG	Electrocardiogram
EEG	Electroencephalography
E-field	Electric Field
EH	Energy Harvesting
EM	Electromagnetic
EMG	Electromyography
ETSI	European Telecommunications Standards Institute
FCC	Federal Communications Commission
FFT	Fast Fourier Transform
FS	Frequency Splitting

GI	Gastrointestinal
GNSS	Global Navigation Satellite Systems
GPS	Global Positioning System
HB	Harmonic Balance
HPBW	Half Power Beamwidth
ID	Information Detection
IEEE	Institute of Electrical and Electronics Engineers
IR	Integrated Receiver
IRR	Integrated Rectifier-Receiver
ISM	Industrial Scientific Medical
LED	Light Emitting Diode
LHCP	Left Hand Circular Polarisation
LP	Linear Polarisation
LSSP	Large Signal S-Parameter
MedRadio	Medical Device Radio Communication
MICS	Medical Implant Communication Service
PANs	Personal Area Network
PC	Personal Computer
PCB	Printed Circuit Board
PCE	Power Conversion Efficiency
PEC	Perfect Electric Conductor
PEEK	Polyether Ether Ketone
PIFA	Planar Inverted-F Antenna
PS	Power Splitting
PT	Power Transferring
RF	Radio Frequency
RHCP	Right Hand Circular Polarisation
RX	Receiving Antenna

SAR	Specific Absorption Rate
SMA	Subminiature Version A
SMD	Surface-Mount Device
SRR	Split-Ring Resonators
SS	Symbol-Splitting
SWIPT	Simultaneous Wireless Information and Power Transfer
TS	Time Switching
TX	Transmitting Antenna
VNA	Vector Network Analyser
WBAN	Wireless Body Area Network
WCE	Wireless Capsule Endoscope
WiFi	Wireless Fidelity
WIPT	Wireless Information and Power Transfer
WMTS	Wireless Medical Telemetry Service
WPAN	Wireless Personal Area Network
WPBC	Wirelessly Powered Backscatter Communication
WPCN	Wirelessly Powered Communication Network
WPT	Wireless Power Transfer
WSN	Wireless Sensor Network

List of Publications

Journal Publications

[1] **Z. Jiang**, Z. Wang, M. Leach, E. G. Lim, H. Zhang, R. Pei, and Y. Huang, “Symbol-splitting-based simultaneous wireless information and power transfer system for WPAN applications,” in *IEEE Microw. and Wireless Compon. Lett.*, vol. 30, no. 7, pp. 713–716, Jul. 2020.

[2] **Z. Jiang,** Z. Wang, M. Leach, Y. Huang, E. G. Lim, J. Wang, and R. Pei, "Wideband loop antenna with split ring resonators for wireless medical telemetry," in *IEEE Antennas Wireless Propag. Lett.*, vol. 18, pp. 1415–1419, Jul. 2019.

[3] J. Wang, M. Leach, E. G. Lim, Z. Wang, **Z. Jiang**, R. Pei, and Y. Huang, "A conformal split-ring loop as a self-resonator for wireless power transfer," in *IEEE Access*, vol. 8, pp. 911-919, 2019, doi: 10.1109/ACCESS.2019.2918640.

[4] R. Pei, M. Leach, E. G. Lim, Z. Wang, J. Wang, Y. Wang, **Z. Jiang**, and Y. Huang, "Wearable belt antenna for body communication networks," in *IEEE Antennas Wireless Propag. Lett.*, vol. 19, no. 12, pp. 2043–2047, Sept. 2020.

[5] R. Pei, M. Leach, E. G. Lim, Z. Wang, C. Song, J. Wang, W. Zhang, **Z. Jiang**, and Y. Huang, "Wearable EBG-backed belt antenna for smart on-body applications," in *IEEE Trans. Industrial Informatics*, vol. 16, pp. 7177–7189, Nov. 2020.

Conference Publications

[1] **Z. Jiang**, Z. Wang, M. Leach, E. G. Lim, H. Zhang, and Y. Huang, “Simultaneous wireless power transfer and communications by recycling third harmonics for WPAN applications,” in *2020 IEEE MTT-S International Microwave Workshop Series on Advanced Materials and Processes for RF and THz Applications (IMWS-AMP)*, Jul. 2020. DOI: 10.1109/IMWS-AMP49156.2020.9199669.

[2] **Z. Jiang**, Z. Wang, M. Leach, E. G. Lim, and Y. Huang, “Modelling and performance analysis of an efficient compact integrated rectifier-receiver for SWIPT,” in *2020 IEEE MTT-S International Microwave Workshop Series on Advanced Materials and Processes for RF and THz Applications (IMWS-AMP)*, Jul. 2020. DOI: 10.1109/IMWS-AMP49156.2020.9199660.

[3] J. Wang, E. G. Lim, M. Leach, Z. Wang, R. Pei, **Z. Jiang**, and Y. Huang, "Design of an implantable antenna for wireless communication of ingestible capsule endoscope," in *2019 International Symposium on Antennas and Propagation (ISAP)*, Oct. 2019.

[4] Z. Wang, H. Zhang, **Z. Jiang**, M. Leach, J. Wang, K. Man, and E. G. Lim, " A multiband rectenna for self-sustainable devices," in *2018 International SoC Design Conference (ISOCC)*, Nov. 2018. DOI: 10.1109/ISOCC.2018.8649903.

[5] Y. Shi, **Z. Jiang**, S. Lam, M. Leach, J. Wang, and E. G. Lim, "Multi-GHz microstrip transmission lines realised by screen printing on flexible substrates," in *2017 IEEE Electrical Design of Advanced Packaging and Systems Symposium (EDAPS)*, Dec. 2017. DOI: 10.1109/EDAPS.2017.8277038.

CHAPTER 1. INTRODUCTION

This thesis contains a body of research which aims to produce novel enabling technologies that lead to improvements in the delivery of wireless communication and power transfer for devices operating in body and personal area networks. This begins with a realisation of the challenges in the field and the derivation of research questions through an analysis of the required theoretical background and current state of the art in the research and industrial environments. These questions bring about the formulation of novel solutions through a rigorous research and development process, leading to a robust set of conclusions. The thesis sees the development of antennas able to support such systems and the formation of a novel hardware receiver implementation.

This chapter sets out the research motivation by providing background to the area of study, allowing the derivation of a clear set of aims and objectives, which steer the focus of the work. An overview of the thesis content is also provided at the end of this chapter.

1.1 Research Background

Body area networks (BANs) and personal area network (PANs), as key elements in body-centric communications, have attracted a growing level of research interest in recent years together with the boom in the number and types of wireless body sensors [1]. Generally, a BAN represents a short-range low power network operating in the direct vicinity of, or inside of, the human body; connecting implantable or wearable devices that collect bio or other personal information from the person [2]. In contrast to a BAN, a PAN normally refers to a network with portable sensors or devices located around an individual within a wider coverage area (e.g., inside a room). Apart from the extended coverage, applications involved in a PAN system often not only monitor physiological changes collected from the human body but also provide information about the user's surroundings or environment. To offer a smart, user-friendly, and ergonomic technology to the user, wireless communications and related technologies

have been adopted in the implementation of these networks, which has moved the general trend towards wireless BAN (WBAN) and wireless PAN (WPAN). The main benefit of WBAN and WPAN is that dynamic networks can be realised, allowing users to add or remove any sensors or devices freely. Accordingly, the growth in potential applications in the fields of WBAN and WPAN such as healthcare, monitoring and position tracking has developed rapidly. Fig. 1-1 shows a generalised architecture of a WBAN/WPAN for healthcare application.

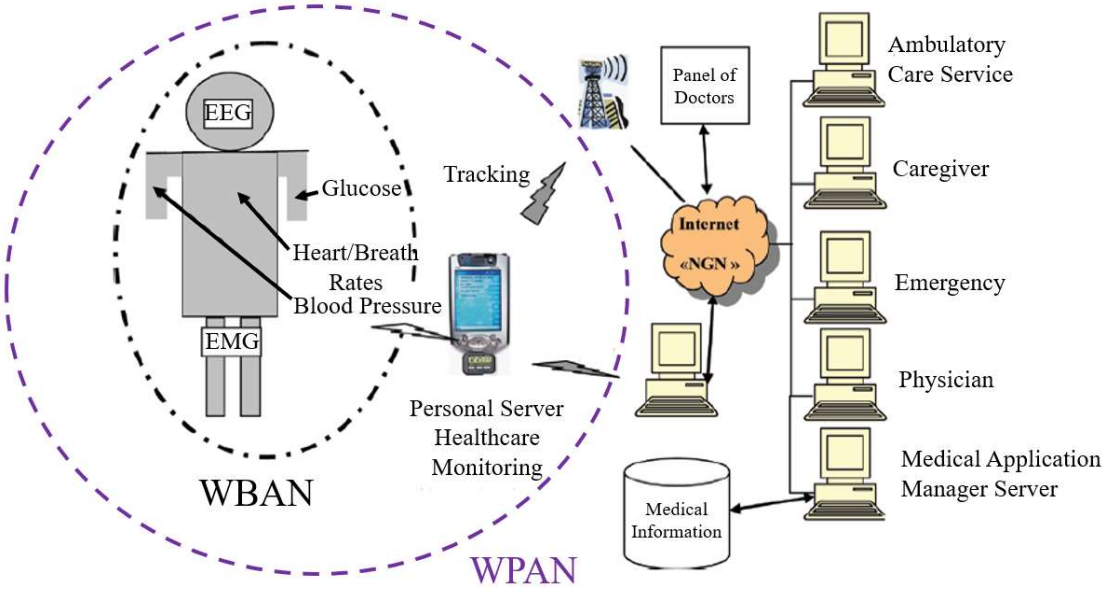

Fig. 1-1: A general architecture of WBAN/WPAN in healthcare application (adapted from) [3].

Among the abovementioned applications, research on biomedical telemetry has become intensive due to its importance for treatment and healthcare in the WBAN domain. Implanted or ingestible sensors can sense and collect vital bio-signals such as temperature, heart activity (electrocardiogram (ECG) sensor), muscle activity (electromyography (EMG) sensor), brain electrical activity (electroencephalography (EEG) sensor), blood pressure and blood glucose level from the human body and transmit the collected information to an external device for further post-processing by a medical expert, potentially in real-time. This application could allow medical emergencies or other time-critical health issues such as stroke, heart attack or even

cancer to be detected and diagnosed as early as possible [4]. In any wireless system, the antenna is a key component. In the cases of WBAN and WPAN, an antenna must be able to transmit and receive signals wirelessly between implantable or ingestible sensors and external devices. A well-designed implantable or ingestible antenna helps to reduce the overall system size and establish a robust wireless communication link. To achieve these goals the following five aspects should be carefully considered:

1. Operating frequency band:

Currently, frequency bands allocated for use in implantable and ingestible applications include the Medical Implant Communication Service (MICS) band, Medical Device Radio Communication (MedRadio) band, Wireless Medical Telemetry Services (WMTS) band, and some of the Industrial Scientific Medical (ISM) bands. These bands are allocated and regulated by the U.S. Federal Communications Commission (FCC) and the European Telecommunications Standards Institute (ETSI). The frequency range of each band is provided in Table 1-1. Among them, MICS 403 MHz is commonly used for low-power communication to support diagnostic or therapeutic operations associated with medical implant devices [5] and ISM 433 MHz is mainly used for wireless power transfer from external sources to implant devices [6]. ISM 2450 MHz is commonly used when size restrictions are paramount to the system such as for a retinal implant, as typically, lower frequency leads to larger antenna size. Conversely, using higher frequency bands results in larger signal attenuation by body tissues [7]. Thus, the selection of an appropriate frequency band for any implantable or ingestible device requires careful consideration.

Table 1-1: Licensed Frequency Bands for Implantable/Ingestible Antenna

	Frequency Band Full Name	**Range (MHz)**
MICS	Medical Implant Communication Service	402~405
MedRadio	Medical Device Radio Communication	401~406 413~419 426~432 438~444 451~457
WMTS	Wireless Medical Telemetry Services	1395~1400
ISM	Industrial Scientific Medical	433.1~434.8 868.0~868.8 902.8~928.0 2400~2480

2. Operating bandwidth:

Distinct from free space, the environment inside a human body is more complex as it is composed of a variety of non-uniform body tissues such as skin, fat, and muscle. These tissues have different material properties (e.g., dielectric constant and conductivity), which vary with frequency and are distributed asymmetrically. The consequent influence such as attenuation inside a tissue layer and reflection among different tissues can result in operating frequency shifts, due to antenna detuning and further losses [8]. Therefore, an antenna's operating bandwidth should be sufficiently wide to compensate to some extent for these influences from the human body.

3. Size miniaturisation:

Physical limitations such as weight and size for implantable and ingestible antennas provides a significant challenge to the antenna designer. Generally, resonating at a

lower frequency requires a larger size [9]. For example, the wavelength at 403 MHz in free space is 744 mm, typically an antenna has dimensions on the order of half/quarter a wavelength and hence an antenna in this case with a size on the order of several hundred mm would be physically beyond the tolerable size for an implantable or ingestible antenna. Even finding sufficient and convenient space for such an antenna on-body would be difficult, hence, miniaturisation is necessary. The relatively high dielectric coefficients of human body tissues, aid in reducing overall antenna size, however, the high conductivity of the human body results in a significant drop in radiation efficiency and hence antenna gain [10]. Therefore, a trade-off between size, radiation efficiency, and gain needs to be considered.

4. Biocompatibility:

To avoid direct contact between an implant and body tissues, appropriate biological properties are required. Two methods have been employed in the literature: the first is to use biocompatible conductors such as Titanium, silver palladium and gold [11]; the second is to use a thin biocompatible insulating film wrapped around the antenna such as polyamide, zirconia, ceramic alumina, and polyether ether ketone (PEEK) [12]-[15]. The latter method is cheaper and offers comparable performance to the former.

5. Adherence to safety regulations:

Specific absorption rate (SAR) is a measure of how much energy is absorbed by the human body [16]. Implantable and ingestible antennas are required to follow SAR standards to avoid hazardous heating of body tissues. Two international standards have been generated to regulate SAR levels by the Institute of Electrical and Electronics Engineers (IEEE). According to IEEE C95.1-1999 standard, averaged SAR (AVG SAR) over 1 g of body tissue in the shape of a cube (1 g-AVG SAR) is limited to less than 1.6 W/kg [17]. Another standard called IEEE C95.1-2005 restricts the averaged SAR over 10 g of body tissue in the shape of a cube (10 g-AVG SAR) to less than 2 W/kg [18]. Designs of antennas to be applied on or within the human body must satisfy these standards.

Different from WBAN applications, WPAN applications integrate healthcare monitoring and location tracking. They collect not only the bio-information from the body but also the environment of the user. Such implementation has a great potential capability for long-term patient monitoring, localisation, and rescue [19]. For example, doctors or carers can easily monitor their recipients' or their patients' health situations and can help to guide or locate them if they get lost. As a result of these merits, recently there has been an upsurge in the development of devices able to provide both indoor and outdoor localisation functions using a single antenna [20], [21]. These devices make use of the allocated Global Navigation Satellite Systems (GNSS); the commonly used bands for localisation are summarised in Table 1-2.

Table 1-2: Allocated GNSS Frequency Bands for Localisation

	Frequency Band Full Name	**Range (MHz)**
GPS	Global Positioning System	L1:1575 L2: 1230 (military) L5: 1175
Galileo	European Galileo	E1: 1575 E5: 1191 E6: 1279
Beidou	Chinese Beidou	B1-2: 1589

Considering batteries are commonly used by distributed sensors like those used in WBAN/WPAN applications, as well as in a variety of other transceivers, the integration of energy harvesting technologies into wireless communication networks to extend battery life has become a new technology paradigm. A promising energy harvesting technology is wireless power transfer (WPT), by which the receivers harvest energy from electromagnetic (EM) radiation provided by a dedicated source in a fully controlled manner. The combination of communication system and wireless power

transfer is referred to as simultaneous wireless information and power transfer (SWIPT). It represents a compact approach to providing power and transmitting information to distributed sensors or other independently powered communication devices concurrently [22]-[24]. It helps with charging the main power elements in a distributed sensor or device (such as a battery) or even providing adequate energy to drive the whole system standalone. For example, wireless implants can be calibrated and powered simultaneously with the same received waves, eliminating the need for regular battery replacements. In the case of an implantable medical device, this would mean avoiding surgical operation for patients, potential infection risks, saving expenses, and improving user convenience/experience. Therefore, applications in WBAN/WPAN areas could become self-sustainable with integrated information and power transfer.

1.2 Research Motivation

This research is focussed on the development of enabling technologies for WBAN and WPAN communication and power transfer. For WBAN applications, biomedical telemetry plays a role in improving the quality of diagnosis and healthcare. Implantable and ingestible antennas as key components have been researched for years. However, none of the published designs satisfies all of the five requirements using a single radiation structure as the antenna for both implantable and ingestible devices discussed above with robust performance. For example, the conformal patch antenna proposed in [25] is of very narrow bandwidth, centred at 1.2 GHz, which suffers frequency detuning after implantation in an in vivo environment. Designs in [26], [27] achieve small size, however, the radiation efficiencies and gains are relatively low in an anatomical body model. Therefore, designing a flexible antenna that covers multi-bands with adequate bandwidth and good radiation performance for both implantable and ingestible devices is of interest.

For WPAN applications, there is a trend in designing antennas able to provide indoor/outdoor location tracking functionality. Published designs in [20], [21] show a dual-band characteristic (1.575 GHz and 2.45 GHz) for indoor/outdoor localisation.

The operational bandwidths in [20] are 1.84% (29 MHz) at 1.575 GHz and 0.736% (17 MHz) at 2.45 GHz, which are relatively narrow and fail to satisfy typical modern communication system bandwidth requirements. Polarisation characteristics should also be considered. Localisation-enabled applications typically transmit and receive circular-polarised (CP) signals as CP waves are not sensitive to the influences of Faraday rotation introduced by the ionosphere [28], [29]. Some designs, such as the one described in [30], provide sufficient bandwidth but with linear polarisation (LP). Furthermore, the provision of an additional frequency band that can be used to provide the wireless communication link used in WBAN/WPAN has been neglected by these studies.

Implementing a SWIPT system for WBAN and WPAN applications requires consideration of both information detecting/decoding (ID) and power transferring (PT) as the electromagnetic energy received by the antenna is used for both decoding information as well as harvesting energy to power the device. Popular techniques proposed for SWIPT function by separating the received signal into two streams in a variety of different domains: time, power, frequency, and antenna [31]-[35]. Common drawbacks of these techniques are an inevitable loss of information or available power. In addition, although much research on this topic has been published, the majority of the focus is on system algorithm optimisation rather than hardware implementation [33], [39]. Therefore, there is a need to develop hardware implementations that achieve the information transmission and power transfer concurrently with less information and power loss.

Two possible scenarios of this work are given in Fig. 1-2 and Fig. 1-3. The first system scenario is using a WPAN device as the personal server, which transmits data and power to other WBAN/WPAN devices (utilising SWIPT). Meanwhile, providing indoor and outdoor localisation functionality. The distributed sensors within the WBAN/WPAN network can work as SWIPT receivers as well as transmitting collected data from, for example the human body, to the personal server for further processing.

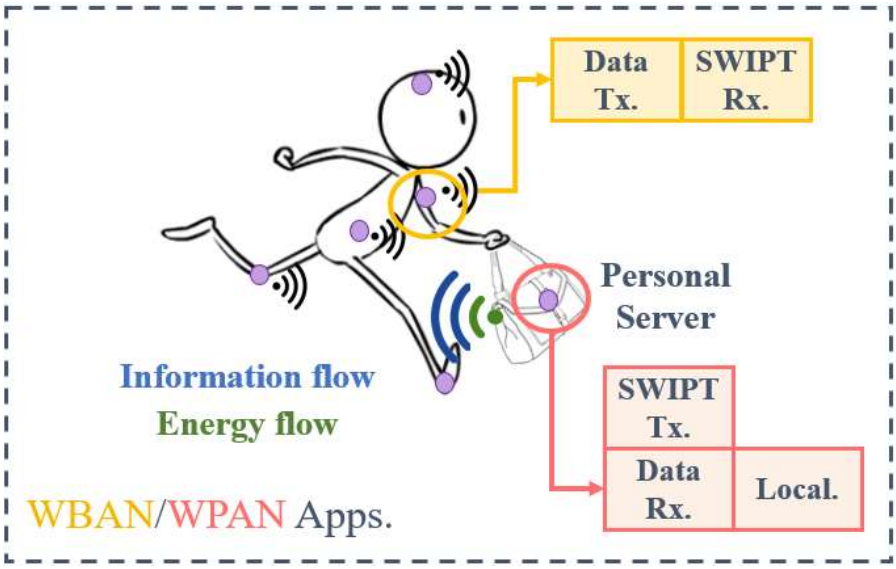

Fig. 1-2: WPAN device as a personal server contacts with WBAN devices around human body.

Another system scenario would be where both WBAN and WPAN devices are controlled by an external personal server, such as a mobile phone. In this case both devices receive data and power from the server, and can transmit collected information to the server for processing. In the case of a WPAN device, this may also provide localisation information to the network server.

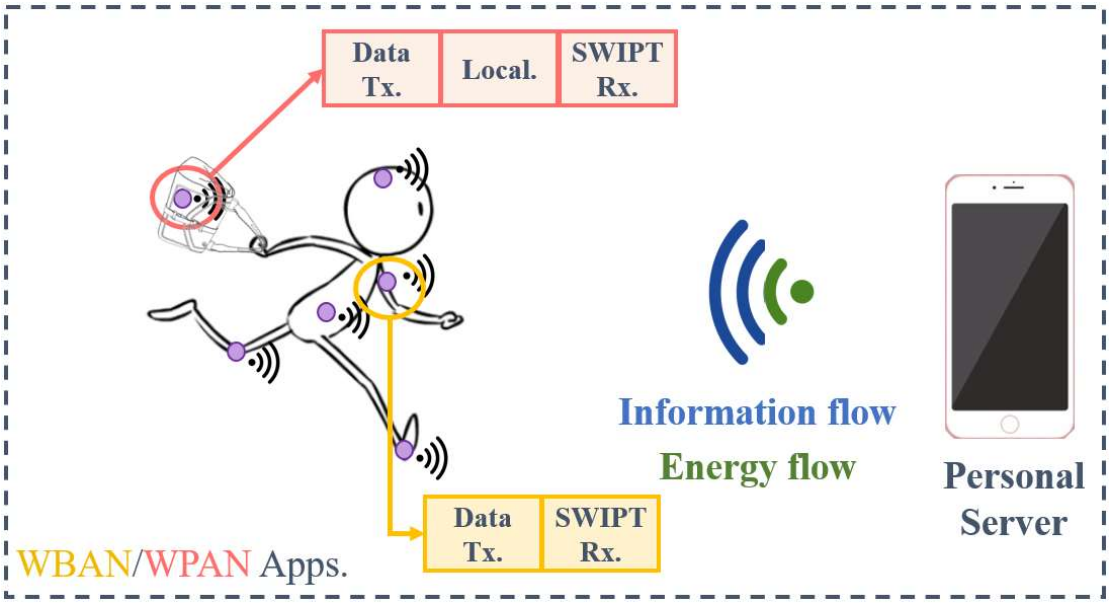

Fig. 1-3: An external server contacts with both WBAN and WPAN devices.

1.3 Aims and Objectives

The main targets of this work relate to the development of SWIPT enabling technologies for WBAN/WPAN applications. The two primary aims are: firstly, to develop novel antenna designs to meet the outcomes of a needs analysis for WBAN/WPAN antennas, and secondly, to design and implement a novel receiver hardware system capable of facilitating SWIPT functionality. To address these aims the following six objectives have been formulated to provide a structured approach to this research:

1) Develop a foundation for implantable/ingestible antennas, antennas equipped with GPS capability, and current techniques used for SWIPT, through researching the current state-of-art to determine present limitations: Chapter 2.

2) Develop a flexible implantable/ingestible antenna that can operate over multiple bands of interest with good radiation performance. This multi-band or broadband antenna should take into consideration of size miniaturisation, detuning desensitisation for the body environment (through bandwidth enhancement), biocompatibility, and user safety: Chapter 3.

3) Develop a compact multiband antenna that can be used for indoor/outdoor localisation and medical telemetry services. Polarisation should be designed carefully to allow CP waves to be received for tracking: Chapter 4.

4) Develop novel hardware-based splitting techniques for simultaneous communication and power transfer while minimising information and power loss: Chapter 5.

5) Provide critical analysis and comparison of simulation and experimental results with an understanding of error sources, together with comparisons with other state of the art works: Chapter 3, 4, and 5.

6) To critically analyse the outcomes of this research and provide suggestions for further work: Chapter 6.

1.4 Chapter Outline

This thesis includes six chapters with the main research contributions provided through the design of two novel antennas optimised for WBAN/WPAN applications and the development of novel splitting mechanisms for SWIPT applications achieved through a hardware implementation. The structure is outlined in the following:

Chapter 2 – Presents an overview of the developments of implantable/ingestible antennas, GPS-equipped WBAN/WPAN antennas, and SWIPT technologies, with a detailed literature review of previous work and the state of the art in similar areas.

Chapter 3 – A wideband flexible antenna with split-ring resonators is presented for implantable and capsule applications in the WBAN domain. This design covers the entire MedRadio band and four ISM bands of interest. The novelty of adopting a split-ring resonator is analysed to elaborate how it helps with impedance matching, radiation gain and efficiency. The proposed antenna in this chapter is the first published work that can offer appropriate radiation performance in both muscle-located implantation and ingestible environment.

Chapter 4 – A novel compact wideband dual-polarised antenna with Indoor/outdoor localisation capabilities for WPAN communications is proposed in this chapter. This antenna has a comparably wide impedance bandwidth covering the GNSS L1/E1, GPS L5, WMTS, and the ISM 2450 MHz bands. Different from most published designs, the CP property is enabled in the GNSS L1/E1, GPS L5, and the ISM 2450 MHz bands for indoor and outdoor localisation.

Chapter 5 – Novel splitting techniques for SWIPT are presented, and two hardware implementations are designed and constructed. A proposed Symbol-Splitting technique aims at separating the information carrying received signal components from the non-information carrying components for data extraction and energy harvesting. Another technique utilises the typically rejected or supressed third harmonic generated by the rectifier necessary for energy harvesting to provide a route to the signal data

demodulation. The hardware implementations of the two proposed techniques are achieved through the utilisation of two common RF components and traditional phase shift keying (PSK) modulation, a commonly used modulation scheme for WBAN/WPAN, is employed for verification of the functionality. These methods reduce information loss and sustain relatively high-power conversion efficiencies for energy harvesting.

Chapter 6 – Provides conclusions in view of the research aims and objectives and highlights some ideas for further development and improvement related to this research topic.

1.5 References

[1] P. Hall, "Antennas and propagation for body-centric wireless communication," *Artech*, 2006. Doi: 10.1109/MAP.2008.4562277.

[2] M. Patel and J. Wang, "Applications, challenges, and perspective in emerging body area networking technologies," in *IEEE Wireless Commun.*, vol. 17, no. 1, pp. 80-88, Feb. 2010.

[3] J. Rodrigues, "Digital advances in medicine, e-health, and communication technologies," *Hershey, PA: IGI Global*, 2013. Doi:10.4018/978-1-4666-2794-9.

[4] F. Merli, "Implantable antennas for biomedical applications," Ph.D .dissertation, Dept. Elect. Eng., EPFL Univ., Lausanne, Switzerland, 2011.

[5] S. Parajuli and R. K. Budhathoki, "A review of medical implants communication in body area network," in *2019 IEEE 2nd International Conference on Electronics and Communication Engineering (ICECE)*, Dec. 2019.

[6] A. W. Damaj *et.al*, "Implantable antennas for biomedical applications: an overview on alternative antenna design methods and challenges," in *2018 International Conference on High Performance Computing & Simulation (HPCS)*, Jul. 2018.

[7] N. A. Malik, P. Sant, T. Ajmal, and M. U. Rehman, “A review of in-body biotelemetry devices: implantables, ingestibles, and injectables,” in *IEEE Journal Electromagnetics, RF and Microwaves in Medicine and Biology*, vol. 5, no. 1, pp. 84–96, Mar. 2021.

[8] A. Kiourti and K. S. Nikita, “A review of in-body biotelemetry devices: implantables, ingestibles, and injectables,” in *IEEE Trans. Biomedical Eng.*, vol. 64, no. 7, pp. 1422–1430, Feb. 2017.

[9] A. Kiourti and K. S. Nikita, “A review of implantable patch antennas for biomedical telemetry: challenges and solution,” in *IEEE Antennas Propag. Mag.*, vol. 54, no. 3, pp. 210-228, Aug. 2012.

[10] S. Gabriel, R. W. Lau, and C. Gabriel, “The dielectric properties of biological tissues: parametric models for the dielectric spectrum of tissues,” in *Physics in Medicine and Biology*, vol. 41, pp. 2271-2293, November 1996.

[11] R. Alrawashdeh, “Implantable antennas for biomedical applications,” Ph.D. dissertation, Department of Electrical Engineering, Univ. of Liverpool, Liverpool, UK, 2015.

[12] R. Warty, M.-R. Tofighi, U. Kawoos, and A. Rosen, “Characterization of implantable antennas for intracranial pressure monitoring: Reflection by and transmission through a scalp phantom,” in *IEEE Trans. Microw. Theory and Techn.*, vol. 56, no. 10, pp. 2366–2376, Oct. 2008.

[13] P. Soontornpipit, C. M. Furse, and Y. C. Chung, “Design of implantable microstrip antenna for communication with medical implants,” in *IEEE Trans on Microw. Theory and Techniques*, vol. 52, no. 8, pp. 1944-1951, Aug. 2004.

[14] A. K. Skrivervik, and F. Merli, “Design strategies for implantable antennas,” in *Proceedings of the Antennas and Propagation Conference*, Loughborough, UK, Nov. 2011.

[15] J. Abadia, F. Merli, J. F. Zurcher, J. R. Mosig, and A. K. Skrivervik, “3D spiral small antenna design and realization for biomedical telemetry in the MICS band,” in *Radio engineering*, vol.18, no. 4, pp. 359-367, Dec. 2009.

[16] R. Moore, “Effects of a surrounding conducting medium on antenna analysis,” in *IEEE Trans. Antennas Propag.*, vol. 11, no. 3, pp. 216–225, May 1963.

[17] IEEE Standard for Safety Levels with Respect to Human Exposure to Radio Frequency Electromagnetic Fields, 3 kHz to 300 GHz, IEEE Standard C95. 1-1999, 1999.

[18] IEEE Standard for Safety Levels with respect to Human Exposure to Radio Frequency Electromagnetic Fields, 3KHz to 300 GHz, IEEE Standard C95. 1-2005, 2005.

[19] N. F. M. Aun, P. J. Soh, A. A. Al-Hadi, M. F. Jamlos, G. A. E. Vandenbosch, and D. Schreurs, “Revolutionizing wearables for 5G: 5G technologies: Recent developments and future perspectives for wearable devices and antennas,” in *IEEE Microw. Mag.*, vol. 18, no. 3, pp. 108-124, May 2017.

[20] K. N. Paracha, S. K. A. Rahim, P. J. Soh, M. R. Kamarudin, K.-G. Tan, Y. C. Lo, and M. T. Islam, “A low profile, dual-band, dual polarised antenna for Indoor/Outdoor wearable application,” in *IEEE Access*, vol. 7, pp. 33277-33288, 2019.

[21] R. Joshi, *et.al*, “Dual-band, dual-sense textile antenna with AMC backing for localization using GPS and WBAN/WLAN,” in *IEEE Access*, vol. 8, pp. 89468-89478, 2020.

[22] Y. Yao *et.al*, “Analysis, design, and implementation of a wireless power and information transmission system using capacitive coupling and double-sided LCC compensation topology,” in *IEEE Trans. Industry Applications*, vol. 55, no. 1, pp. 541–551, Jan. 2019.

[23] J. Hirai, T.-W. Kim, and A. Kawamura, “Wireless transmission of power and information and information for cableless linear motor drive,” in *IEEE Trans. Power Electron.*, vol. 15, no. 1, pp. 21–27, Jan. 2000.

[24] X. Zhou, R. Zhang, and C. K. Ho, “Wireless information and power transfer in multiuser OFDM systems,” in *IEEE Trans. Wireless Communications.*, vol. 13, no. 4, pp. 2282–2294, Apr. 2014.

[25] S. M. Asif *et.al.*, “Design and in vivo test of a batteryless and fully wireless implantable asynchronous pacing system,” in *IEEE Trans. Biomedl Eng.*, vol. 63, pp. 1070–1081, Sept. 2016.

[26] A. Kiourti and K. Nikita, “Miniature scalp-implantable antennas for telemetry in the MICS and ISM bands: Design, safety considerations and link budget analysis,” in *IEEE Trans. Antennas Propagat.*, vol. 60, no. 8, pp. 3568-3575, Aug. 2012.

[27] M. Asili, R. Green, S. Seran, and E. Topsakal, “A small implantable antenna for MedRadio and ISM Bands,” in *IEEE Antennas and Wireless Propagat. Lett.*, vol. 11, pp. 1683 – 1685, Jan. 2013.

[28] E. K. Kaivanto, M. Berg, E. Salonen, and P. D. Maagt, “Wearable circularly polarised antenna for personal satellite communication and navigation,” in *IEEE Trans. Antennas Propagat.*, vol. 59, no. 12, pp. 4490-4496, Dec. 2011.

[29] W. T. Hsieh, T. H. Chang, and J. F. Kiang, “Dual-band circularly polarized cavity-backed annular slot antenna for GPS Receiver,” in *IEEE Trans. Antennas Propagat.*, vol. 60, no. 4, pp. 2076-2080, Apr. 2012.

[30] S. Velan *et.al.*, “Dual-band EBG integrated monopole antenna deploying fractal geometry for wearable applications,” in *IEEE Antennas Wireless Propag. Lett.*, vol. 14, pp. 249-252, 2015.

[31] J. Tang *et.al*, “Energy efficiency optimization with SWIPT in MIMO broadcast channels for internet of things,” in *IEEE Internet of Things Journal*, vol. 5, no. 4, pp. 2605–2619, Aug. 2018.

[32] C. Peng *et.al.*, "Optimal power splitting in two-way decode-and-forward relay networks", in *IEEE Commun. Lett.*, vol. 21, no. 9, pp. 2009-2012, Sep. 2017.

[33] M. Abedi, H. Masoumi, and M. J. Emadi, " Power splitting-based SWIPT systems with decoding cost," in *IEEE Wireless Commun. Lett.*, vol. 8, no. 2, pp. 432-435, Apr. 2019.

[34] P. A. Howher, “FSK-based simultaneous wireless information and power transfer in inductively coupled resonant circuits exploiting frequencies splitting,” in *IEEE Access.*, vol. 7, pp. 40183–40194, Mar. 2019.

[35] J. G. Kim *et.al*, “A splitting frequencies-based wireless power and information simultaneous transfer method,” in *IEEE Trans. Circuits Syst.*, vol. 65, no. 12, pp. 4434–4445, Dec. 2018.

[36] X. Zhou, R. Zhang, and C. K. Ho,” Wireless information and power transfer: architecture design and rate-energy tradeoff,” in *IEEE Trans. Commun.*, vol. 61, no. 11, pp. 4754–4767, Oct. 2013.

[37] T. D. P. Perera *et.al*, “Simultaneous wireless information and power transfer (SWIPT): recent advances and future challenges,” in *IEEE Communications Surveys & Tutorials*, vol. 20, no. 1, pp. 264-302, Dec. 2017.

[38] B. Clerckx *et.al*, “Fundamentals of wireless information and power transfer: from rf energy harvester models to signal and system designs,” in *IEEE Journal on Selected Areas in Communications*, vol. 37, no. 1, pp. 4-33, Sept. 2019.

[39] R. Lei, D. Xu, and I. Ahmad, " Secrecy outage performance analysis of cooperative noma networks with SWIPT," in *IEEE Wireless Commun. Lett.* (Early Access), Apr. 2021. DOI: 10.1109/LWC.2021.3070429.

CHAPTER 2. LITERATURE REVIEW

The purpose of this chapter is to present a general overview of antennas for WBAN/WPAN applications and current hardware implementations related to simultaneous information and power transfer (SWIPT). It is an essential point of departure as it offers a full picture for the motivation behind this research while presenting a useful insight into the research field and its current trends.

Overviews of implantable and ingestible antennas for WBAN are given in Section 2.1.1 and Section 2.1.2. In Section 2.1.3, metamaterials used for biomedical applications are described. WPAN, antennas equipped with localisation and tracking capabilities are discussed in Section 2.2. Current progress in merging wireless power transfer (WPT) into wireless data communication networks in terms of hardware realisations is reviewed in Section 2.3.1. This is followed by a discussion of WPT architecture in Section 2.3.2 which helps with the construction of a simultaneous wireless information and power transfer system.

2.1 Overview of Antennas for WBAN

WBAN technology is playing an important role in revolutionising biomedical telemetry systems, including facilitating health monitoring and medical aids [1]-[3]. Most of these devices belong to one of two categories, implantable, or ingestible, on basis of the way they are placed onto, or inserted into, a human body. As shown in Fig. 2-1, implantable devices are normally placed inside the human body via surgical operation and include devices such as pacemakers, blood glucose monitors, and brain implants [5]-[7]. Ingestible devices are commonly capsule-shaped that they to be swallowed like regular medical pills [8], [9]. Antennas are key elements for these devices, enabling bidirectional communications with other control units. General design challenges for such antennas include size miniaturisation, detuning desensitivity to the body environment (bandwidth enhancement), biocompatibility, and user safety. Current

solutions to these challenges on implantable and ingestible antennas are discussed in Section 2.1.2 and Section 2.1.1.

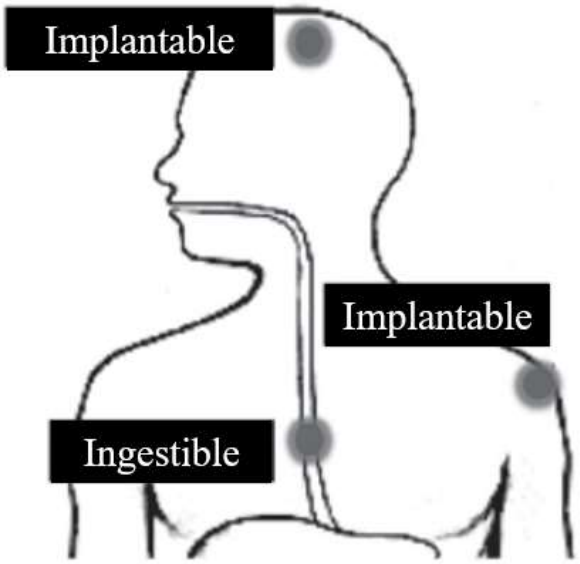

Fig. 2-1: Implantable and ingestible devices for biomedical telemetry [4].

2.1.1 Implantable Antennas

For physiological acceptability, the overall size of an implantable antenna should be miniaturised. There are four common miniaturisation methods for implantable antennas. The first is to select an appropriate substrate and superstrate material, each with a high dielectric constant (ε_r) property. A high dielectric constant leads to a shorter effective wavelength and results in the lowering of a design's resonant frequency. Rogers 3010 ($\varepsilon_r = 10.2$, loss tangent $\tan\delta = 0.0035$), Rogers 3210 ($\varepsilon_r = 10.2$, $\tan\delta = 0.003$), and Rogers 6010 ($\varepsilon_r = 10.2$, $\tan\delta = 0.0035$) are preferred by most researchers [10]-[14]. These materials with high dielectric constants can not only reduce overall size but also decouple the antenna from the absorbing lossy body environment as well as stabilise against effective permittivity fluctuations in the various body tissues encountered by the antenna [15]. However, the input power of an implantable antenna may convert into surface waves if a material with a very high dielectric constant is used [16] and as a result, the radiation efficiency would be affected.

Another way to achieve miniaturisation is to select higher frequency bands such as the licensed ISM 2450 MHz band or even millimetre-wave frequencies [17]-[19]. Higher resonant frequencies lead to an overall smaller antenna size. The main concern here relates to losses, which influence the signal transmission from the antenna through the body as losses in human body tissues at RF frequencies generally increase with frequency [19].

The third method is to increase the lengths of current paths of radiators. Generally, increasing the current path length leads to a lower resonant frequency [13], [14], [20]-[22]. As shown in Fig. 2-2, shorting pins and open-ended slots on an antenna ground plane can be used to lengthen current paths leading to a significant reduction in antenna size. Moreover, radiator stacking can also increase current path length. Fig. 2-3 shows how two radiators of an implantable antenna can be stacked either vertically or horizontally [22], in this case leading to a 33% reduction in required antenna size.

Adopting stub loading and capacitive coupling can also help with size reduction as discussed in [12]. Inductive or capacitive loading can help with impedance matching at the desired frequency by adjusting the imaginary part of the impedance, thus facilitating size reduction for an implantable antenna [12], [23], [24]. Fig. 2-4 shows the influence of stub loading (case 2) and stub loading together with capacitive coupling (proposed design) on the reflection coefficient (S_{11}) of the antenna. It demonstrates that the resonant frequency shifts down dramatically with the loading stubs on the radiator, verifying that the overall size can be reduced for a fixed operating frequency with the use of loading stubs. Adding capacitive coupling among the stubs leads to further size reduction (operating frequency shifts downwards in Fig. 2-4).

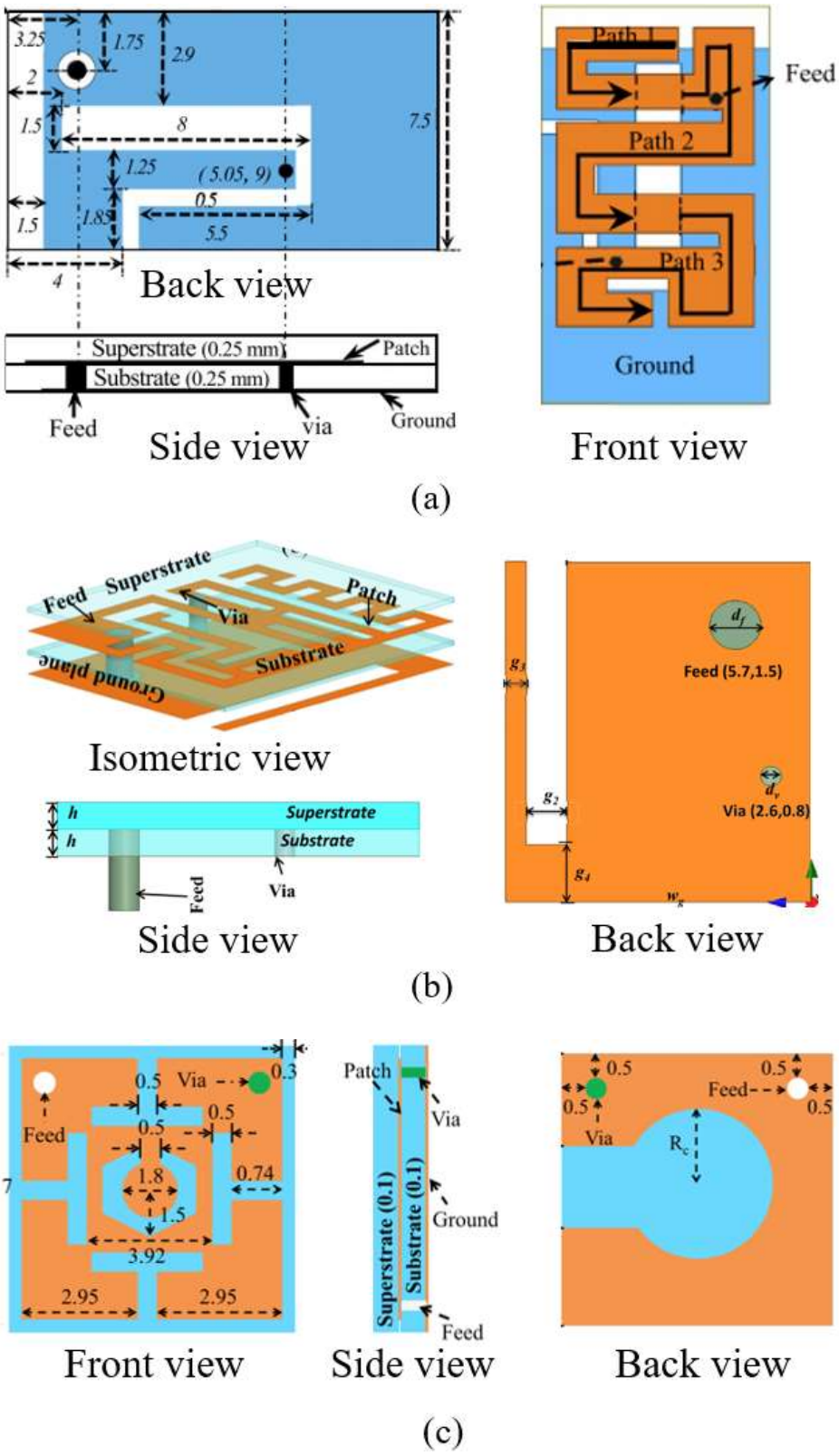

Fig. 2-2: Size miniaturisation by using shorting pins and open-ended slots on the ground plane: Antenna structure in (a) [13]; (b) [14]; (c) [20].

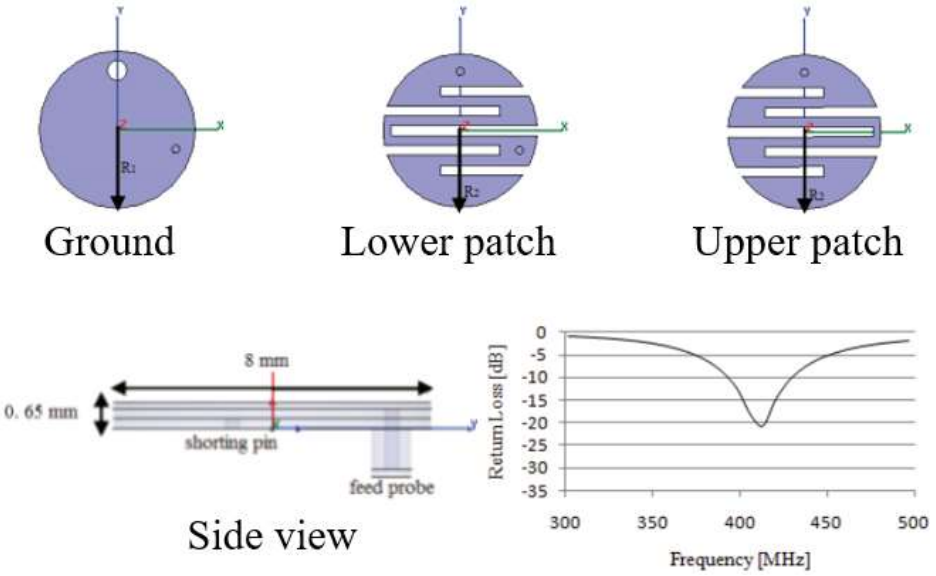

Fig. 2-3: Size miniaturisation by radiator stacking to increase radiator current paths [22].

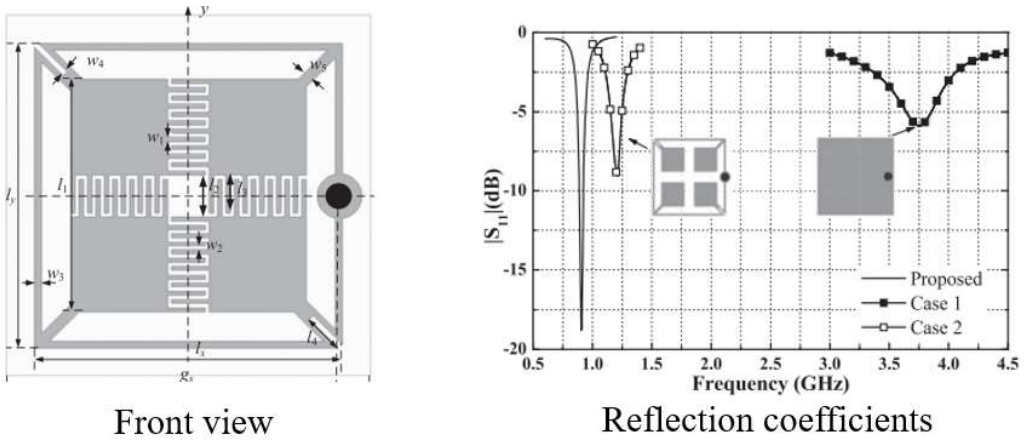

Fig. 2-4: Size miniaturisation by using stub loading and capacitive coupling [12].

Due to the heterogeneous environment inside a human body, sufficient operating bandwidth is an important demand for implantable antennas. An implantable antenna should have an adequate operating bandwidth to avoid being tuned away from the desired frequency band by the effects of the surrounding environment. Furthermore, dual- or multi- frequency band operation for a single antenna can enrich the variety of applications for which the antenna is equipped to support. For example, by cutting an open-ended slot on the ground plane of the antenna proposed in [14], two additional resonant frequencies appeared at 1.9 GHz and 2.45 GHz with corresponding operating bandwidths of 8.2% and 7.3%, respectively. This result is shown in Fig. 2-5(a). In this

case, the number of operating frequency bands has increased, however, the bandwidth around each resonance is still quite narrow and hence the antenna remains sensitive to detuning. Another example in Fig. 2-5(b) shows adding slots on the radiators and ground plane can also achieve dual-band operation but with improved bandwidths [22]. The bandwidths at 0.4 GHz and 2.4 GHz are 38.1% and 17.6%, respectively. However, to achieve this the overall antenna size (diameter = 20 mm, area = $2.517\lambda_0^2$) had to increase. A multi-band antenna example is depicted in Fig. 2-5(c). This antenna utilises a multi-layer structure to achieve multi-resonant frequencies. The bandwidths for the MICS and ISM bands are 28.1% and 2.8%, respectively. Overall, these mentioned techniques are beneficial, but in each case the structure of the implantable antenna becomes complicated and bulky, giving rise to the need for further improvement.

Biocompatibility and prevention of undesirable short-circuit from the human body presents another challenge in the design of an implantable antenna. Direct contact between an implantable antenna and body tissues results in a short-circuit situation for the antenna as the human body is conductive. As has been mentioned in Chapter 1, two approaches are commonly utilised to overcome this challenge. The first approach is to use biocompatible materials such as Titanium, Teflon, and ceramic alumina as opposed to the commonly used copper conductor and low loss RF substrates. The main problem with this approach is that drilling, round cutting and hence accurate manufacture of an antenna using these materials is difficult [24], [25].

Another approach is to use a low-cost thin biocompatible insulating film wrapped around the antenna such as polyamide, zirconia, silicone, Silastic MDX-4210 Biomedical-Grade Base Elastomer, or polyether ether ketone (PEEK) [26]-[28]. An example of coating a biocompatible insulating film is depicted in Fig. 2-6. Materials with high dielectric constant and low loss-tangent tanδ contribute to lower power loss by concentrating the near fields of the antenna inside the low-loss coating layer. The selection of the material is typically related to ease of handling and availability.

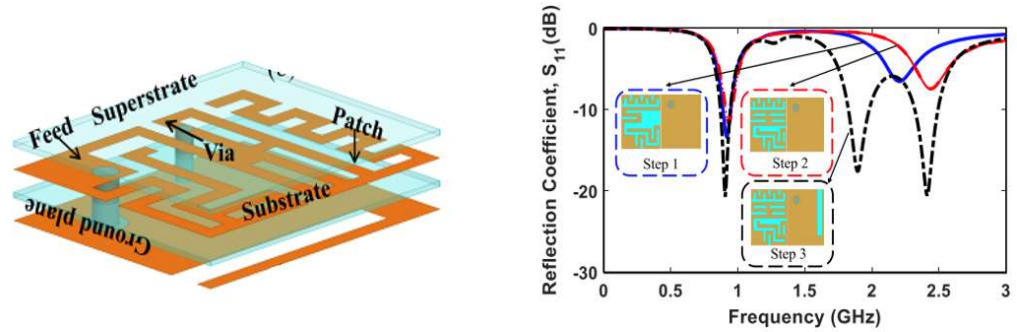

Antenna structure Reflection coefficients

(a)

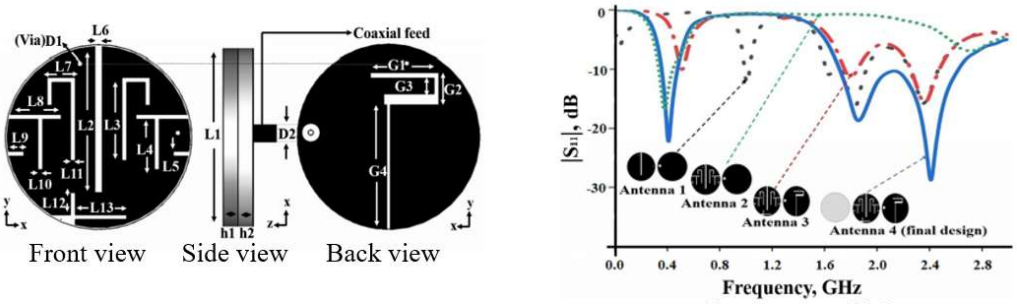

Front view Side view Back view

Antenna structure Reflection coefficients

(b)

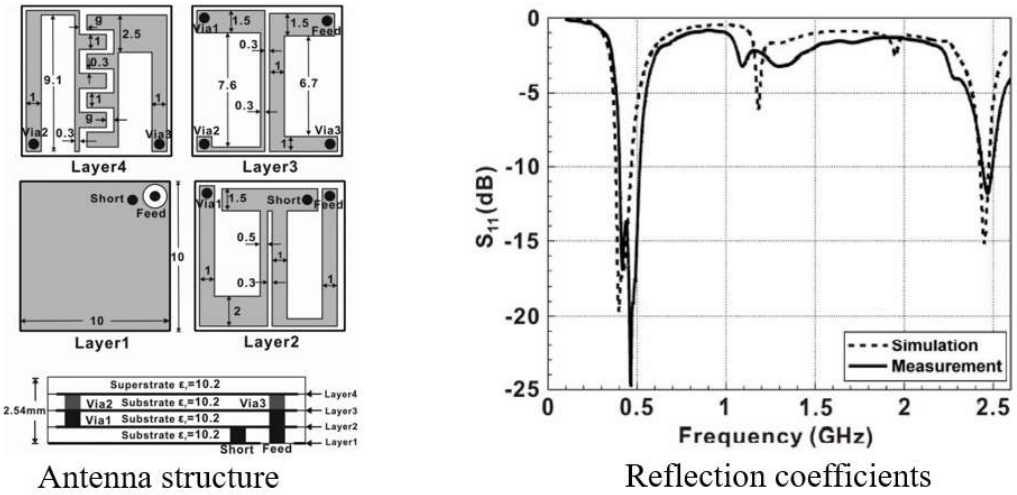

Antenna structure Reflection coefficients

(c)

Fig. 2-5: Examples of bandwidth enhancement: (a) [14]; (b) [22]; (c) [23].

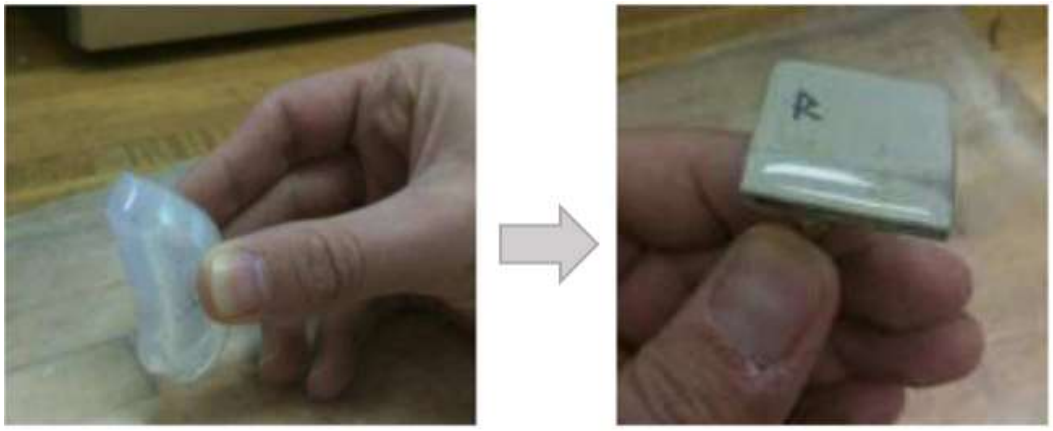

Fig. 2-6: An example of achieving biocompatibility by coating the implantable antenna with a thin biocompatible insulating film [26].

User safety is a key issue for designers of implantable or ingestible antennas since these devices are positioned inside the human body. Careful consideration is required to minimise danger to the human body tissues due to electromagnetic (EM) exposure. The Specific Absorption Rate (SAR) is widely acknowledged as the most appropriate measure for evaluating the safety of body tissues under EM exposure. SAR is defined as the amount of energy absorbed per unit mass of body tissue and can be calculated by Eq. (2.1):

$$SAR = \frac{P}{\rho} = \frac{\sigma |E|^2}{\rho} \tag{2.1}$$

where P (W/m^3) is the power loss density, σ (S/m) is the conductivity of the selected tissue, $\boldsymbol{E}$ (V/m) is the effective value of the electric field intensity within the tissue, and ρ (kg/m^3) is the mass density of the tissue [29].

From this equation, in a given material the maximum SAR value produced by an antenna will occur in the area where the electric field intensity is maximum. Currently, two widely accepted international standards for SAR are IEEE C95.1-1999 and IEEE C95.1-2005. The former limits the averaged SAR over any 1 g cubic volume of body

tissue to less than 1.6 W/kg [30]. The latter restricts the averaged SAR over any 10 g cubic volume of body tissue to less than 2 W/kg [31].

2.1.2 Ingestible Antennas

One of the most common ingestible device applications is the wireless capsule endoscope (WCE). This is normally a capsule-shaped device that people swallow like taking a regular pharmaceutical capsule pill [32], [33]. This kind of device can collect data such as images while passing through the gastrointestinal (GI) tract and transmit them to a surrounding monitoring device for post-processing, facilitating medical diagnosis and directing therapy [34]. A typical WCE is illustrated in Fig. 2-7, which shows that an ingestible device passes through and operates within the entire GI tract (including oesophagus, stomach, small/ large intestine, and colon) after being swallowed.

The components involved in a typical WCE are also depicted in Fig. 2-7. Generally, it contains a dome, light-emitting diodes (LEDs), a sensor pack, batteries, and an antenna system [35]. The antenna plays a key role for ingestible devices as it enables EM waves to be radiated and/or received. Allowing images to be transferred instantaneously reducing the need for data storage capacity within the device and speeding up medical processing. Compared to implantable antennas, ingestible antennas are more sensitive to detuning as they pass through a dynamically varying environment. To guarantee a robust communication link, a straightforward approach is to design a wideband antenna with sufficient bandwidth covering the possible detuning range hence achieving insensitivity to the lossy body environment. Basic requirements and challenges discussed before such as size miniaturisation and user safety for implantable antennas remain key for ingestible antennas.

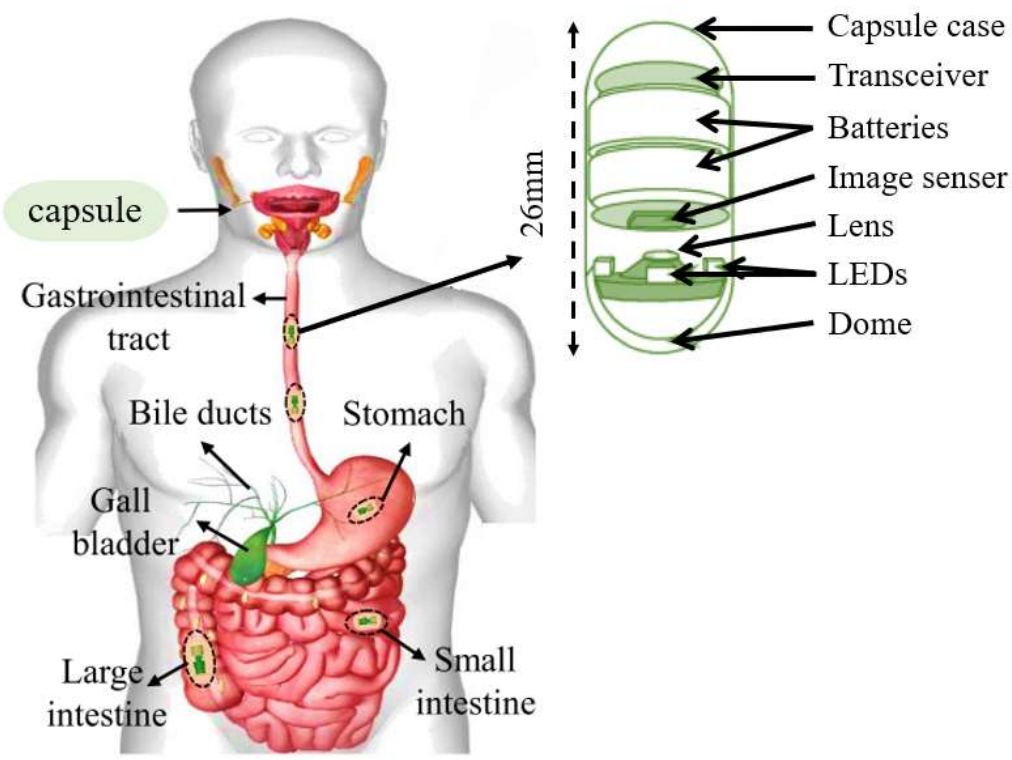

Fig. 2-7: Overview of a typical WCE operational path [49].

There are generally two categories of ingestible antennas regarding size requirement, namely embedded structure, and conformal structure. In an embedded structure, the antenna is placed inside the capsule cavity with the other components. Some examples are depicted in Fig. 2-8 and Fig. 2-9.

In Fig. 2-8 a capacitance-loaded embedded antenna is connected to a transceiver inside the capsule cavity. For simulation purposes, a cylinder with 2 mm height was used to represent the LED, and the camera and battery were replaced by perfect electrical conductors (PECs). The results in Fig. 2-8(c) show two phenomena. Firstly, the antenna reflection coefficient varies when the antenna is in the vicinity of different organs which is caused by the different dielectric constants of each organ, directly giving rise to the frequency shift. Another phenomenon is that placing the antenna inside the capsule cavity (with WCE) affects performance. The matching performance becomes worse compared to the case without the WCE system model.

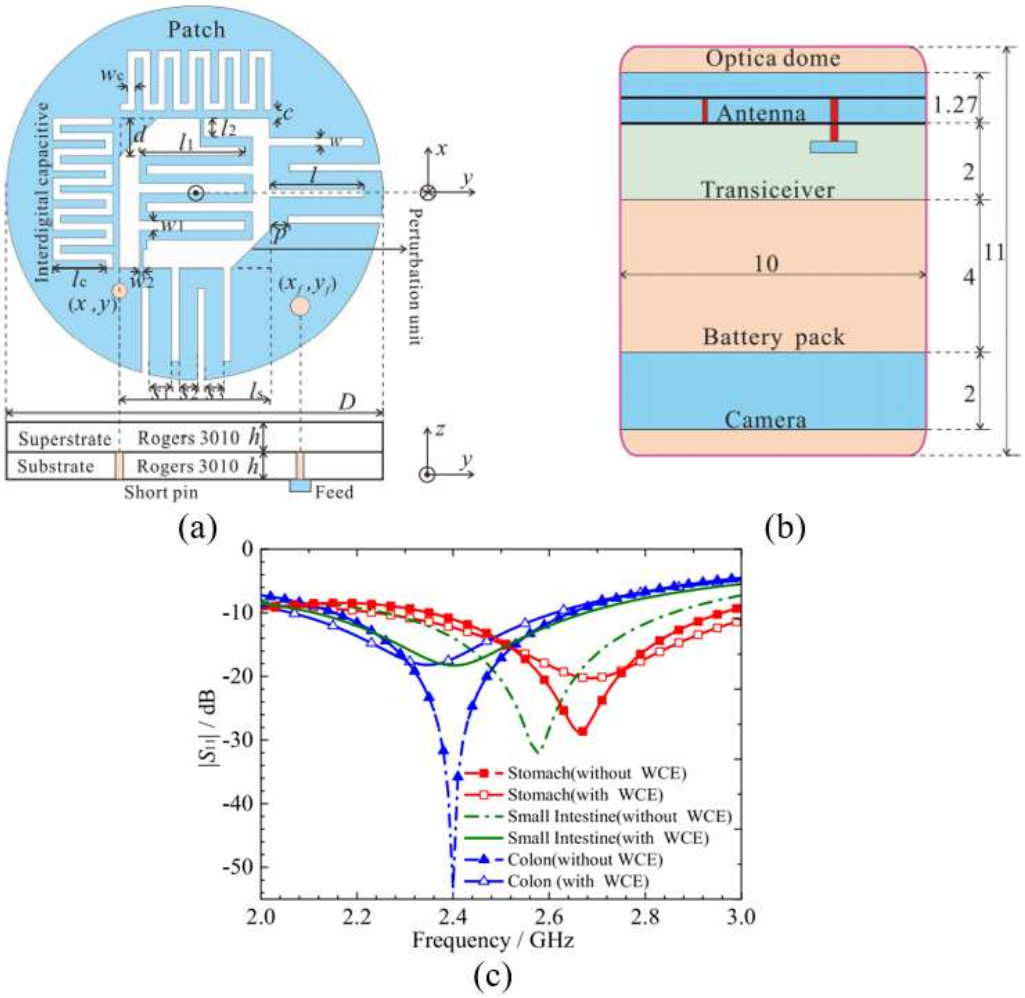

Fig. 2-8: Example of a capacitance-loaded embedded antenna for WCE [36]: (a) Geometry structure of the antenna; (b) Geometry structure of the WCE model; (c) Performance in different organs.

Loop and spiral antennas have also been used for embedded structures. A small loop antenna operating at 315 MHz and a conical helix operating at 450 MHz in Fig. 2-9(a) and (b) are placed inside the capsule cavity. The bandwidth in [37] is about 2 MHz which is likely insufficient to overcome the potential frequency detuning as the capsule passes through the GI tract. The resonant frequency for [38] is at 450 MHz which is not in the licensed frequency range for WBAN devices. Moreover, two vital features, radiation efficiency and realised gain, were not reported on in either example.

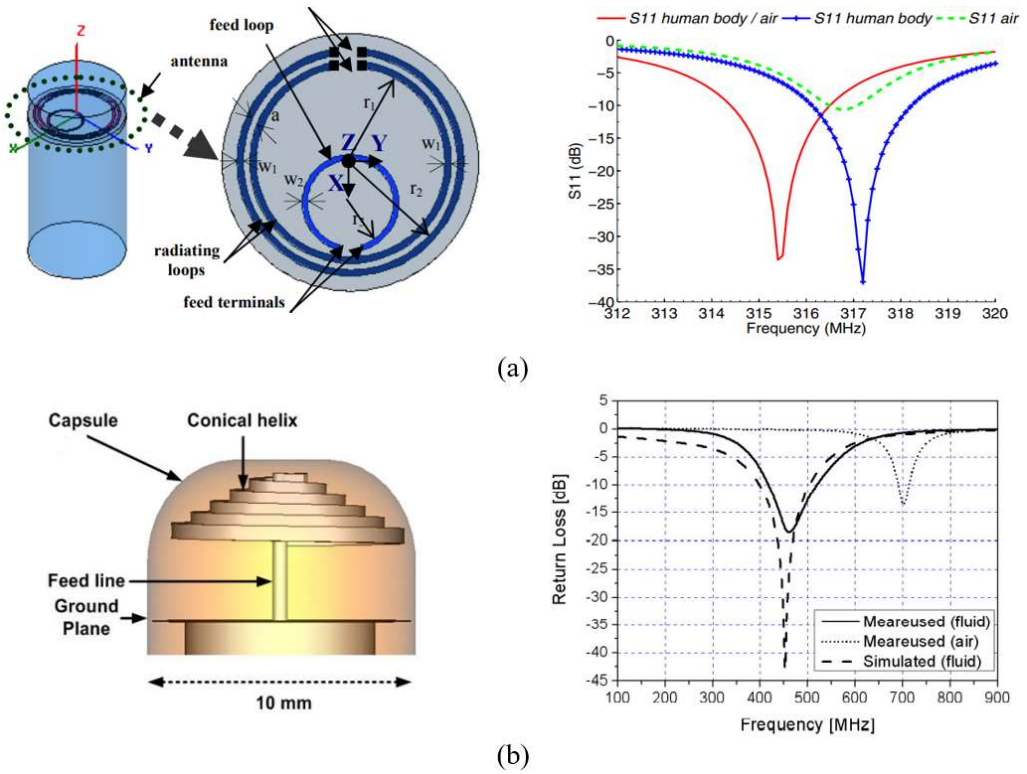

Fig. 2-9: Examples of embedded antenna for WCE: (a) [37]; (b) [38].

The second design approach takes full advantages of the capsule surface. This structure is a conformal structure, which adopts flexible substrate material to achieve conformality with the shell of the capsule. Conformal antennas for WCEs can be categorised according to the wrapping location, which can be either on the inner surface of the capsule shell (inner wall) or on the outer surface of the capsule shell (outer wall). The common advantage of wrapping on the inner wall of the capsule is that direct contact with body tissues is prevented [39]-[44]. Two examples are depicted in Fig. 2-10 presenting capsule antennas wrapped on the inner wall. The problem of the first of these antennas is its narrow bandwidth. The conformal microstrip antenna shown in Fig. 2-10(a) operates at 434 MHz with an overall size of 17 mm in length and 7 mm in diameter. In three liquid phantoms with muscle-equivalent, maximum, and time-averaged GI EM properties which were used to simulate the antenna operating environment, the antenna achieved an operating bandwidth of around 17 MHz. Fig. 2-10(b) is a conformal loop antenna with an overall size of 15 mm in length and 10 mm in diameter operating at 2.45 GHz with 31.58% fractional bandwidth (from 2.08 to

2.86 GHz). The gain is -29.1 dBi which is relatively low compared with others operating in the same frequency band.

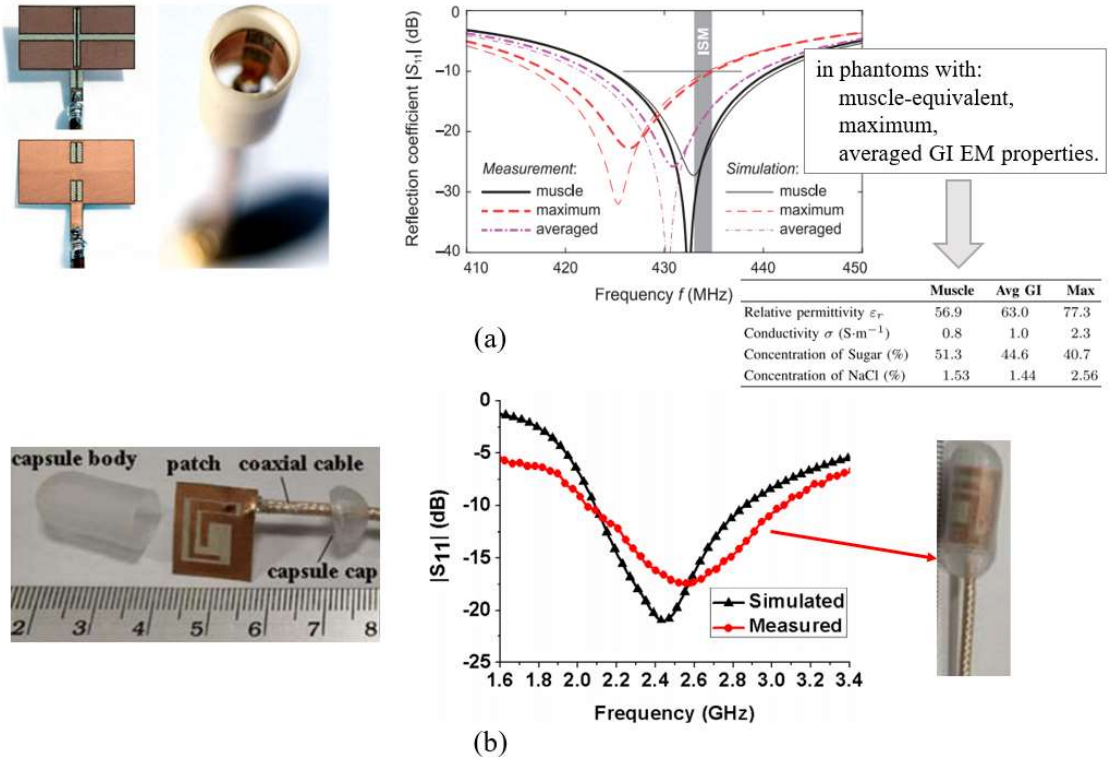

Fig. 2-10: Examples of conformal antennas placing on the inner wall of a WCE: (a) microstrip antenna [39]; (b) loop antenna [40].

Unlike an inner capsule wall antenna, wrapping on the outer wall requires careful consideration of the surrounding environment. Magnetic type antennas (loop antennas) are preferred over electric type antennas as they are less susceptible to the varying environment [37]. Wrapping loop antennas on the outer wall of the capsule commonly realises wide bandwidth [45]-[47]. The outer-wall loop antenna in Fig. 2-11(a) is placed inside a cylindrical homogeneous body model and has a resonant frequency of around 350 MHz. The realised bandwidth is 785 MHz from 215 MHz to 1 GHz, which can be regarded as ultra-wide. However, the radiation efficiency, gain, and matching behaviours of this design when placed in a realistic operating environment were not studied. Another example is depicted in Fig. 2-11(b). This antenna also has a wide bandwidth of 260 MHz (from 370 MHz to 630 MHz) which can contribute to robust

performance against the probable frequency detuning previously discussed. Despite these good characteristics, the size of the capsule is 28 mm in length and 11 mm in diameter, which is over the standard limitation of a WCE dimension (26 mm in length and 11 mm in diameter). Neither radiation efficiency nor gain was studied for this antenna.

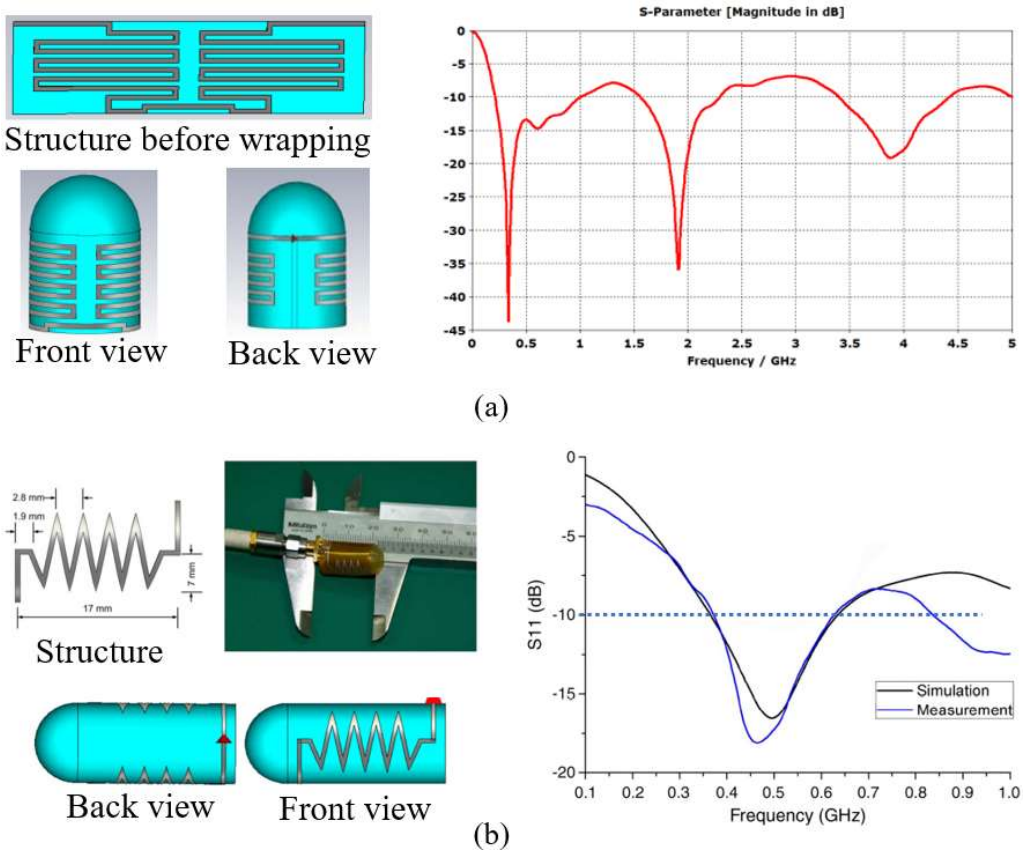

Fig. 2-11: Examples of the conformal antennas with loop structure placing on the outer wall of a WCE: (a) [45]; (b) [46].

Helix and PIFA structures have also been used for outer-wall wrapped style antennas [48]-[50]. The helix shape was verified to be less sensitive to the varying organ environments [50]. Such an antenna shape can be easily wrapped along the capsule shell while maintaining its geometry. An example of a helix-shaped antenna is provided in Fig. 2-11(a). The desired resonant frequency is 433 MHz with 20 MHz bandwidth. The simulated gain was -40.9 dBi and the simulated radiation efficiency -41.16 dB (0.007%), which are not sufficient to support convenient system functionality. The

example in Fig. 2-11(b) uses a planar inverted-F antenna (PIFA) structure. This antenna resonates at 403 MHz and the fractional bandwidth is 134.2% (284 MHz~825 MHz). However, the capsule operating environment was not described and evaluation of its performance in terms of reflection coefficients, radiation efficiencies and gains in different organs was not studied.

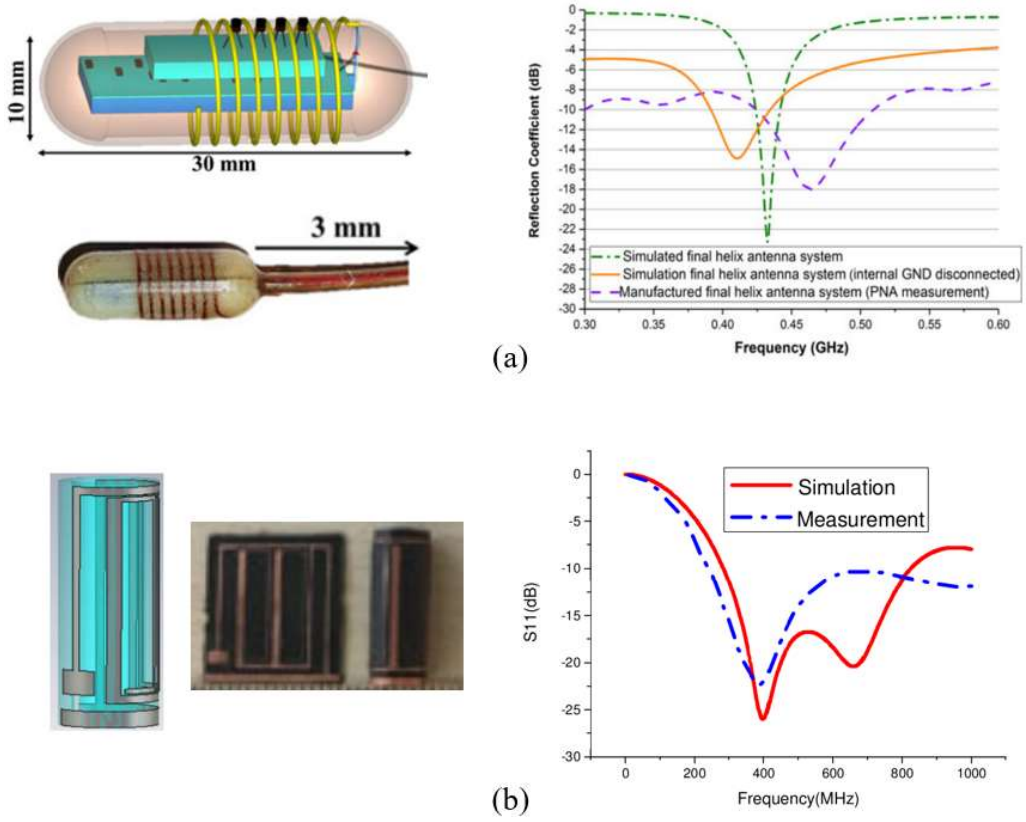

Fig. 2-12: Examples of conformal antenna placing on the outer wall of a WCE: (a) helix antenna [48]; (b) PIFA antenna [49].

2.1.3 Metamaterials for Bio-medical Applications

Artificial electromagnetic materials (metamaterials) have attracted increasing attention after a practical evaluation of split-ring resonators (SRRs) by the Pendry group [51] and an experimental demonstration by the Shelby group [52]. The dual counterparts of SRRs are complementary SRRs (CSRRs). The most prominent property of (C)SRRs is their ability to provide a negative permeability or permittivity near their resonant frequency [53]-[55]. Adopting (C)SRRs on bio-antenna designs brings a new approach

to size miniaturisation, multiband operation, and circular polarisation (CP). For example, a single-fed implantable antenna with four C-shaped slots and a CSRR loading on the radiator is shown in Fig. 2-13. The circular CSRR consists of two concentric metallic slot rings with two slits cut in opposite directions at the centre of the radiator as depicted in Fig. 2-13(a). This structure offers negative permeability, which contributes to a decreased electrical length for this unit cell at the desired resonant frequency [56]. The resonant frequency shifts from 4.5 GHz (case 1) to 2.45 GHz (case 2). In addition, adopting the CSRR introduced two more resonant frequencies which can be seen in Fig. 2-13(b). By carefully tuning the geometrical parameters, CP radiation is realised in [56] and the received CP bandwidth is 60 MHz (from 2.42 GHz to 2.48 GHz).

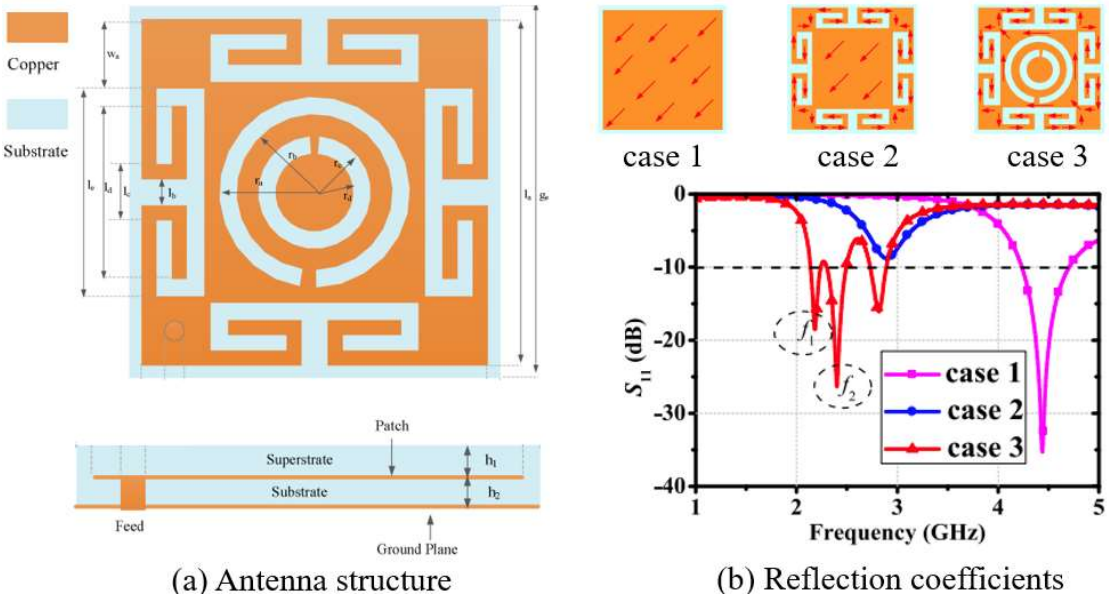

(a) Antenna structure (b) Reflection coefficients

Fig. 2-13: Example of a compact CSRR loaded CP implantable antenna: (a) antenna structure; (b) Reflection coefficients [56].

An example of adopting an SRR is shown in Fig. 2-14. A square slot etched on the front side of the substrate offers a resonant frequency of 2.5 GHz. The reflection coefficient plots in Fig. 2-14 show that the impedance matching improves, and more resonant frequencies are generated by adding strips inside the slot. The SRR in this design produces the lowest resonant frequency at 1.8 GHz, which helps with size

miniaturisation. Meanwhile, the excitation of the SRR provides CP radiation at this frequency. It should be acknowledged here that this design is not for WBAN/WPAN applications. The exploitation of the SRR/CSRR for implantable or ingestible applications has not been previously investigated in the literature and is a key innovation of this research.

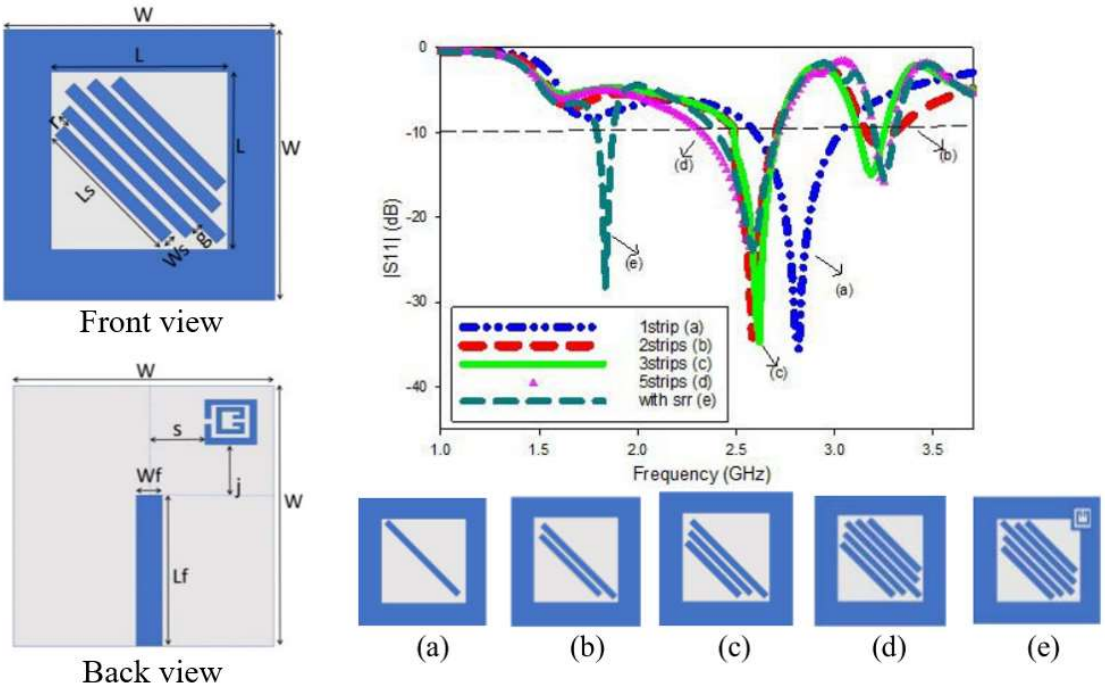

Fig. 2-14: Example of a compact SRR loaded slot antenna [57].

2.2 Design of Antennas for Localisation in WPAN Applications

WPAN applications are designed to not only provide relevant data but are often also able to provide information about a user's locality as explained in Chapter 1. The GNSS allows position and time information to be trackable, normally for outdoor scenarios [58]. The utilisation of CP antennas for GNSS is beneficial as it can prevent signal attenuation, multipath distortion, absorption losses and polarisation mismatch losses from Faraday rotation influences when transmitting or receiving waves [59]. Owing to the insufficient signal penetration into rooms or buildings, the ability of positioning for

GNSS-enabled devices is constrained from indoor scenarios, therefore, an additional frequency band is required to provide this information.

Developing capabilities of localisation for both indoor and outdoor scenarios for WPAN applications has become highly desirable and attractive in recent years. Considering the types of signals available inside rooms or buildings and those allowable for WPAN applications, the 2.45 GHz ISM band has been selected for indoor tracking [60]-[62]. It is thus desirable to design a multiband antenna covering the mentioned bands with CP ability. Examples of such antennas found in recent literature are discussed in the following.

A truncated patch antenna integrated into a military beret in [63] is designed for indoor and outdoor positioning. As shown in Fig. 2-15(a), this antenna is composed of a truncated patch, a circular ring patch with four shorting pins and a ground plane on the bottom side of the substrate [63]. The truncated patch realises a resonant frequency at 1.575 GHz for positioning outdoors with left-hand CP (LHCP). The circular ring patch with four shorting pins resonates at 915 MHz for indoor positioning. For outdoor positioning, the simulated AR bandwidth of the truncated patch is 2.4% (~37 MHz). Meanwhile, Fig. 2-15(b) also shows that this antenna can operate in different worn positions. Reflection coefficients in Fig. 2-15(d) indicate that impedance matching at both resonant frequencies is good. Overall, the performance of this design is satisfactory at the expense of a complex feeding mechanism, that two radiators achieve dual-band performance fed by two separate SMA connectors. The AR beamwidth at 1.575 GHz was not studied, which is vital for GNSS usage.

A dual-band antenna was proposed for indoor and outdoor positioning in [61]. The patch shaped radiator in Fig. 2-16(a) has a truncated pair of diagonal corners allowing CP performance to be attained. To achieve dual-band performance with a single feed port, four rectangular slits are cut from all four corners of the patch. By tuning the upper corners of the patch, it can resonate at 1.575 GHz. Similarly, tuning the lower corners is able to operate at 2.45 GHz. The measured operating bandwidths of this antenna are

185 MHz and 440 MHz at 2.45 GHz and 1.575 GHz respectively, shown in Fig. 2-16(b). The measured AR bandwidth is 9% at 1.575 GHz as shown in Fig. 2-16(d). The main problem of this work is that the AR beamwidth at 1.575 GHz was not studied. The overall physical size is 85.5 mm × 85.5 mm (electrical length = $0.4\lambda_0 \times 0.4\lambda_0 \times 0.02\lambda_0$) which is relatively large compared to other designs.

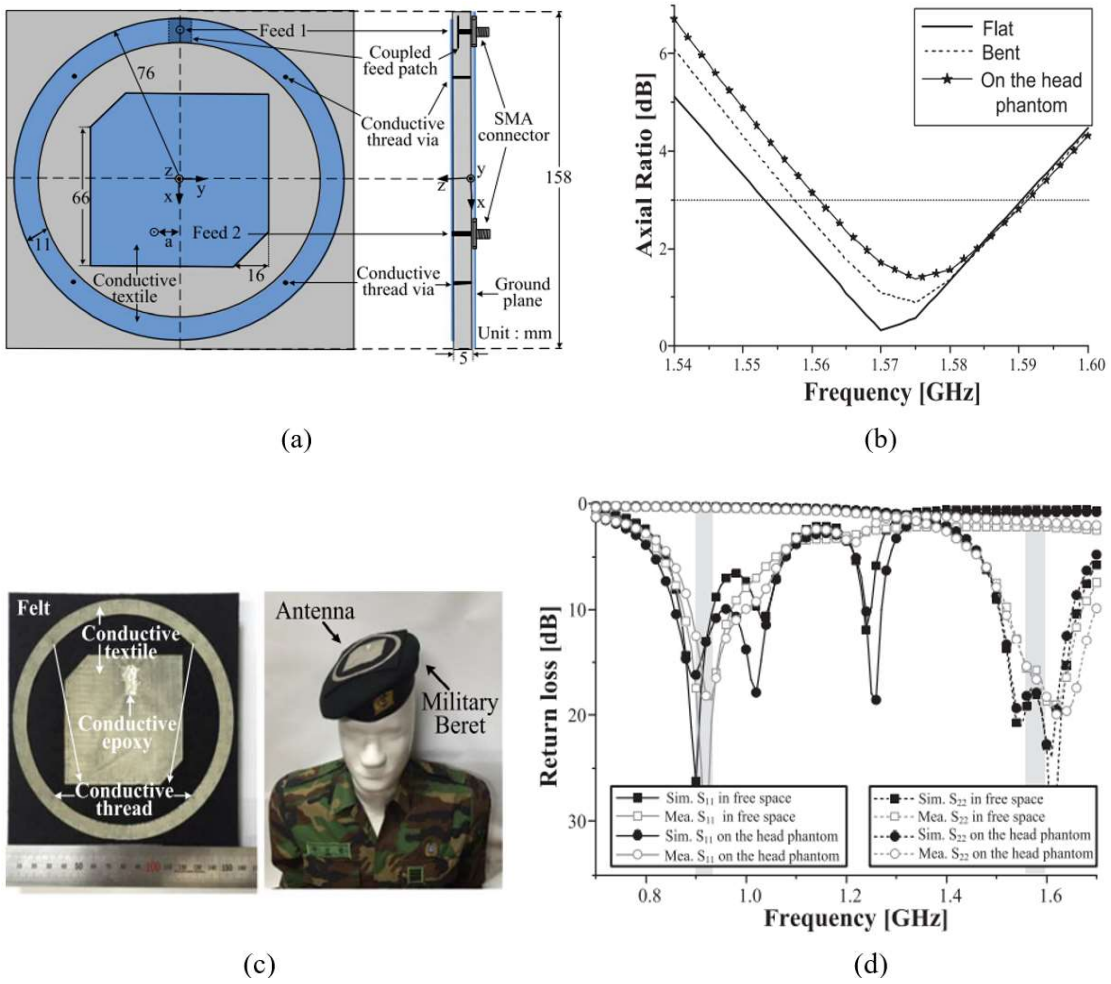

Fig. 2-15: Example of a GNSS-enabled dual-feed antenna [63]: (a) Antenna geometry; (b) Simulated AR for three different conditions; (c) Fabricated antenna and torso phantom (wearing the antenna integrated into the military beret); (d) Measured and simulated reflection coefficients.

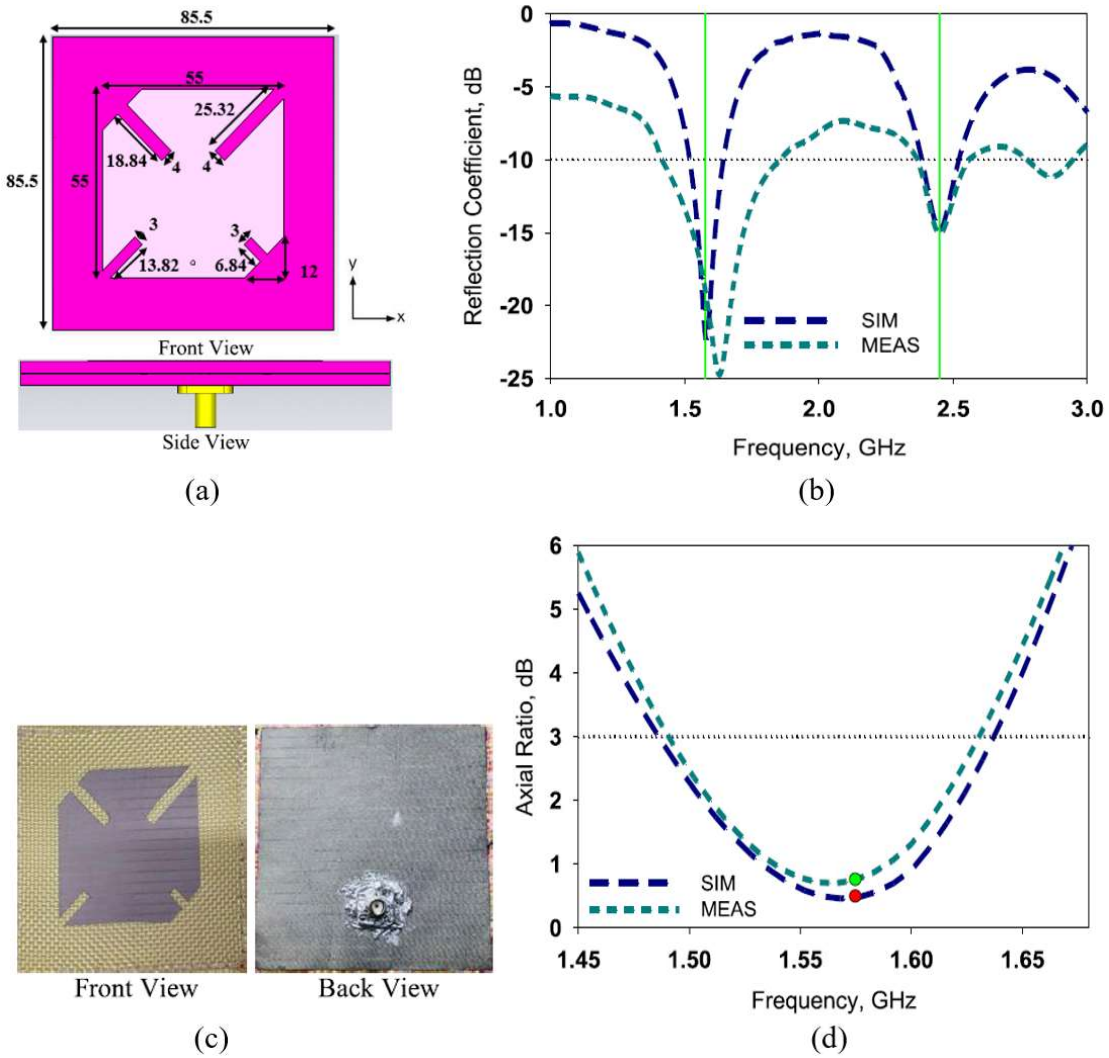

Fig. 2-16: Example of a GNSS-enabled single-feed antenna [61]: (a) Antenna geometry; (b) Measured and simulated reflection coefficients; (c) Fabricated prototype; (d) Simulated and measured AR in dB.

A dual-band antenna with CSRR and a single Y-shaped electromagnetic coupled feed line is proposed for indoor and outdoor positioning in [62]. Adopting a CSRR allows a size reduction to be realised as well as CP performance to be produced at the low resonant frequency instead of employing truncations, shorting pins, or a dual feed structure such as in [61] and [63]. Fig. 2-17(c) indicates that the operating bandwidths are from 1.564 GHz to 1.593 GHz (1.837%) and from 2.439 GHz to 2.457 GHz (0.735%) for indoor and outdoor scenarios. The AR plot in Fig. 2-17(d) shows the AR bandwidth is from 1.569 GHz to 1.581 GHz, which is narrow. The AR beamwidth at 1.575 GHz is 97.5°, which fails to meet the beamwidth requirement for GNSS.

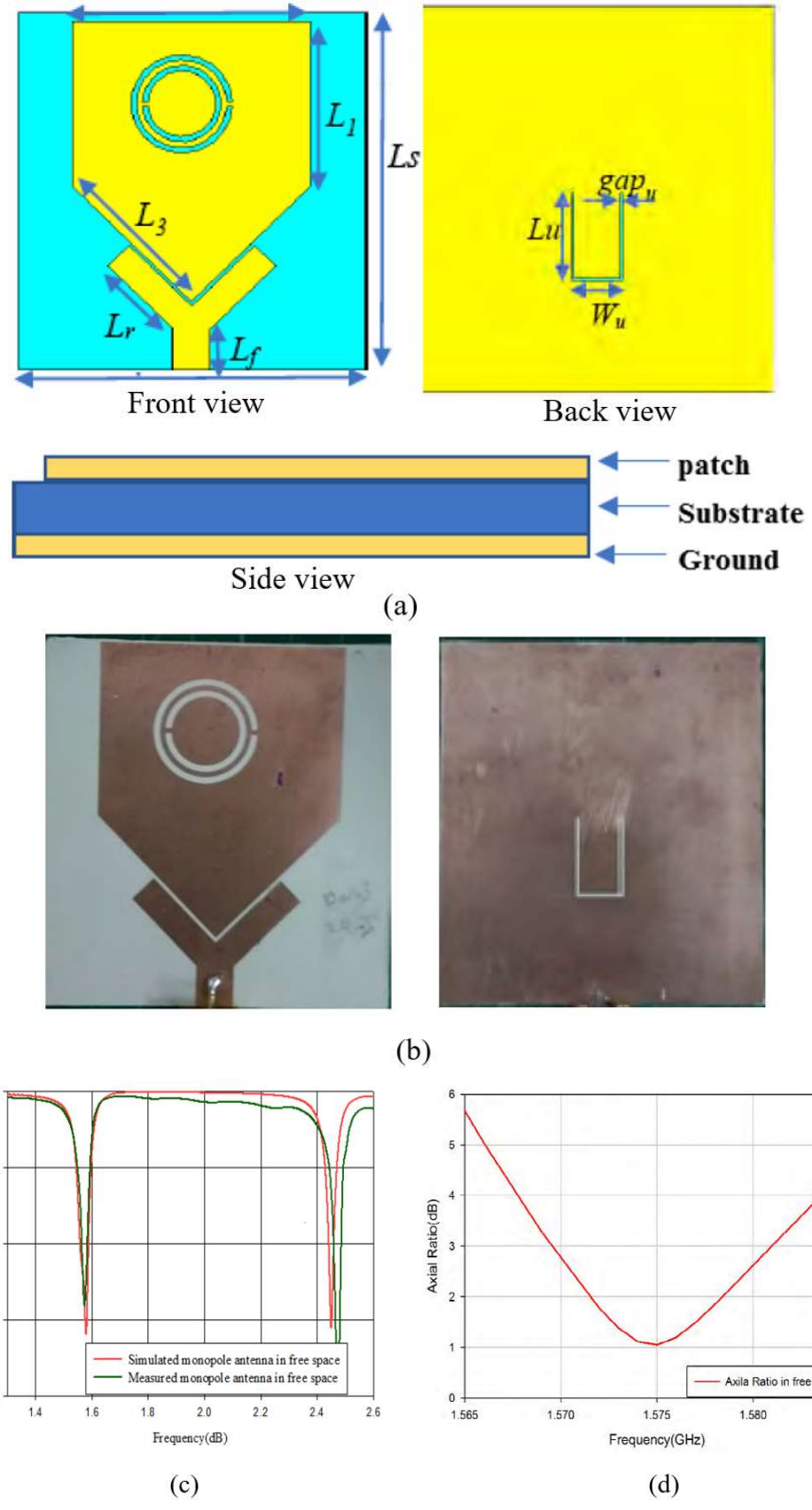

Fig. 2-17: Example of a GNSS-enabled antenna with CSRR [62]: (a) Antenna geometry; (b) Fabricated prototype; (c) Measured and simulated reflection coefficients; (d) Simulated and measured AR in dB.

2.3 Previous Studies of SWIPT

Due to size restrictions, battery-powered WBAN/WPAN applications (such as implants) have a limited energy storage capacity and hence require an inevitable battery replacement. This leads to constraints on the design of a reliable and self-powered communication module within the device. A promising solution to prolonging battery life and facilitate a sustainable communication network is to merge wireless power transfer (WPT) technology into the communication system [64]-[66]. WPT is one of the energy harvesting (EH) technologies in which EM radiations are captures and used to charge or directly power devices in a wireless system. WPT can be categorised into three types [65]:

1. Near-field WPT:

This technology uses coupling effects (e.g., inductive/capacitive coupling) to transfer power over a short distance, typically on the order of a meter. The power transfer level is in the range of tenths of Watts.

2. Far-field Directive Power Beaming WPT:

This technology uses directive antennas to transfer power. The power transfer level is in the range of milli-Watts, covering ranges of several meters in indoor and outdoor environments.

3. Far-field RF WPT:

This technology aims at providing power to low power devices, transferring power on the order of micro-Watts over longer distances up to several kilometres dependent on field energy density and without a specifically directed energy source.

Among these WPT technologies, the far-field RF WPT is the most suitable selection for powering low-power WBAN/WPAN applications as connected devices operate on RF bands to communicate with each other [67]. With this technology, the RF energy of the propagating waves can be collected and accumulated at the device's receiving

terminals to compensate for the energy consumption of the device itself. Such a network has the ability to utilise the received RF radiation in the most efficient manner and realise a self-sustaining distributed device communication network. This is called wireless information and power transfer (WIPT). There are three types of WIPT as illustrated in Fig. 2-18.

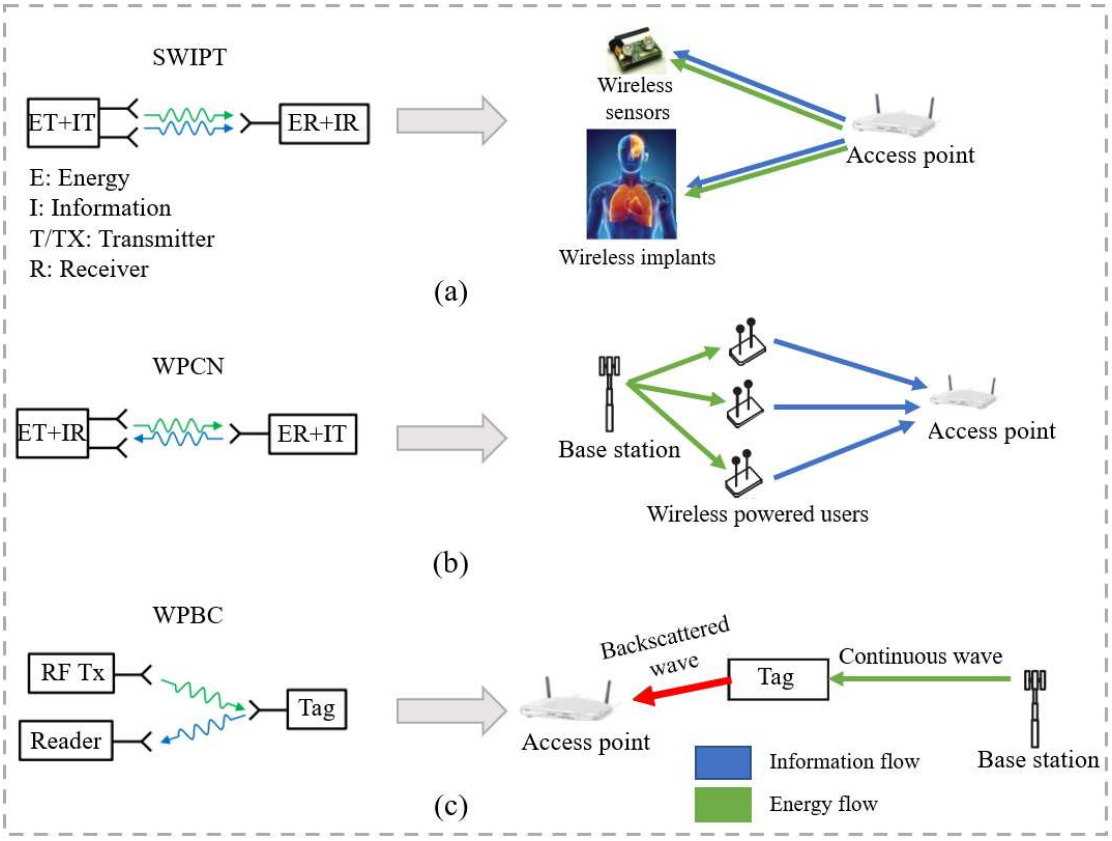

Fig. 2-18: Types of WIPT: (a) SWIPT; (b) WPCNs; (c) WPBC [68], [69].

The first type is called simultaneous wireless information and power transfer (SWIPT) [68], [69], which allows data and power to be received simultaneously via the same EM wave in the downlink. The second type is the wirelessly powered communication network (WPCN) [68], [69], these enable energy to be transferred in the downlink and information collected from the receiving terminal to be transferred in the uplink. The last type is wirelessly powered backscatter communication (WPBC) [68], [69]. Backscatter modulation at a tag is used to reflect and modulate the received RF wave for communication. SWIPT is considered as the extension of far-field RF WPT for

WBAN/WPAN applications in this work, allowing an implanted or ingested device to receive power and communication control signals from a source simultaneously.

2.3.1 Techniques for SWIPT

Conventionally, processing EH and information decoding (ID) on the same RF waves simultaneously is impossible because performing EH on incoming waves destroys the information carried. Therefore, received waves should be separated into two streams for the EH and ID processes. There are four commonly adopted splitting techniques for an integrated receiver (IR) system to practically perform SWIPT as follows:

A. Separate Receivers

Early hardware implementations for SWIPT adopted two separate receivers as demonstrated in Fig. 2-19. This structure is easy to construct and current receiving topologies for ID and EH can be utilised to process the received signals. The major drawback of this scheme is that the system is cumbersome and hence is not suitable for wireless sensors or other devices [70], [71], which should be compact. This technique can be optimised by using an antenna switching architecture which is explained in part B below.

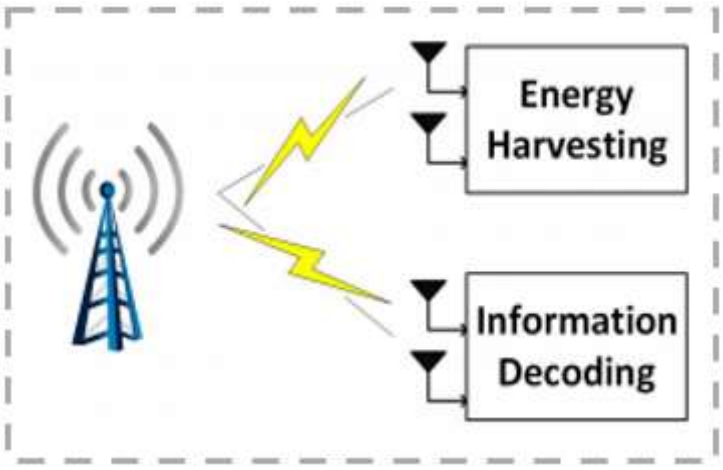

Fig. 2-19: Separated receivers technique for SWIPT [70].

B. Time Switching (TS)

The TS scheme switches between EH and ID modes in successive time slots as shown in Fig. 2-20. The main advantage is that this scheme shares the same antenna for EH and information reception. The hardware implementation is relatively simple as a switch is employed to select EH and ID modes periodically [70], [72]. Thus, the majority of research on this technique is about optimising the switching period [72]-[78]. Owing to periodically switching modes, technically this is not a SWIPT system. Meanwhile, precise time synchronisation and information/energy scheduling are required to reduce information and power losses.

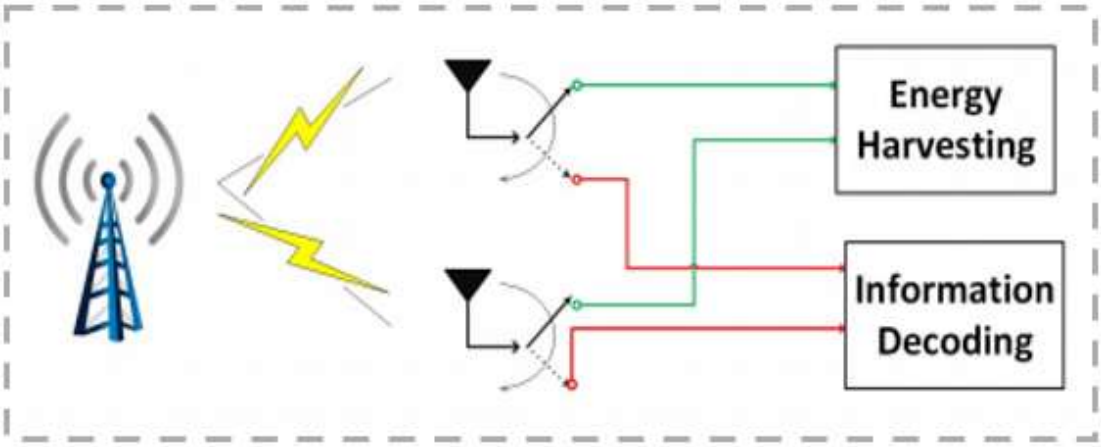

Fig. 2-20: TS technique for SWIPT [70].

C. Power Splitting (PS)

The PS scheme aims to split the received signal into two power streams for EH and ID separately according to a pre-defined splitting ratio as demonstrated in Fig. 2-21. The information rate and the amount of energy to be harvested depend on this PS ratio. By optimising the ratio, a balance between EH and ID could be reached. The main benefit of this scheme is that the received signal can be simultaneously exploited for both EH and ID processes [70]. Overall, the IR system is passive which means time synchronisation is no longer problematic. Major challenges of the PS scheme are the optimisation of the PS ratio to reduce information and power losses and maximising

efficiency as a radically wide gap exists between the required amounts of power for communication and WPT [72], [79]-[82].

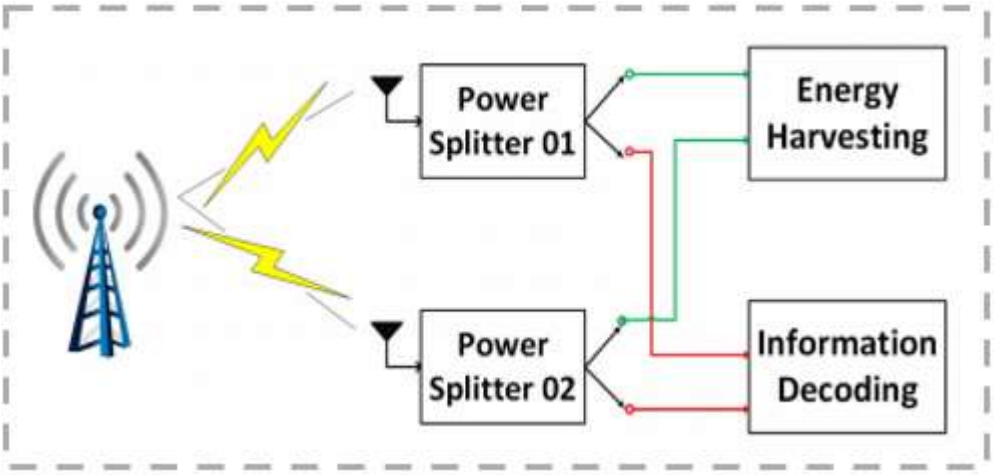

Fig. 2-21: PS technique for SWIPT [70].

D. Frequency Splitting/Antenna Switching (FS/AS)

The operating mechanisms behind FS and AS are similar as they separate signals in the frequency domain. The AS technique typically employs antenna arrays to achieve SWIPT as demonstrated in Fig. 2-22. The antenna arrays at the receiving terminal are divided into two groups where one aims at ID and the other collects waves for EH [83]-[85]. The major challenge of AS is the optimal allocation of antenna units for ID and EH. The FS technique normally has one dual-band antenna with one band used for EH and the other for ID [86] or it employs coils that allocate the power signal to a single-tone centre frequency and information to the spectrum around the centre frequency [87], [88]. The common problem of both techniques is that they use two or more frequency bands to perform ID and EH independently instead of dealing with the same signal concurrently.

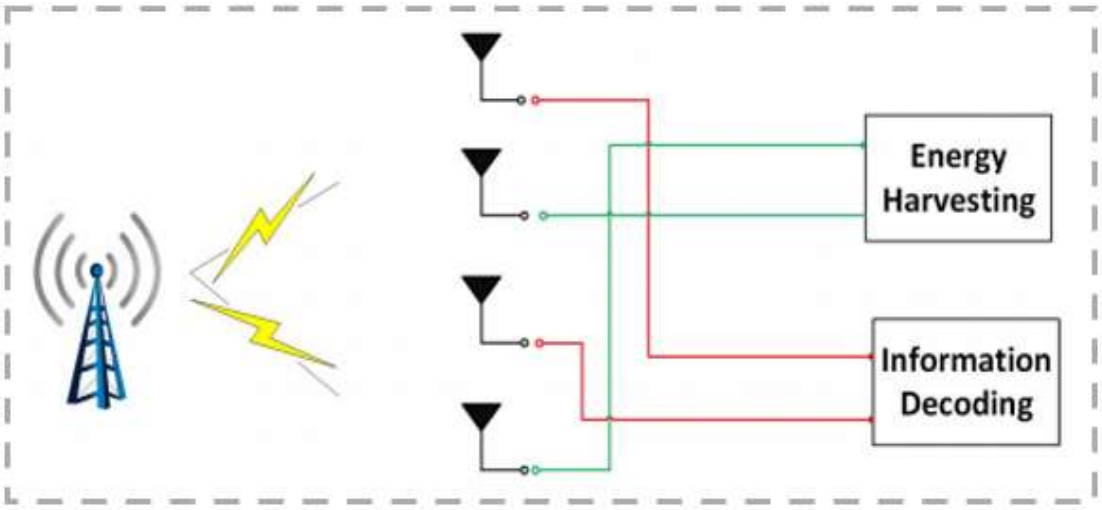

Fig. 2-22: AS technique for SWIPT [70].

2.3.2 RF WPT Architecture

A typical far-field RF WPT architecture is depicted in Fig. 2-23. The overall performance of a receiver is dependent on each element shown in this figure, such as the antenna (or array), matching network, and rectifying circuit (RF to DC converter). The general process is that firstly the antenna captures the RF signals and then these signals are delivered to a rectifying circuit through a matching network. The rectifying circuit is used to convert RF into direct current (DC) and the DC voltages can be used for various applications, such as powering loads and batteries (storage management). The overall performance of the system is evaluated by the actual DC voltage levels and the RF-to-DC power conversion efficiency (PCE). The PCE can be calculated by Eq. (2.2):

$$PCE = \frac{P_{DC}}{P_{in}} = \frac{V_{DC}^{\ 2}}{P_{in} R_L} \tag{2.2}$$

where P_{DC} is the output DC power, P_{in} is the input power, R_L is the load impedance, and V_{DC} is the output DC voltage.

Many surveys have been conducted on the optimisation of the performance of each element, especially in terms of PCE and Table 2-1 summarises relevant literature reviews [89]-[96] with their PCE optimisation stages (a) to (e) shown in Fig. 2-23.

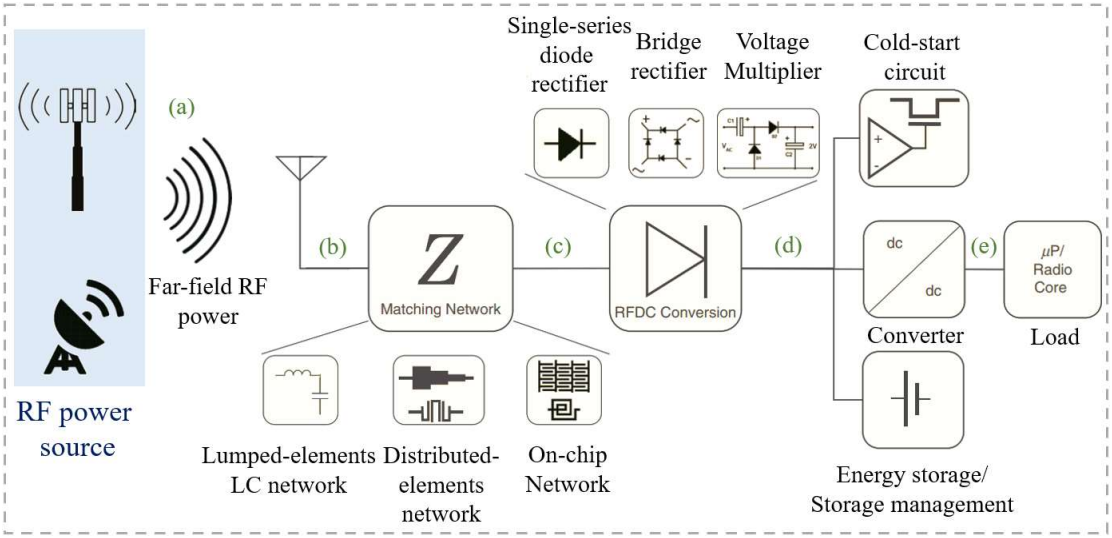

Fig. 2-23: General hardware implementation of a far-field RF WPT system [89].

Table 2-1: Summary of Published Research on Optimisations of an RF WPT System.

Stage	Power type	Optimised element	Ref.
(b)	RF	Antenna radiation properties	[89]
(b) & (c)	RF	Antenna & matching network	[89], [90] [91], [92]
(c) & (d)	RF	Rectifying circuit topologies	[90], [91] [93], [94]
(d)	Unregulated DC	Power management circuitry	[94], [95]
(e)	Regulated DC	Load & network architecture	[90], [96]

The impedance matching network in Fig. 2-24 affects the amount of power captured by the antenna that can be delivered to the rectifying circuit. A good matching network

helps to minimise the transmission loss from the antenna to the rectifying circuit. When the impedances are matched, maximum RF-DC power transfer is obtained for the rectifier design.

The rectifying circuit is used to convert the input RF power into a DC output. It consists of at least one non-linear component such as a diode. Considering WBAN/WPAN applications in this work function at low power, the selection of diode should be for low power consumption and low forward bias voltage. Schottky diodes such as the SMS7630 from *Skyworks* are proven to be the best choice as their forward bias voltage is low and saturation current is high (60-120 mV at 0.1 mA) [97], [98]. They can work well at low power levels (typically from -30 to 5 dBm) and have a fast-switching action [65]. Due to the non-linearity of rectifying circuits, the input impedance of a rectifying circuit is dependent on frequency, input power level and load impedance. Hence, designing a suitable impedance matching network is a significant and important challenge.

Commonly, designs of antennas are matched with a 50 Ω feeding network, therefore, the main challenge in designing impedance matching networks becomes transforming the input impedance to the rectifier's input impedance at the desired frequencies, within the desired power levels and load range [89]. Four typical impedance matching scenarios are demonstrated in Fig. 2-24. The common matching network for scenarios in Fig. 2-24 (a) and (b) are lumped element *LC* matching networks [99], [100]. For scenarios in Fig. 2-24 (c) and (d), matching networks with hybrid lumped elements (especially series inductors and capacitors) and distributed elements are commonly used to reduce the complexity of the circuit [101]-[105].

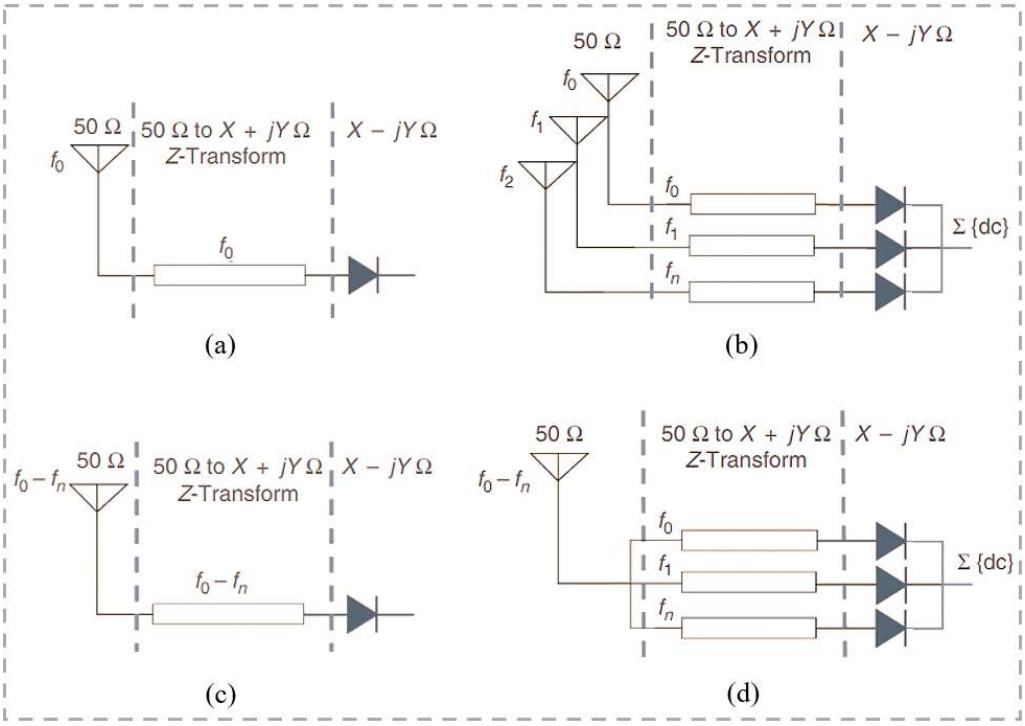

Fig. 2-24: Four typical impedance matching scenarios: (a) A single band rectenna; (b) A multiband rectenna with matching network and rectifying circuit per frequency band; (c) A broadband rectenna with a broadband matching network; (d) A broadband rectenna with separate matching networks for each frequency band [89].

2.4 Summary

This chapter has outlined and discussed the basic requirements regarding designs of antennas for WBAN/WPAN applications and provided foundational knowledge for SWIPT including splitting techniques and hardware implementations, which are essential to understand the remaining content of this thesis.

An overview of implantable and ingestible antennas for WBAN regarding the four major challenges (size miniaturisation, detuning ability for body environment, biocompatibility, and user safety) was set out. Section 2.1.2 and Section 2.1.1 have provided details on current works and discussed their limitations. It was found that the majority of existing implantable and ingestible antennas for WBAN in the literature can only operate within one allowed licensed band for a particular function, and none of them satisfies all requirements due to the difficulty and complexity of their structure.

Therefore, a more general compact wideband antenna that satisfies all of these requirements with robust performance for multi-usage (implantable and ingestible applications) is of interest.

Section 2.1.3 has highlighted the opportunities afforded by the use of metamaterials in the design of implantable and ingestible antennas. Current achievements include increasing the number of resonant frequency points, bandwidth enhancement, and size reduction. Impacts of metamaterials on radiation performance and power loss have not been well studied according to the existing literature, which becomes an interesting research aspect that will be examined in this thesis.

Current designs of antennas for localisation have been discussed in Section 2.2. They aim at WPAN applications, however, only their localisation ability has been researched. The expansion of this to provide multifunctioning operation such as in the monitoring of user physiological changes has not been investigated. Furthermore, the AR beamwidth for these current designs was either not mentioned or does not meet the required standards.

Studies of merging WPT technology into a communication system in Section 2.3 have broadened the horizons of this research. Commonly adopted splitting techniques (Separate receivers, TS, PS, AS/FS) for an IR system have been outlined and evaluated in Section 2.3.1 in terms of their benefits and drawbacks. Architecture for the EH process has been illustrated and analysed in Section 2.3.2. The literature review for this part highlights that inevitable information and power loss existing in these splitting techniques provides the motivation to develop a new splitting technique that can improve on this current situation.

The state of art presented in this chapter offers a solid groundwork to identify research problems, current solutions, and remaining challenges and researching these to develop novel solutions becomes the main goal in this work.

2.5 References

[1] G. Virone *et al.*, “An advanced wireless sensor network for health monitoring,” in *Proceedings of the Transdisciplinary Conference on Distributed Diagnosis and Home Healthcare*, Apr. 2006.

[2] C. P. Ráez, “Overview of wireless sensor networks applications in medical care,” in *Proceedings of the Second International Symposium on Medical Information and Communication Technology*, Dec. 2007.

[3] T. Gao *et al.*, “Wireless medical sensor networks in emergency response: Implementation and pilot results,” in *Proceedings of the IEEE Conference on Technologies for Homeland Security*, May 2008.

[4] A. Kiourti and K. S. Nikita, “A review of in-body biotelemetry devices: implantables, ingestibles, and injectables,” in *IEEE Trans. Biomedical Eng.*, vol. 64, no. 7, pp. 1422–1430, Jul. 2017.

[5] S. A. A. Shah and H. Yoo, “Scalp-implantable antenna systems for intracranial pressure monitoring,” in *IEEE Trans. Antennas Propag.*, vol. 66, no. 4, pp. 2170–2173, Apr. 2018.

[6] X. Y. Liu, Z. T. Wu, Y. Fan, and E. M. Tentzeris, “A miniaturized CSRR loaded wide-beamwidth circularly polarized implantable antenna for subcutaneous real-time glucose monitoring,” in *IEEE Antennas Wireless Propag. Lett.*, vol. 16, pp. 577–580, 2017.

[7] A. Kiourti *et al.*, “A wireless fully-passive neural recording device for unobtrusive neuropotential monitoring,” in *IEEE Trans. Biomed. Eng.*, vol. 63, no. 1, pp. 131–137, Jan. 2016.

[8] M.Yuce *et al.*, “Easy-to-swallow wireless telemetry,” in *IEEE Microw.Mag.*, vol. 13, no. 6, pp. 90–101, Oct. 2012.

[9] R. Das and H. Yoo, “A wideband circularly polarized conformal endoscopic antenna system for high-speed data transfer,” in *IEEE Trans. Antennas Propag.*, vol. 65, no. 6, pp. 2816–2826, Jun. 2017.

[10] X. Liu, Z. Wu, and W. M. Tentzeris, “A miniaturized csrr loaded wide-beamwidth circularly polarized implantable antenna for subcutaneous real-time glucose monitoring,” in *IEEE Antennas Wireless Propag. Lett.*, vol. 16, pp. 577–580, Jul. 2016.

[11] S. Das and D. mitra, “A compact wideband flexible implantable slot antenna design with enhanced gain,” in *IEEE Trans. Antennas Propag.*, vol. 66, no. 8, pp. 4309–4314, Aug. 2018.

[12] C. Liu, Y. Zhang, and X. Liu, “Circularly polarized implantable antenna for 915 MHz ism-band far-field wireless power transmission,” in *IEEE Antennas Wireless Propag. Lett.*, vol. 17, no. 3, pp. 373–376, Mar. 2018.

[13] I. Gani and H. Yoo, “Multi-band antenna system for skin implant,” in *IEEE Microw. Wireless Compon. Lett*, vol. 26, no. 4, pp. 294–296, Apr. 2016.

[14] M. Zada and H. Yoo, “A miniaturized triple-band implantable antenna system for bio-telemetry applications,” in *IEEE Trans. Antennas Propag.*, vol. 66, no. 12, pp. 7378–7382, Dec. 2018.

[15] D. Nikolayev, M. Zhadobov, P. Karban, and R. Sauleau, “Increasing the radiation efficiency and matching stability of in-body capsule antennas,” in *Proc. 10th Eur. Conf. Antennas Propag.*, pp. 1–5, Apr. 2016.

[16] N. A. Malik, P. Sant, T. Ajmal, and M. Ur-Rehman, “Implantable antennas for bio-medical applications,” in *IEEE Journal Electromagnetics RF Microwaves in Medicine and Biology*, vol. 5, no. 1, pp. 84-96, Mar. 2021.

[17] Z. Yang, S. Xiao, L. Zhu, B. Wang, and H. Tu, “A Circularly Polarized Implantable Antenna for 2.4-GHz ISM Band Biomedical Applications,” in *IEEE Antennas Wireless Propag. Lett.*, vol. 16, pp. 2554–2557, Jul. 2017.

[18] M. Ur-Rehman, N. A. Malik, X. Yang, Q. H. Abbasi, Z. Zhang, and N. Zhao, “A low profile antenna for millimeter-wave body-centric applications,” in *IEEE Trans. Antennas Propag.*, vol. 65, no. 12, pp. 6329–6337, Dec. 2017.

[19] Q. H. Abbasi, M. Ur-Rehman, K. Qaraqe, and A. Alomainy, “Advances in body-centric wireless communication: Applications and state-of-the-art,” *IET*, UK, 2016.

[20] F. Faisal *et al.*, “A miniaturized dual-band implantable antenna system for medical applications,” in *IEEE Trans. Antennas Propag.*, vol. 68, no. 2, pp. 1161–1165, Feb. 2020.

[21] A. Kiourti and K. S Nikita, “A review of implantable patch antennas for biomedical telemetry: Challenges and solutions [wireless corner],” in *IEEE Antennas Propag. Mag.*, vol. 54, no. 3, pp. 210–228, Jun. 2012.

[22] A. Kiourti, M. Christopoulou, and K. S Nikita, “Performance of a novel miniature antenna implanted in the human head for wireless biotelemetry,” in *Proc. IEEE Int. Symp. Antennas Propag.*, pp. 392–395, 2011.

[23] L.-Jie Xu, Y.-X. Guo, and W. Wu, “Bandwidth enhancement of an implantable antenna,” in *IEEE Antennas Wireless Propag. Lett.*, vol. 14, pp. 1510–1513, 2014.

[24] C. Liu, Y.-X. Guo, and S. Xiao, “Capacitively loaded circularly polarized implantable patch antenna for ISM band biomedical applications,” in *IEEE Trans. Antennas Propag.*, vol. 62, no. 5, pp. 2407–2417, May 2014.

[22] N. Ganeshwaran, J. K. Jeyaprakash, M. G. N. Alsath, and V. Sathyanarayanan, “Design of a Dual-Band Circular Implantable Antenna for Biomedical Applications,” in *IEEE Antennas Wireless Propag. Lett.*, vol. 19, no.1, pp. 119–123, Jan. 2020.

[23] F. Huang, C. Lee, C. Chang, L. Chen, T. Yu, and C. Luo, “Rectenna application of miniaturized implantable antenna design for triple-band biotelemetry communication,” in *IEEE Trans. Antennas Propag.*, vol. 59, no. 7, pp. 2646–2653, Jul. 2011.

[24] R. Warty, M.-R. Tofighi, U. Kawoos, and A. Rosen, “Characterization of implantable antennas for intracranial pressure monitoring: Reflection by and transmission through a scalp phantom,” in *IEEE Trans. Microw. Theory and Techn.*, vol. 56, no. 10, pp. 2366–2376, Oct. 2008.

[25] P. Soontornpipit, C. M. Furse, and Y. C. Chung, “Design of implantable microstrip antenna for communication with medical implants,” in *IEEE Transactions on Microw. Theory and Techn.*, vol. 52, no. 8, pp. 1944-1951, August 2004.

[26] T. Karacolak, R. Cooper, J. Butler, S. Fisher, and E. Topsakal, “In vivo verification of implantable antennas using rats as model animals,” in *IEEE Antennas Wireless Propag. Lett.*, vol. 9, pp. 334–337, 2010.

[27] A. K. Skrivervik and F Merli, “Design strategies for implantable antennas,” in *Proc. Loughborough Antennas Propag. Conf.*, IEEE, 2011, pp. 1–5.

[28] J. Abadia, F. Merli, J.-F. Zurcher, J. R. Mosig, and A. K. Skrivervik, “3D-spiral small antenna design and realization for biomedical telemetry in the mics band,” in *Radioengineering*, vol. 18, no. 4, pp. 359–367, 2009.

[29] T. Wittig, “Sar overview,” CST User Manual, 2007.

[30] IEEE Standard for Safety Levels with respect to Human Exposure to Radio Frequency Electromagnetic Fields, 3KHz to 300 GHz, IEEE Standard C95. 1-1999, 1999.

[31] IEEE Standard for Safety Levels with respect to Human Exposure to Radio Frequency Electromagnetic Fields, 3KHz to 300 GHz, IEEE Standard C95. 1-2005, 2005.

[32] G. Iddan, G. Meron, A. Glukhovsky, and P. Swain, “Wireless capsule endoscopy,” in *Nature*, vol. 405, p. 417, May 2000.

[33] G. Ciuti, A. Menciassi, and P.Dario, “Capsule endoscopy: from current achievements to open challenges,” in *IEEE Reviews in Biomed.l Engin.*, vol. 4, pp. 59-72, 2011.

[34] A. Kiourti, K. A. Psathas, and K. S. Nikita, “Implantable and ingestible medical devices with wireless telemetry functionalities: A review of current status and challenges,” in *Bioelectromagnetics*, vol. 35, no. 1, pp. 1–15, Jan. 2015.

[35] P. M. Szczypinski, R. D. Sriram, P.V. J. Sriram, and D. N. Reddy, “A model of deformable rings for interpretation of wireless capsule endoscopic videos,” in *Med. Image Anal.*, vol. 13, no. 2, pp. 312–324, Apr. 2009.

[36] W. Cui *et al.*, “Design of wideband implantable antenna for wireless capsule endoscope system,” in *IEEE Antennas Wireless Propag. Lett.*, vol. 18, no. 12, pp. 2706–2711, Dec. 2019.

[37] F. El Hatmi, M. Grzeskowiak, T. Alves, S. Protat, and O. Picon, “Magnetic loop antenna for wireless capsule endoscopy inside the human body operating at 315 MHz: Near field behaviour,” in *Proc. 11th Medit. Micro. Symp. (MMS)*, pp. 81–87, Sep. 2011.

[38] S. H. Lee, K. Chang, K. J. Kim, and Y. J. Yoon, “A conical spiral antenna for wideband capsule endoscope system,” in *Proc. IEEE Antennas Propag. Soc. Int. Symp.*, pp. 1–4, Jul. 2008.

[39] D. Nikolayev, M. Zhadobov, L. L. Coq, P. Karban, and R. Sauleau, “Robust ultraminiature capsule antenna for ingestible and implantable applications,” in *IEEE Trans. Antennas Propag.*, vol. 65, no. 11, pp. 6107–6119, Nov. 2017.

[40] R. Li, Y. Guo, and G. Du, “A conformal circularly polarized antenna for wireless capsule endoscope systems,” in *IEEE Trans. Antennas Propag.*, vol. 66, no. 4, pp. 2119–2124, Apr. 2018.

[41] Z. Bao, Y. X. Guo, and R. Mittra, “An ultrawideband conformal capsule antenna with stable impedance matching,” in *IEEE Trans. Antennas Propag.*, vol. 65, no. 10, pp. 5086–5094, Oct. 2017.

[42] K. Zhang *et al.*, “A conformal differentially fed antenna for ingestible capsule system,” in *IEEE Trans. Antennas Propag.*, vol. 66, no. 4, pp. 1695–1703, Apr. 2018.

[43] R. Das and H. Yoo, “A multiband antenna associating wireless monitoring and nonleaky wireless power transfer system for biomedical implants,” in *IEEE Trans. Microw. Theory Techn.*, vol. 65, no. 7, pp. 2485–2495, Jul. 2017.

[44] R. Das and H. Yoo, “Biotelemetry and wireless powering for leadless pacemaker systems,” in *IEEE Microw. Wireless Compon. Lett.*, vol. 25, no. 4, pp. 262–264, Apr. 2015.

[45] R. Alrawashdeh, Y. Huang, P. Cao, and E. Lim, “A new small conformal antenna for capsule endoscopy,” in *Proc. 7th Eur. Conf. Antennas Propag. (EuCAP)*, Gothenburg, Sweden, pp. 220–223, Apr. 2013.

[46] S. Yun, K. Kim, and S. Nam, “Outer-wall loop antenna for ultrawideband capsule endoscope system,” in *IEEE Antennas Wireless Propag. Lett.*, vol. 9, pp. 1135–1138, Nov. 2010.

[47] Md. S. Miah, A. N. Khan, C. Icheln, K. Haneda, and K. Takizawa, “Antenna system design for improved wireless capsule endoscope links at 433 MHz,” in *IEEE Trans. Antennas Propag.*, vol. 67, no. 4, pp. 2687–2699, Apr. 2019.

[48] J. Faerber *et al.*, “In vivo characterization of a wireless telemetry module for a capsule endoscopy system utilizing a conformal antenna,” in *IEEE Trans. Biomed. Circuits Syst.*, vol. 12, no. 1, pp. 95–105, Feb. 2017.

[49] J. Wang, M. Leach, E. G. Lim, Z. Wang, R. Pei, and Y. Huang, “An implantable and conformal antenna for wireless capsule endoscopy,” in *IEEE Antennas Wireless Propag. Lett.*, vol. 17, no. 7, pp. 1153–1157, Jul. 2018.

[50] J. Faerber, G. Cummins, and M. P. Y. Desmulliez, “Design of conformal wideband antennas for capsule endoscopy within a body tissue environment,” in *Proc. 46th Eur. Microw. Conf.*, pp. 1223–1226, 2016.

[51] J. B. Pendry, A. J. Holden, D. J. Robbins, and W. J. Stewart, “Magnetism from conductors and enhanced nonlinear phenomena,” in *IEEE Trans. Microw. Theory Techn.*, vol. 47, no. 11, pp. 2075–2084, Nov. 1999.

[52] R. A. Shelby, D. R. Smith, and S. Schultz, “Experimental verification of a negative index of refraction,” in *Science*, vol. 292, no. 5514, pp. 77–79, 2001.

[53] R. Marqués, J. Martel, F. Mesa, and F. Medina, “Left-handed-media simulation and transmission of EM waves in subwavelength split-ring resonator-loaded metallic waveguides,” in *Phys. Rev. Lett.*, vol. 89, no. 18, p. 183901, 2002.

[54] F. Martín, J. Bonache, F. Falcone, M. Sorolla, and R. Marqués, “Split ring resonator-based left-handed coplanar waveguide,” in *Appl. Phys. Lett.*, vol. 83, no. 22, pp. 4652–4654, 2003.

[55] X. Cheng, D. E. C. Kim, and Y. Yoon, “A compact omnidirectional self-packaged patch antenna with complementary split-ring resonator loading for wireless endoscope applications,” in *IEEE Antennas Wireless Propag. Lett.*, vol. 10, pp. 1532–1535, 2011.

[56] X. Liu, Z. Wu, Y. Fan, and E. M. Tentzeris, “A Miniaturized CSRR Loaded Wide-Beamwidth Circularly Polarized Implantable Antenna for Subcutaneous Real-Time Glucose Monitoring,” in *IEEE Antennas Wireless Propag. Lett.*, vol. 16, pp. 577–580, 2017.

[57] P. M.Paul, K. Kandasamy , and M. S. Sharawi, “A triband circularly polarized strip and SRR-loaded slot antenna,” in *IEEE Trans. Antennas Propag.*, vol. 66, no. 10, pp. 5569–5573, Oct. 2018.

[58] J. J. H. Wang, “Antennas for global navigation satellite system (GNSS),” in *Proc. IEEE*, vol. 100, no. 7, pp. 2349-2355, Jul. 2012.

[59] U. U. Hussine, Y. Huang, and C. Song, “A New Circularly Polarized Antenna for GNSS Applications,” in *11th European Conference on Antennas and Propagation (EUCAP)*, pp. 1954-1956, 2017.

[60] M. Secmen and A. Hizal, “A dual-polarized wide-band patch antenna for indoor mobile communication applications,” in *Prog. Electromagn. Res.*, vol. 100, no. 100, pp. 189-200, 2010.

[61] K. N. Paracha, S. K. A. Rahim, P. J. Soh, M. R. Kamarudin, K.-G. Tan, Y. C. Lo, and M. T. Islam, “A low profile, dual-band, dual polarised antenna for Indoor/Outdoor wearable application,” in *IEEE Access*, vol. 7, pp. 33277-33288, 2019.

[62] R. Joshi, *et.al*, “Dual-band, dual-sense textile antenna with AMC backing for localization using GPS and WBAN/WLAN,” in *IEEE Access*, vol. 8, pp. 89468-89478, 2020.

[63] H. Lee, J. Tak, and J. Choi, “Wearable antenna integrated into military berets for indoor/outdoor positioning system,” in *IEEE Antennas Wireless Propag. Lett.*, vol. 16, pp. 1919-1922, 2017.

[64] S. Bi, Y. Zeng, and R. Zhang, “Wireless powered communication networks: An overview,” in *IEEE Wireless Commun.*, vol. 23, no. 2, pp. 10–18, 2016.

[65] I. Krikidis, S. Timotheou, S. Nikolaou, G. Zheng, D. W. K. Ng, and R. Schober, “Simultaneous wireless information and power transfer in modern communication systems,” in *IEEE Commun. Mag.*, vol. 52, no.11, pp. 104–110, 2014.

[66] Q. Wu, G. Y. Li, W. Chen, D. W. K. Ng, and R. Schober, “An overview of sustainable green 5G networks,” in *IEEE Wireless Commun.*, vol.24, no. 4, pp. 72–80, 2017.

[67] K. W. Choi *et al.*, “Toward realisation of long-range wireless-powered sensor networks,” in *IEEE Wireless Commun.*, vol. 26, no. 4, pp. 184–192, Aug. 2019.

[68] B. Clerckx, R. Zhang, R. Schober, D. W. K. Ng, D. I. Kim, and H. V. Poor, "Fundamentals of wireless information and power transfer: from RF energy harvester models to signal and system designs," in *IEEE Journal Selected Areas Commun.*, vol. 37, no. 1, pp. 4-33, Jan. 2019.

[69] D. W. K. Ng *et al.*, "Wireless information and power transfer: theory and practice," *Wiley Telecom*, 2019. ISBN: 9781119476795.

[70] T. D. P. Perera, D. Jayakody, S. K. Sharma, S. Chatzinotas, and J. Li, "Simultaneous wireless information and power transfer (SWIPT): recent advances and future challenges," in *IEEE Wireless Commun. Survey & Tutorials*, vol.20, no. 1, pp. 264–302, 2018.

[71] X. Zhou, R. Zhang, and C. K. Ho, "Wireless information and power transfer in multiuser OFDM systems," in *IEEE Trans. Wireless Communications.*, vol. 13, no. 4, pp. 2282–2294, Apr. 2014.

[72] K. W.Choi, S. I. Hwang, A. A. Aziz, H. H. Jang, J. S. Kim, D. S. Kang, and D. I. Kim, "Simultaneous wireless information and power transfer (SWIPT) for internet of things: novel receiver design and experimental validation," in *IEEE Internet of Things Journal*, vol. 7, no. 4, pp. 2996-3012, Apr. 2020.

[73] I. Krikidis, S. Timotheou, and S. Sasaki, "RF energy transfer for cooperative networks: Data relaying or energy harvesting?" in *IEEE Commun. Lett.*, vol. 16, no. 11, pp. 1772–1775, Nov. 2012.

[74] A. A. Nasir, H. D. Tuan, D. T. Ngo, T. Q. Duong, and H. V. Poor, "Beamforming design for wireless information and power transfer systems: Receive power-splitting versus transmit time-switching," in *IEEE Trans. Commun.*, vol. 65, no. 2, pp. 876–889, Feb. 2017.

[75] N. Janatian, I. Stupia, and L. Vandendorpe, "Joint multi-objective transmit precoding and receiver time switching design for MISO SWIPT systems," in *Proc. IEEE SPAWC*, Jul. 2016, pp. 1–5.

[76] S. Wang, L. Ma, and W. Wu, "Joint TS beamforming and Hybrid TS-PS receiving design for SWIPT systems," in IEEE Access, vol 9, pp. 50686-50699, Mar. 2021.

[77] H. Lee, K. J. Lee, H. Kim, and I. Lee, “Joint transceiver optimization for MISO SWIPT systems with time switching,” in *IEEE Trans. Wireless Commun.*, vol. 17, no. 5, pp. 3298–3312, Mar. 2018.

[78] S. Kang, H. Lee, S. Jang, H. Kim, and I. Lee, “Dynamic Time Switching for MIMO Wireless Information and Power Transfer,” in *IEEE Trans. Commun.*, vol. 67, no. 6, pp. 3978-3990, Jun. 2019.

[79] C. Peng *et al.*, "Optimal power splitting in two-way decode-and-forward relay networks", in *IEEE Commun. Lett.*, vol. 21, no. 9, pp. 2009-2012, Sep. 2017.

[80] D. W. K. Ng, E. S. Lo, and R. Schober, “Wireless information and power transfer: energy efficiency optimization in OFDMA systems,” in *IEEE Trans. Wireless Commun.*, vol. 12, no. 12, pp. 6352–6370, Dec. 2013.

[81] M. Abedi, H. Masoumi and M. J. Emadi, " Power splitting-based SWIPT systems with decoding cost," in *IEEE Wireless Commun. Lett.*, vol. 8, no. 2, pp. 432-435, Apr. 2019.

[82] D. W. K. Ng, E. S. Lo, and R. Schober, “Robust beamforming for secure communication in systems with wireless information and power transfer,” in *IEEE Trans. Wireless Commun.*, vol. 13, no. 8, pp. 4599–4615, Aug. 2014.

[83] F. Benkhelifa, K. Tourki, and M. S. Alouini, “Proactive spectrum sharing for SWIPT in MIMO cognitive radio systems using antenna switching technique,” in *IEEE Trans. Green Commun. & Networking*, vol. 1, no. 2, pp. 204-222, Apr. 2017.

[84] F. Benkhelifa and M. S. Alouini, “Prioritizing data/energy thresholding-based antenna switching for SWIPT-enabled secondary receiver in cognitive radio networks,” in *IEEE Trans. Cognitive Commun. & Networking*, vol. 3, no. 4, pp. 782-800, Dec. 2017.

[85] R. Zhang and C. K. Ho, “MIMO broadcasting for simultaneous wireless information and power transfer,” in *IEEE Trans. Wireless Commun.*, vol. 12, pp. 1989–2001, May 2013.

[86] P. Lu, X. S. Yang, and B. Z. Wang, “A two-channel frequency reconfigurable rectenna for microwave power transmission and data communication,” in *IEEE Trans. Antennas Propag.*, vol. 65, no. 12, pp. 6976-6985, Dec. 2017.

[87] H. H. Jang, K. W. Choi, and D. I. Kim, “Novel frequency-splitting SWIPT for overcoming amplifier nonlinearity,” in *IEEE Wireless Commun. Lett.*, vol. 9, pp. 826-829, Jun. 2020.

[88] K. W. Choi, S. I. Hwang, A. A. Aziz, H. H. Jang, J. S. Kim, D. S. Kang, and D. I. Kim, “Simultaneous wireless information and power transfer (SWIPT) for internet of things: Novel receiver design and experimental validation,” in *IEEE Internet of Things Journal*, vol. 7, pp. 2996-3012, Apr. 2020.

[89] M. Wagih, A. S. Weddell, and S. Beeby, “Rectennas for radio-frequency energy harvesting and wireless power transfer: a review of antenna design,” in *IEEE Antennas Propag. Mag.*, vol. 62, no. 5, pp. 95-107, Oct. 2020.

[90] H. J. Visser and R. J. M. Vullers, “RF energy harvesting and transport for wireless sensor network applications: Principles and requirements,” in *Proc. IEEE*, vol. 101, no. 6, pp. 1410–1423, 2013.

[91] S. K. Divakaran, D. D. Krishna, and N. Nasimuddin, “RF energy harvesting systems: An overview and design issues,” in *Int. J. RF Microw. Comput.-Aided Eng.*, vol. 29, no. 1, pp. 1–15, 2018.

[92] M. Cansiza, D. Altinel, and G. K. Kurt, “Efficiency in RF energy harvesting systems: A comprehensive review,” in *Energy*, vol. 174, pp. 292–309, May 2019.

[93] C. R. Valenta and G. D. Durgin, “Harvesting wireless power: Survey of energy-harvester conversion efficiency in far-field, wireless power transfer systems,” in *IEEE Microw. Mag.*, vol. 15, no. 4, pp. 108–120, 2014.

[94] T. Soyata, L. Copeland, and W. Heinzelman, “RF energy harvesting for embedded systems: A survey of tradeoffs and methodology,” in *IEEE Circuits Syst. Mag.*, vol. 16, no. 1, pp. 22–57, 2016.

[95] U. Guler and M. Ghovanloo, “Power management in wireless power-sipping devices: A survey,” in *IEEE Circuits Syst. Mag.*, vol. 17, no. 4, pp. 64–82, 2015.

[96] X. Lu, P. Wang, D. Niyato, D. I. Kim, and Z. Han, “Wireless networks with RF energy harvesting: A contemporary survey,” in *IEEE Commun. Surveys Tutorial*, vol. 17, no. 2, pp. 757–789, 2015.

[97] *Surface Mount Mixer and Detector Schottky Diodes*, Data sheet, Skyworks Solutions, Inc., Jul. 2016.

[98] S. Hemour, Y. P. Zhao, C. H. P. Lorenz, D. Houssameddine, Y. S. Gui, C.–m. Hu, and K. Wu, "Towards low-power high-efficiency RF and microwave energy harvesting," in *IEEE Trans. Microw. Theory Tech.*, vol. 62, no. 4, pp. 965–976, Feb. 2014.

[99] Z. Hameed and K. Moez, "A 3.2 v -15 dBm adaptive threshold-voltage compensated RF energy harvester in 130 nm CMOS," in *IEEE Trans. Circuits Syst. I, Reg. Papers*, vol. 62, no. 4, pp. 948–958, 2015.

[100] H. Sun and W. Geyi, "A new rectenna with all-polarization-receiving capability for wireless power transmission," in *IEEE Antennas Wireless Propag. Lett.*, vol. 15, pp. 814–817, Sept. 2015.

[101] C. Song *et al.*, "A novel six-band dual CP rectenna using improved impedance matching technique for ambient RF energy harvesting," in *IEEE Trans. Antennas Propag.*, vol. 64, no. 7, pp. 3160–3171, 2016.

[102] V. Palazzi *et al.*, "A novel ultra-lightweight multiband rectenna on paper for RF energy harvesting in the next generation LTE bands," in *IEEE Microw. Theory Techn.*, vol. 66, no. 1, pp. 366–379, 2018.

[103] S. Shen, C.-Y. Chiu, and R. D. Murch, "A dual-port triple-band l-probe microstrip patch rectenna for ambient RF energy harvesting," in *IEEE Antennas Wireless Propag. Lett.*, vol. 16, pp. 3071–3074, Oct. 2017.

[104] Y. Shi, Y. Fan, Y. Li, L. Yang, and M. Wang, "An efficient broadband slotted rectenna for wireless power transfer at LTE band," in *IEEE Trans. Antennas Propag.*, vol. 67, no. 2, pp. 814–822, 2019.

[105] C. Song, Y. Huang, J. Zhou, J. Zhang, S. Yuan, and P. Carter, "A high-efficiency broadband rectenna for ambient wireless energy harvesting," in *IEEE Trans. Antennas Propag.*, vol. 63, no. 8, pp. 3486–3495, 2015.

CHAPTER 3. A NOVEL COMPACT WIDEBAND ANTENNA WITH SPLIT-RING RESONATORS FOR IMPLANTABLE/INGESTIBLE APPLICATIONS

Having examined the development of implantable and ingestible antennas and highlighted the possibility and benefits of utilising metamaterials for these applications in Chapter 2, it is now necessary to focus in detail on the design of a general antenna structure utilising metamaterials that is able to operate for both implantable and ingestible WBAN applications with robust performance.

In this chapter, a compact wideband loop antenna with split-ring resonators (SRRs) is proposed for both implantable and ingestible applications. The operating frequency band of this antenna is from 307 MHz~3500 MHz, which covers all licensed frequency bands that could be used in applications requiring implantable or ingestible antennas, as discussed in Chapter 1. This wideband coverage enables the accommodation of frequency detuning, and hence provides stable performance inside a realistic body environment. The characteristics of SRRs have been explored regarding radiation performance, which verified their ability to aid in reducing power loss and hence improve radiation efficiency.

Considering the operating conditions for ingestible applications (for example the wireless capsule endoscope (WCE)) are more complex, a capsule-shaped structure is selected as it is commonly used in these applications. By careful tuning and optimising, this novel antenna design is the first to offer such a wide impedance bandwidth, good radiation efficiency, and can work be utilised in both ingestible and implantable applications (e.g., WCE and blood glucose monitoring implant) without requiring remodelling or testing.

3.1 Antenna Background

Research relating to biomedical telemetry has become intensive owing to its importance for therapy and healthcare monitoring in the WBAN domain [1], [2]. One popular application is the wireless capsule endoscope (WCE), which is a capsule-shaped device that can collect information while passing through the GI tract and transmitting it to a nearby monitoring or controlling device for post-processing [3]. Antenna design requirements for such an application include sufficient operating bandwidth, compact size, good isolation from body tissues, and adherence to strict human safety restrictions.

Different from an implantable device, a typical WCE is composed of a dome, light-emitting diodes (LEDs), a sensor pack, batteries, and an antenna [4]. The device's antenna's operating characteristics are more sensitive to detuning than in other applications due to the dynamically varying material properties of the environment the capsule must pass through. Among the licensed allocated frequency bands listed in Chapter 1, the MICS 402~405 MHz, MedRadio 433.0~434.8 MHz, and ISM 2.45 GHz bands are often used by WCEs [5]-[8]. Considering the volume and types of potential data that could be obtained from the human body and the fact that data types would differ concerning factors such as gender, age, or other physical conditions, it is of interest to maximise the available bandwidth to ensure that any detuning due to the variable environmental factors does not severely affect performance.

In comparing the two common structures of ingestible antennas in terms of achievable bandwidth in Chapter 2, adoption of a conformal loop structure (bent onto the outer shell of the capsule) with a flexible substrate material is the most suitable selection in this work, since it commonly realises wide bandwidth [9]-[11]. As for size reduction, some designs have made use of high permittivity substrates, fractal structures, or shorting pins to miniaturise the size such as [12]-[17]. However, most of these are optimised only for a single frequency band to maintain a relatively high radiation efficiency.

Recently, the synthesised metamaterial SRR and complementary split-ring resonator (CSRR) have gained increasing attention for use in biomedical applications. Their ability to provide a negative permeability or permittivity near their resonant point brings a new approach to size miniaturisation and multiband operation [18]-[20]. The influence on power loss and radiation performance over a wideband inside body tissues will be further investigated and exploited in this research.

This chapter addressed four main aspects as follows:

1. Design and optimise a SRR equipped loop antenna with flexible substrate material to achieve a wide operation bandwidth, covering all bands of interest.

2. Investigate the possibility of using the antenna model for implantable applications.

3. Examine the use of SRRs on impedance matching to achieve robust performance in both an anatomical body model and real-world environment.

4. Explore the use of SRRs to achieve an overall improvement in radiation efficiency and a general decrease in SAR around the antenna over the frequency bands of interest.

To fulfil the above goals, this chapter is structured as follows: Section 3.2 provides detailed information on the proposed design including the determination of the basic antenna structure. The optimisation process is outlined and the effects of various factors on antenna performance such as SRRs and typical implantable device characteristics are also discussed in this section. Section 3.3 investigates the antenna radiating properties and associated SAR values. Measurement setups and experimental outcomes are presented in Section 0 and the novelty of this design is summarised in Section 3.5. The main achievement of the work presented in this chapter is a compact loop antenna utilising SRRs for both ingestible and implantable applications. The desired licensed frequency bands covered by the antenna are the MICS band (402~405 MHz), the MedRadio bands (401~406, 413~419, 426~432, 438~444, and 451~457 MHz), and the ISM bands (433.1~434.8, 868.0~868.8, 902.8~928.0 MHz, and 2.4~2.48 GHz),

offering the ability to provide various operating functions such as wireless communication and/or wireless charging on different bands.

3.2 Design Optimisation

The loop antenna, as a magnetic type antenna, is proposed as the starting point for the design of an antenna for ingestible/implantable applications. Having a smaller E-field than an electric type of antenna in the antenna near field region reduces the power absorbed by human body tissues and correspondingly increases the power radiated, leading to higher power efficiency inside the human body. Considering the requirements of an efficient bio-used antenna discussed above, a general design methodology has been formulated as detailed in Fig. 3-1.

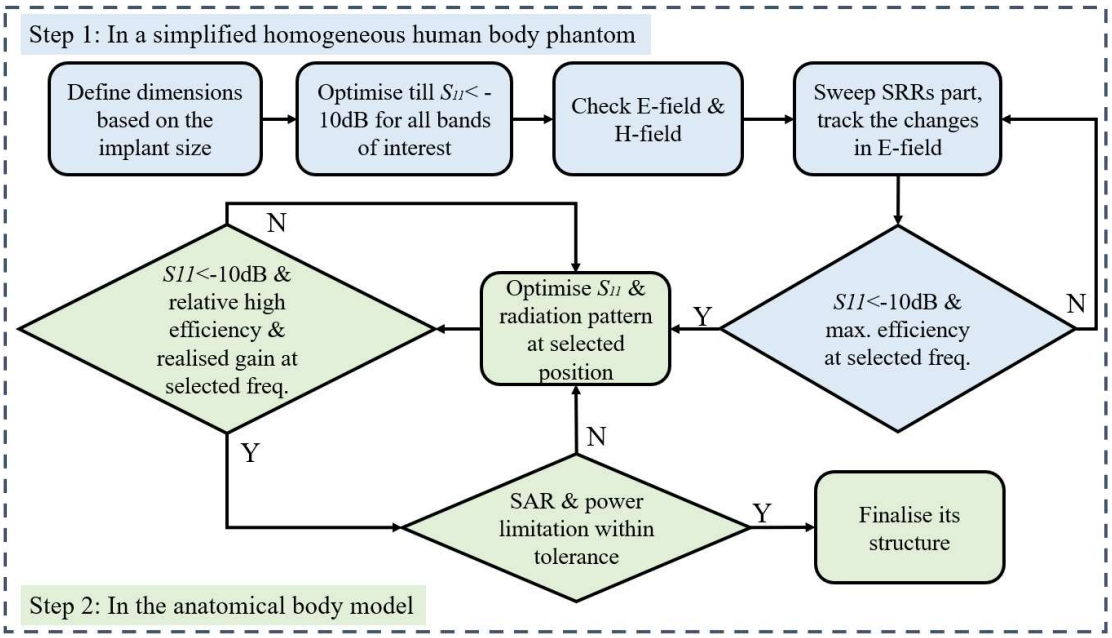

Fig. 3-1: Schematic of the optimisation process.

The first step is to determine the original dimensions of the antenna according to the regular capsule size (within 26 mm in height and 5.5 mm in radius). The proposed antenna structure can then be optimised in a simplified homogeneous human body material phantom with aid of the CST Microwave Suite 2017 software (CST 2017). This software can provide results of reflection coefficients and E-/H-field strengths which helps with the optimisation process. Initially, a simplified phantom is used

enabling an initial set of optimised parameters to be found within a relatively short simulation time. Based on this initial set of optimised parameters, the proposed antenna can be placed in an accurate anatomical body model at different locations and in various orientations, with the corresponding feedback being used for evaluation and re-optimisation. The optimisation of the SRRs (parameters including *a*, *lb*, *gap*, *w1* and *wf2* defined in Fig. 3-2) is mainly based on the reflection coefficients (S_{11}) and radiation efficiencies at 403, 433 MHz, and 2.45 GHz as they are often chosen by researchers as representative of the bands of interest. A trade-off between S_{11}, realised gain, and radiation efficiency has been carefully considered to ensure robust performance in the human body, where detuning may occur as well as maximising the potential link budget of the intended communication system. Furthermore, SAR and power limitations have also been considered at this stage to prevent hazardous heating of the body's biological tissues.

The proposed antenna is designed on RO3010 substrate with relative permittivity ε_r = 10.2, loss tangent tanδ = 0.0035, and thickness 0.6 mm. The proposed design is a three-layer structure from inside to outside composed of substrate, copper, and superstrate (the superstrate uses the same material as the substrate). The copper layer is 0.035 mm thick. As is shown in Fig. 3-2, SRRs are adopted at both sides around the loop structure, whose cell dimensions are mainly limited by the available physical space within the loop structure. The dimensions of the SRR unit cell are optimised and tuned to provide maximum antenna matching and radiation efficiency with S_{11} < - 10 dB for 403, 433 MHz, and 2.45 GHz. The overall dimension of the planar antenna is 18 × 18 × 1.235 mm^3 (including superstrate) and the 3-dimensional (3-D) size of the conformal shape (bent onto the outer wall of a capsule case) is 18 mm in height and 3.2 mm in radius. Table 3-1 provides the optimised geometrical parameters of this design after conducting parametric studies with the aid of CST 2017.

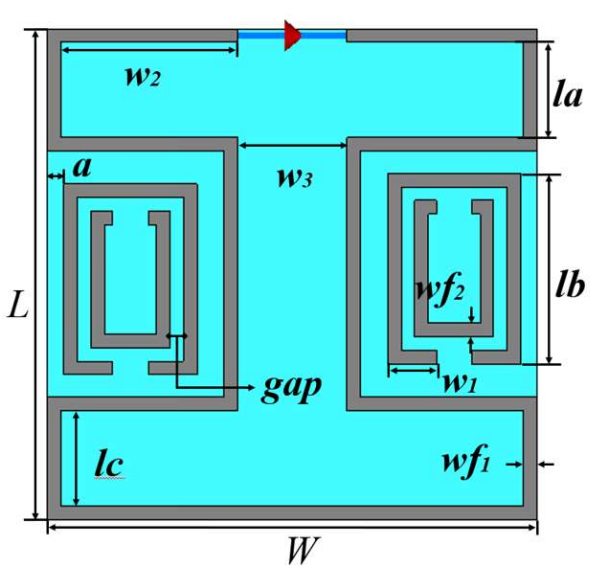

(a)

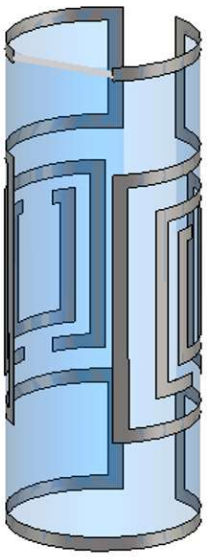

(b)

Fig. 3-2: (a) Planar design of the proposed antenna. (b) 3-D conformal model of the designed antenna (substrate colour here is set to be transparent blue for display purpose).

Table 3-1: Optimised Antenna Dimensions (Millimetre)

Parameter	Value	Parameter	Value	Parameter	Value
L	18	*lc*	3.5	wf_1	0.5
W	18	w_1	1.8	wf_2	0.5
la	3.5	w_2	6.5	*gap*	0.5
lb	7.0	w_3	4.0	*a*	0.6

As previously discussed, a simplified homogeneous human body phantom was initially used in the optimisation process to shorten simulation time. This initial phantom was an elliptical cylinder 120 × 80 ×100 mm^3 with ε_r = 56 and conductivity σ = 0.8 S/m [8], [21]. To verify the influence of SRRs, both structures (with and without SRRs) are simulated in the simplified homogeneous human body phantom. The simulated S_{11} of the original loop structure with and without SRRs in a cylindrical geometry with an internal radius of 3.2 mm is depicted in Fig. 3-3 and it shows that employing SRRs reduces loop inductance and therefore improves matching. The operating band

(S_{11} <-10 dB) is wide, covering all licensed frequency bands used for implantable and ingestible applications (MICS band, MedRadio bands, and ISM bands).

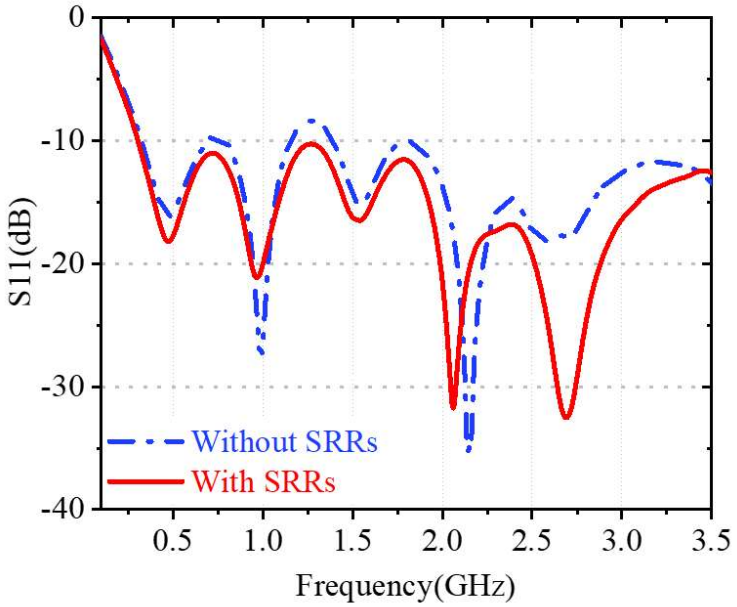

Fig. 3-3: S_{11} with and without SRRs in the simplified body phantom.

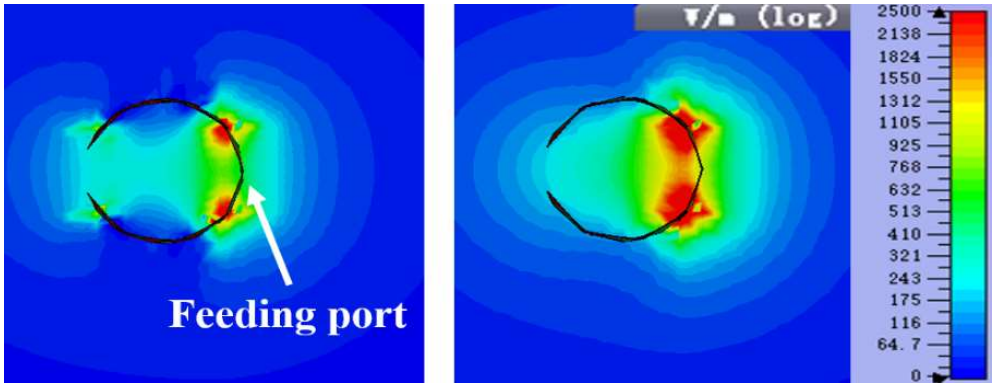

Fig. 3-4: Top view of the E-field distribution around the proposed antenna in the simplified body phantom at 403 MHz: (a) with SRRs, (b) without SRRs.

Fig. 3-4 provides cross-sectional contour plots of the scalar electric near field (E-field) across the centre of the antenna with and without SRRs. The E-field is reduced when the SRRs are added to the design, resulting in a drop in the absorbed power and SAR value (only shown at 403 MHz for brevity but the conclusion is general to other frequencies). The radiated power increases due to the reduction in power absorbed by body tissues and therefore radiation efficiency and antenna realised gain are enhanced

inside a lossy human body model. This is verified by the numerical results and can be seen in Section 3.3.

3.2.1 Influence of Capsule Dimensions

According to [21], [22], attaching a conformal antenna to the outer wall of the capsule case can save space for other essential components inside the shell. Therefore, the effects of bending curvature on the antenna performance are evaluated to ensure the antenna is suitable for use in a range of capsule-based systems. More particularly, it is important to know the minimum radius at which the antenna still functions within design requirements. To test the influence of varying the radius, the proposed antenna is bent on to capsule shells of the same height and radii values of 3.0, 3.5, 4.5, 5.0, and 6.5 mm. Corresponding results of S_{11} are shown in Fig. 3-5. These show that the performance of the antenna is stable across all design bands for capsule radii under 6.5 mm. For a radius of 6.5 mm, this antenna still meets the design requirements for the MICS band (402~405 MHz) and some of the ISM bands (433.1~434.8, 868.0~868.8 and 902.8~928.0 MHz). After carefully tuning within the optimal range, the best operation occurs at a radius of 3.2 mm. Therefore, this is the radius used in the following simulations and experiments.

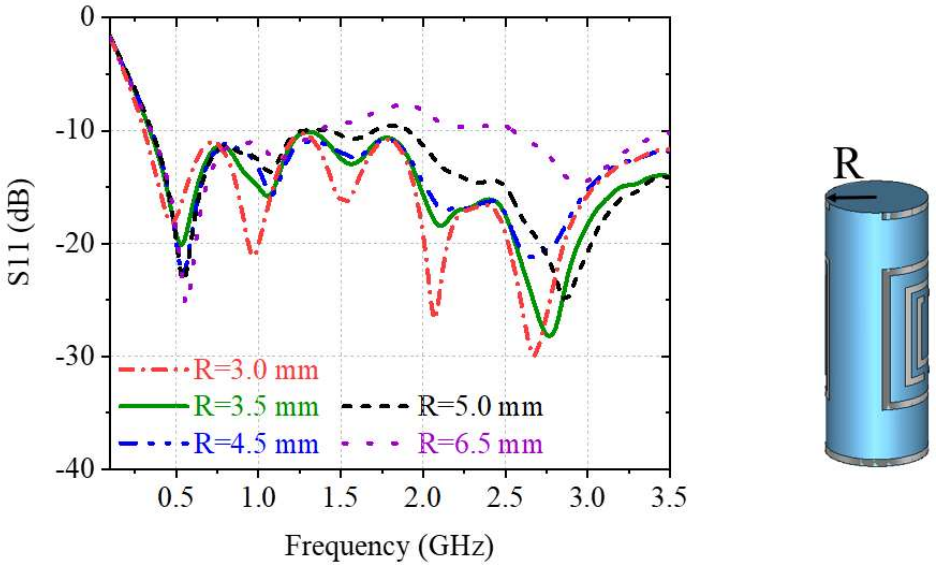

Fig. 3-5: Effects on S_{11} with varying radii.

3.2.2 Influence of Internal Batteries

Considering the internal components mentioned previously, the battery is the main solid component and is conducting which may influence antenna performance [21], [23]. Therefore, it is necessary to investigate the impact of locating a battery inside the shell. To simplify the corresponding model, a perfect electric conductor (PEC) is inserted to represent the battery. Simulated S_{11} results with and without a battery are illustrated in Fig. 3-6 for two different battery sizes. The inclusion of a battery is seen to result in a frequency shift. The lower resonant frequencies are shifted from 477 MHz and 0.96 GHz to 577 MHz and 1.28 GHz respectively, and the resonant frequency at 2.5 GHz is upshifted by 150 MHz. The operating bandwidth of the proposed antenna though remains almost the same and still covers all frequency bands of interests despite the frequency shifts.

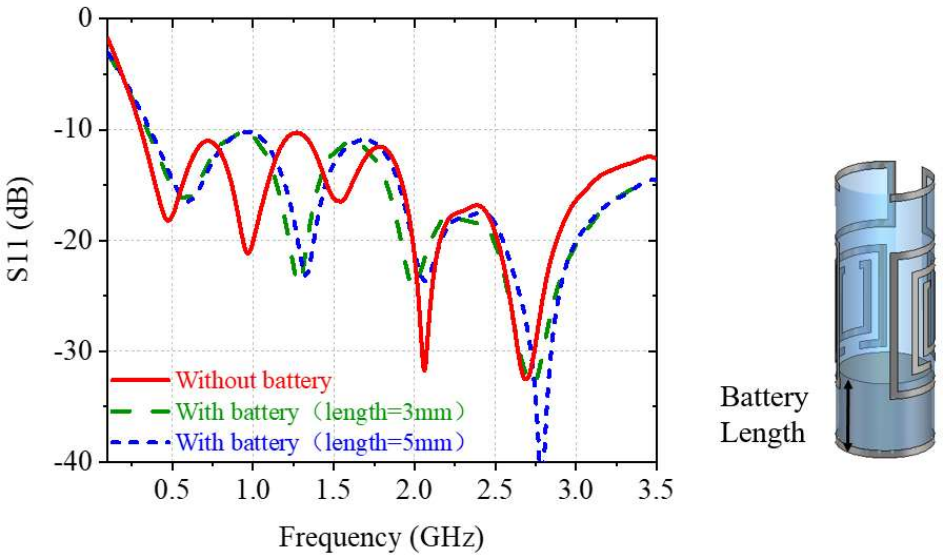

Fig. 3-6: Simulated S_{11} with internal batteries of different heights.

3.2.3 Influence of Biocompatible Insulation

To avoid direct contact between the radiator and body tissues and provide electrical isolation, a biocompatible polyamide layer is added to the capsule surface in real implantation cases. This is also required as the substrate material used, RO3010, which is not biocompatible. The low-loss biocompatible polyamide used has the material

properties ε_r = 3.5, tanδ = 0.004. It is wrapped around the outer surface of the designed antenna to offer the necessary isolation from the body tissues. This encapsulation layer reduces the conducting effects of the human body and coupling between the implant and the surrounding human tissue [24]. Effects of different coating thicknesses are plotted in Fig. 3-7, which illustrates frequency shifts increase with coating thickness. The thickness of polyamide providing optimal antenna performance is found to be 17 μm.

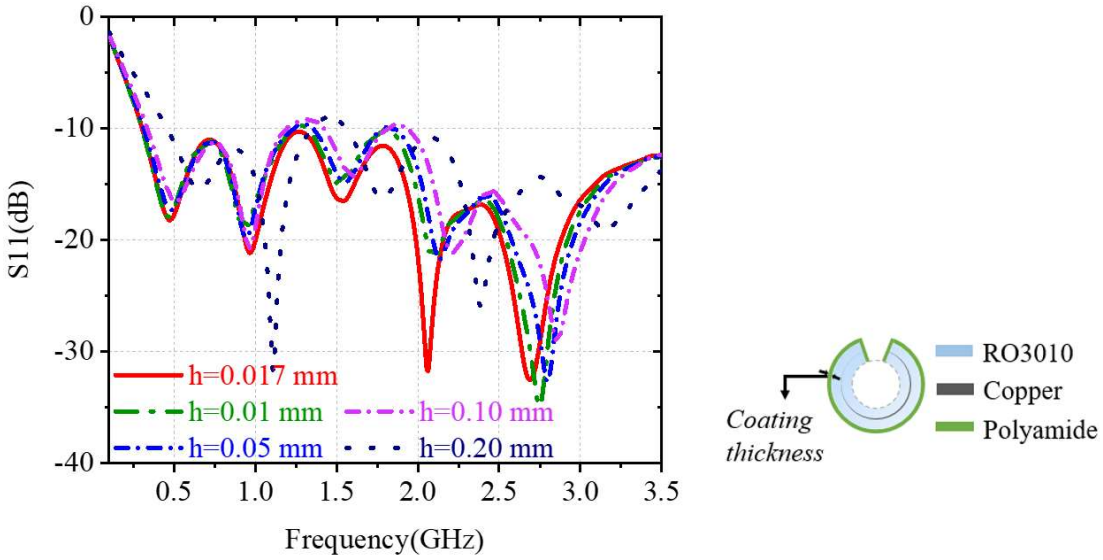

Fig. 3-7: Effects on S_{11} with different thicknesses of the coating material.

An alternative to using a coating would be to use a biocompatible material for the antenna design directly as discussed in Chapter 2 [24]. The substrate and copper could be replaced with Al_2O_3 (ϵ_r = 9.8, tanδ = 0.008) and silver palladium (AgPd) respectively. Fig. 3-8 illustrates the result of making these changes and shows that the resonant frequencies are shifted upwards to some extent. One reason is that the relative permittivity of Al_2O_3 is slightly lower than that of RO3010. The change observed in impedance bandwidth is approximately 40-55 MHz, though the antenna still covers all bands of interest. However, the RO3010 substrate remains the preferred choice due to the relative ease of manufacture and costs. The biocompatible structures could be studied as future work.

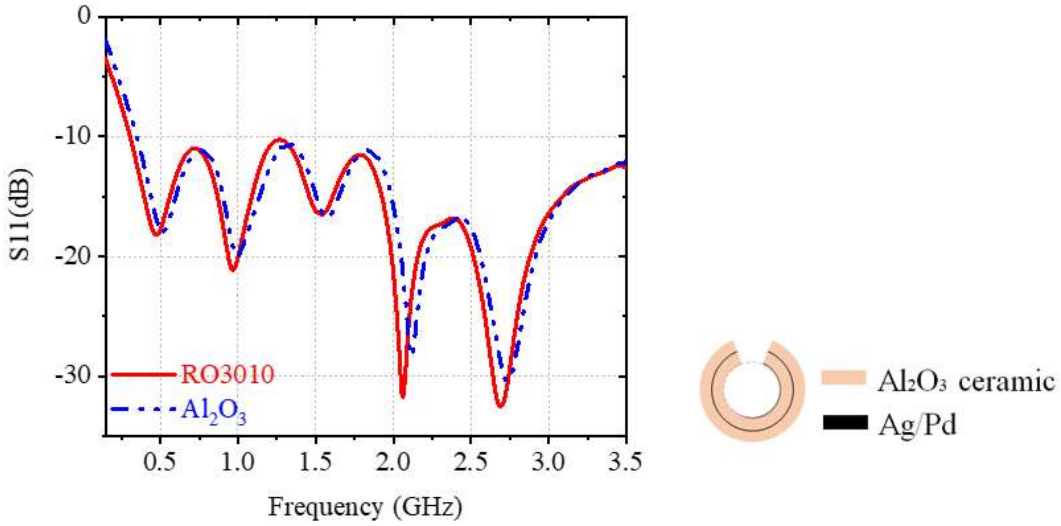

Fig. 3-8: Effects on S_{11} with Al_2O_3 substrate and superstrate.

3.2.4 Influence of Different Organs

The influence of the various organ material properties that would be encountered by an ingestible antenna such as stomach ($\varepsilon_r = 67.45$, $\sigma = 1.00$ S/m), colon ($\varepsilon_r = 62.54$, $\sigma = 0.86$ S/m) and small intestine ($\varepsilon_r = 66.06$, $\sigma = 1.90$ S/m) on the antenna S_{11} using the same polyamide coating and elliptical cylinder shape body model is investigated in Fig. 3-9. The resonant frequencies for both the stomach and the small intestine are almost the same since their relative permittivities are close (a slight downshift in S_{11} for the stomach case). Moreover, there is a slight upshift in S_{11} for the colon case, which has a considerably smaller relative permittivity.

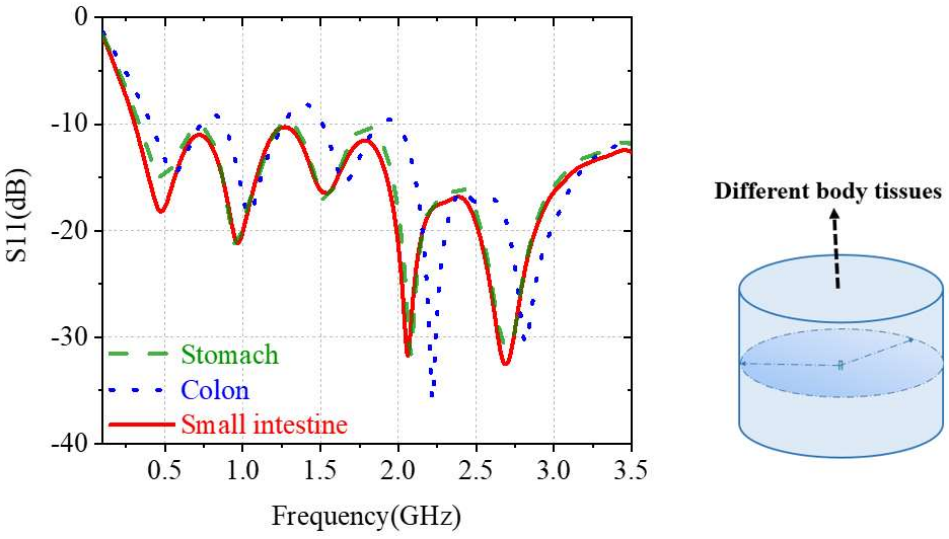

Fig. 3-9: Effects on S_{11} with different biological tissues.

The dielectric properties of the selected human tissues vary with frequency. For example, the dielectric properties of the small intestine are ε_r = 66.06, 65.29, 59.71, 59.39, 54.43 and σ = 1.90, 1.92, 2.14, 2.17, 3.17 S/m at 403, 433, 868, 915, and 2450 MHz respectively. The trend of ε_r decreases and the trend of σ increases with frequency. However, this does not invalidate the use of a single frequency material property for the selected human tissue model. Based on the investigation above, a bandwidth that covers all bands of interest is maintained whilst resonant frequencies slightly shift as dielectric properties vary. Therefore, it is reasonable to design it in a homogeneous tissue (using its dielectric property at a single frequency) for simplicity as the antenna maintains acceptable performance with dielectric property variation within the ranges seen.

3.2.5 Possible usage for implants

The proposed antenna has also been evaluated using the same elliptical cylinder shape body model shown in Fig. 3-3 but with muscle equivalent dielectric properties (e.g., ε_r = 51.9, and σ = 1.74 S/m at 2.45 GHz) to explore the possibility for implantable applications. Fig. 3-10 depicts the corresponding S_{11} for both a simplified homogeneous human body phantom case and an anatomical body model case for comparison, which provides evidence supporting the use of the antenna for an implant device within muscle tissue (e.g., implant in the human arm as a blood glucose monitoring implant). Details of the selected anatomical body model are provided in Section 3.3, as well as radiation patterns to show whether the proposed antenna can provide robust and desirable performance in a human muscle environment.

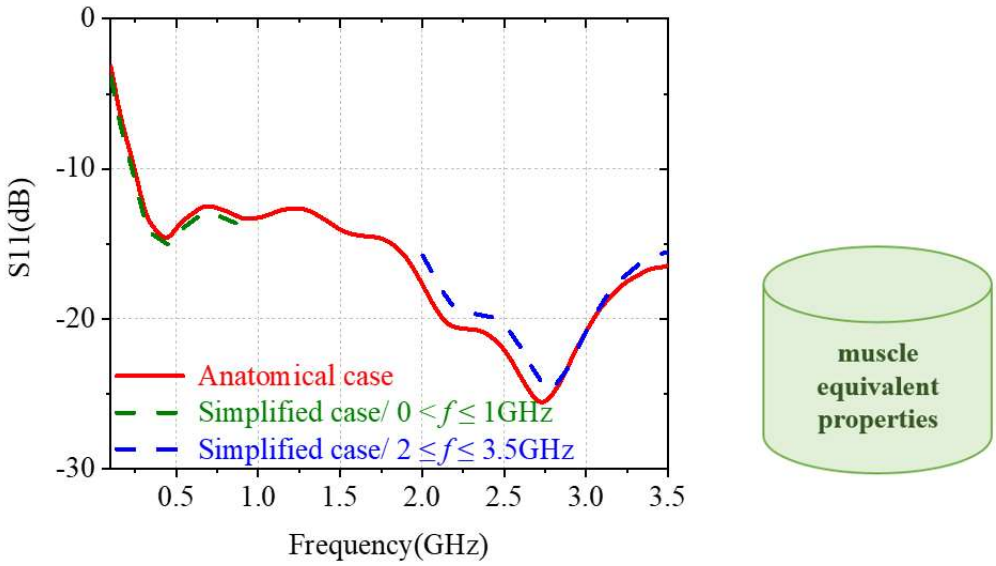

Fig. 3-10: Simulated S_{11} when the antenna is implanted inside the human arm.

3.3 Radiation Efficiencies and SAR Values

3.3.1 Evaluation of Gain and Radiation Efficiency

Accurate simulations of bio-EM propagation require accurate models of the complex anatomical structure and tissue properties, which are typically age, frequency and temperature dependant. Based on the previous 1-D analysis in the simplified homogeneous human body phantom, an anatomical body model, Gustav from the CST Voxel family, is used for further far-field simulations as it has a multilayer heterogeneous structure of much better resemblance to a real human body. This voxel model represents a male with a height of 176 cm and a weight of 69 kg. Both front and side views are given in Fig. 3-12.

Radiation becomes directional in this model owing to the different absorption levels from different body tissues around the antenna. In general, the maximum radiation is achieved when the antenna radiates outwards from the body (in the off-body direction towards free space). As is stated in Section 3.2, the optimisation is about a trade-off between S_{11}, realised gain, and radiation efficiencies at 403, 433 MHz and 2.45 GHz. After optimisation and selection of best-case geometry and coating, simulated two-dimensional (2-D) polar plots of antenna patterns in the *E-plane* and *H-plane* at 403

and 433 MHz in the small intestine and at 2.45 GHz in the arm are depicted in Fig. 3-12 (a), (b), and (c) respectively.

Fig. 3-11: Gustav voxel body model for CST anatomical simulations.

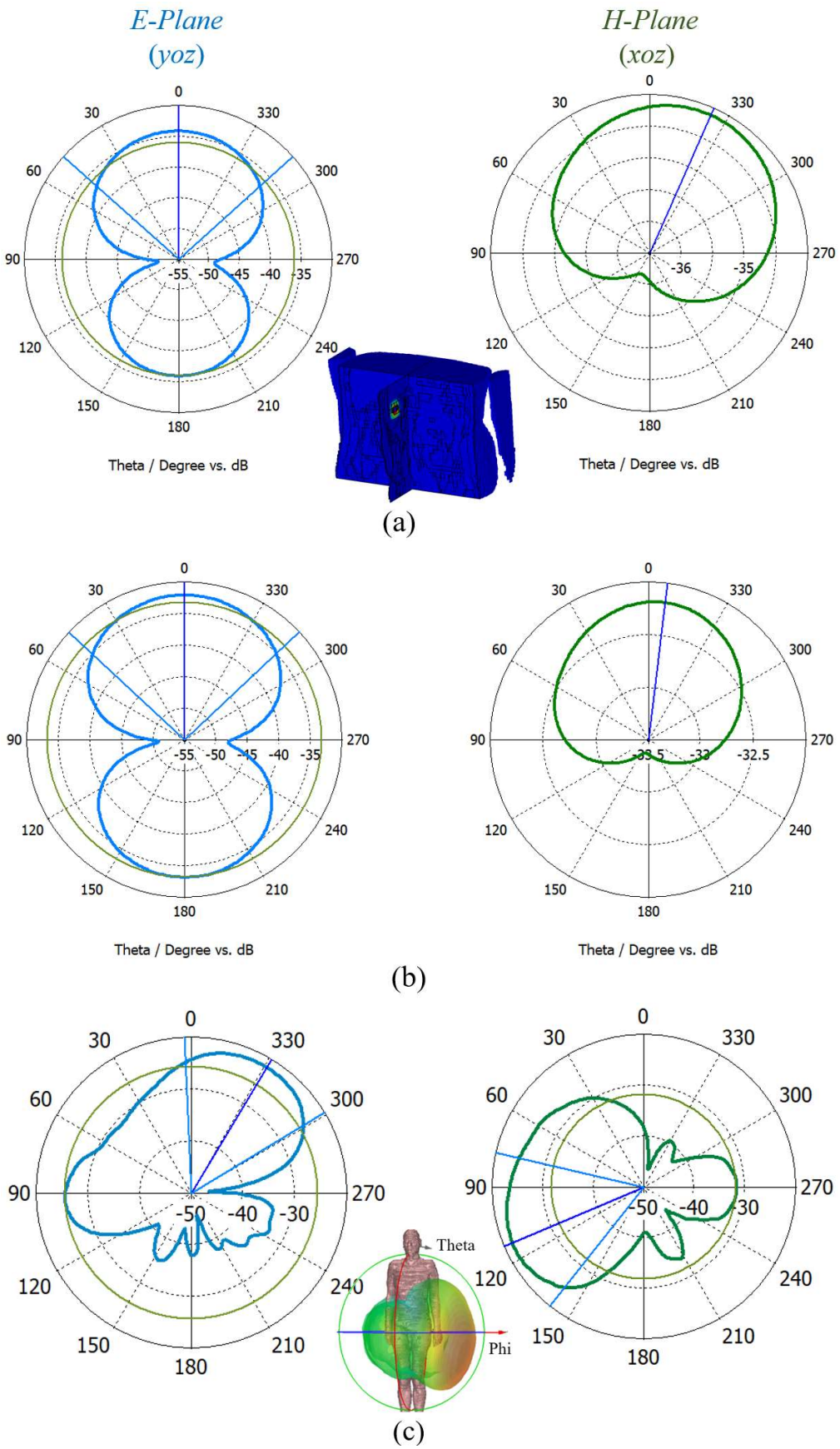

Fig. 3-12: Simulated 2-D patterns of the proposed antenna over *E-plane* and *H-plane* at (a) 403 MHz; (b) 433 MHz in the small intestine; (c) 2.45 GHz in the arm.

It demonstrates that this antenna has near symmetrical patterns in the *E-plane* with maximum gain values of -34.3 dBi and -32.1 dBi at 403 and 433 MHz respectively when it is placed in the small intestine environment. For the arm-case, the target gain value, which is proportional to the antenna radiation efficiency directly, is required to be equal to or larger than -20 dBi at 2.45 GHz inside an anatomical body model in order to build a reliable communication link of 2 m according to [25]. From Fig. 3-12(c) the maximum gain equals to -18.4 dBi, which meets the target. Larger radiation efficiencies and gains are achieved at higher frequencies, which is in agreement with findings published in [26]. Radiation efficiency and realised gain with and without SRRs have also been computed and have been summarised in Table 3-2. It indicates that the radiation efficiency and realised gain increase when the SRRs are employed.

Table 3-2: Radiation Efficiency and Realised Gain with and Without SRRs

f **(MHz)**	**Radiation Efficiency (%)**		**Realised Gain (dBi)**	
	With	Without	**With**	Without
403	**0.025**	0.023	**-34.3**	-35.7
433	**0.039**	0.033	**-32.1**	-33.9
868	**0.248**	0.116	**-26.6**	-27.6
915	**0.264**	0.190	**-26.0**	-28.0
2450	**0.414**	0.284	**-18.4**	-22.2

3.3.2 Evaluation of Specific Absorption Rate

Water, which forms 70% of a cell's mass, absorbs energy from an electromagnetic field, converting that energy into heat. This could possibly lead to damage to the characteristics of cells. To avoiding hazardous tissue heating problems, implantable devices require certification by governmental authorities, and these certifications are mainly based on SAR. The SAR standards determine how much energy is allowed to be safely absorbed by the human body. According to IEEE standards, SAR averaged over any 1 g of tissue in the shape of a cube is restricted to 1.6 W/kg [27]. Thus, the maximum applied/received input power on the antenna should satisfy this limitation. One common method used to calculate SAR values is to use the E-field strength [28]. Thus, SAR (W/kg) can be calculated by (3.1):

$$SAR = \frac{P}{\rho} = \frac{\sigma |E|^2}{\rho} \tag{3.1}$$

where P (W/m^3) is the power loss density, σ (S/m) is the conductivity of the selected tissue, $\boldsymbol{E}$ (V/m) is the effective value of the electric field intensity within the tissue, and ρ (kg/m^3) is the mass density of the tissue.

Computations of SAR values for this work are conducted by CST 2017 using the Gustav anatomical body model and are summarised in Table 3-3. The simulated maximum 1 g average SAR value for a transmitter are 216 and 203 W/kg at 403 MHz and 2.45 GHz respectively at an input power of 1 W. Use of SRRs here decreases the SAR by 88 and 62 W/kg at 403 MHz and 2.45 GHz respectively, allowing increased transmit powers of 7.41 and 7.88 mW (8.70 and 8.97 dBm) respectively, with SAR limits of 1.6 W/kg.

Table 3-3: SAR Values for the Proposed Antenna

***f* (MHz)**	403	433	868	915	2450
Max 1g-avg SAR (W/kg) without SRRs	304	284	278	272	265
Max 1g-avg SAR (W/kg) with SRRs	**216**	**213**	**211**	**205**	**203**
Allowed transmitted power level (mW)	7.41	7.51	7.58	7.80	7.88

3.4 Realisation and Measurements

The optimised design was manufactured using an LPKF milling machine (S103) on RO3010 substrate and then rolled onto a 3-D printed model to form a cylindrical shape. The cylindrical prototype and the fabricated antenna with its superstrate are presented in Fig. 3-13(a). Measurements of its performance are conducted using the homogeneous liquid phantom mixture method proposed in [29]. The recipes for the tissue-simulating liquid at 403 MHz and 2.45 GHz for WCE are summarised in Table 3-4 and both are used for measurements to decrease possible errors. The prototype is connected to a calibrated Agilent E5071C vector network analyser (VNA) port with a standard 50 Ω RF cable. The measurement setup is shown in Fig. 3-13(b), where the antenna is placed at the centre of a plastic beaker filled with the tissue-simulating liquid.

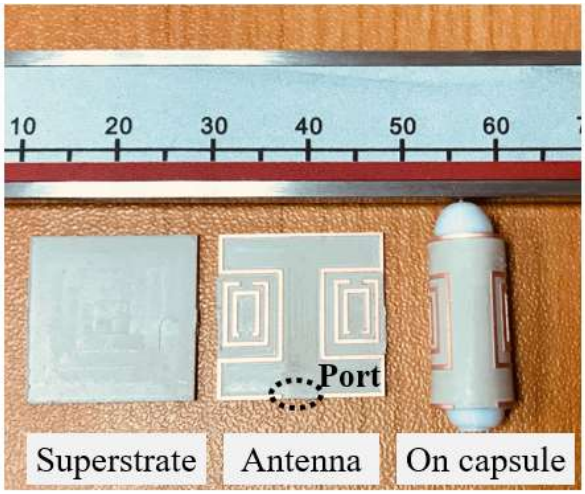

(a)

(b)

Fig. 3-13: (a) Photograph of the fabricated superstrate and antenna (b) Measurement of the proposed antenna in the tissue-simulating liquid.

Table 3-4: Recipes for the Tissue-Simulating Liquids

f **(MHz)**	**Sugar**	**NaCl**	**De-ionized water**	**HEC**	**Diacetin and Glycol**	**Triton X-100**
403	45.17%	2.98%	51.3%	0.5%	0.05%	--
2450	--	--	58.2%	--	5.1%	36.7%

Reflection coefficient results from the VNA are shown in Fig. 3-14 compared with the simulation results. The blue dotted line represents S_{11} using the liquid phantom recipe at 403 MHz and the green dashed line shows S_{11} with the 2.45 GHz liquid recipe. The resonant frequencies shift in comparison to the simulated values and some discrepancies are seen to exist while both the simulated and measured results are well below -10 dB and in good agreement at all frequencies of interest. Frequency shifting may be caused by the air gap between the superstrate and antenna. Fabrication errors and connectivity issues may also give rise to differences.

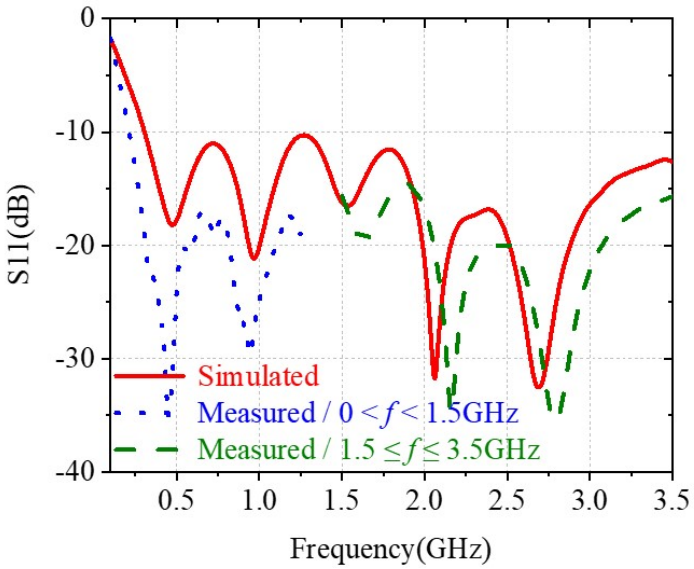

Fig. 3-14: Measured and simulated S_{11} of the proposed antenna.

3.5 Novelty

Although there are some metamaterial-based designs proposed for implantable antennas published in previous studies [18], [30], [31], they were only used to miniaturise the antenna and obtain resonances at additional frequencies by coupling to another radiator (e.g., SRR coupled to a spiral). In this work, SRRs are utilised to improve the overall radiation from the antenna regardless of the multiple operating frequency bands. This is an interesting path of investigation as normally SRR and CSRR are introduced to reduce the structure size. Moreover, it has been shown in this work that a metamaterial-based structure SRR can reduce the E-field, SAR value, and increase efficiency. Table 3-5 lists comparisons of this work to others in terms of SRR/CSRR functionality.

Table 3-5: Comparisons of the Proposed Antenna with Other Metamaterial Work

Ref.	***f*** **(MHz)**	**Type**	**Function of metamaterial units**
[32]	1200	CSRR	Miniaturise size
[30]	2400~2480	CSRR	Miniaturise size
[31]	402~455, 2400~2480	SRR	Miniaturise size & obtain a new resonance frequency by coupling to a spiral
This work	**307~3500**	**SRR**	**Reduce E-field & power loss & enhance radiation efficiency**

Some of the published SRR or CSRR based antennas including those in [30] and [32] exhibit narrow bandwidths. In this work, the designed antenna is wide in bandwidth and has a relatively good radiation efficiency. It brings about the opportunity to be applied in both ingestible and implantable WBAN applications.

According to the discussions in Section 3.2.4 and Section 3.2.5, this design functions as per design requirements in different human body tissues such as the small intestine, stomach, colon and human arm. To the best knowledge of the author, this bio-antenna which can be used for both wireless capsule endoscopy and monitoring implant with a reasonable and desirable wideband performance is the first of its kind in published materials. The final dimension of the structure has been fully considered for those operating environments. Besides, a comparison table with other recent published work in terms of size, realised gain, and SAR values is provided in Table 3-6. This antenna has a reasonably wide operation frequency band, with relatively low SAR and comparable realised gain. Therefore, it can be treated as a potential candidate for WBAN communication due to its overall good performance.

Table 3-6: Comparisons of the Proposed Antenna with Other Work

Ref.	***f* (MHz)**	**Size (*L* x *R*) mm^2**	**Realised Gain (dBi)**	**Radiation Efficiency**	**Max 1g-avg SAR (W/kg)**
[8]	284~825	17 × 3	-31.5 (at 403)	NA	913 (at 403)
[33]	2290~2530	15 × 5	-44.5 (at 2450)	NA	368.7 (at 2450)
[34]	902~928	26 × 5.5	-35.7 (at 915)	NA	NA
[35]	721~1705	22 × 5.5	-28.2 (at 915) -29.4 (at 1400)	0.11% (at 915) 0.04% (at 1400)	NA
[36]	296~589	15 × 4.6	-33.6 (at 434)	NA	340.6 at port 1 322.3 at port 2 (at 434)
[37]	1400	26 × 5.5	-26.1	0.05%	NA
This work	**307~3500**	**18 × 3.2**	**-34.3 (at 403)** **-32.1 (at 433)** **-26.6 (at 868)** **-26.0 (at 915)** **-18.4 (at 2450)**	**0.025% (at 403)** **0.039% (at 433)** **0.248% (at 868)** **0.264% (at 915)** **0.414% (at 2450)**	**216 (at 403)** **213 (at 433)** **211 (at 868)** **205 (at 915)** **203 (at 2450)**

(*NA: not available)

3.6 Summary

In this chapter, a wideband flexible loop antenna with SRRs for ingestible and implantable applications in the WBAN domain has been proposed, designed, fabricated and tested. The designing procedure methodology has been discussed, which includes optimisation in a simplified homogeneous human body phantom followed by further fine tuning in an anatomical body model. The optimisation at the first step has given a set of parameters to obtain the best reflection coefficients and maximum possible radiation efficiencies at 403, 433 MHz and 2.45 GHz within a relatively short simulation time. Evaluation in the anatomical body model has been carried out with these values of parameters. Antenna gain at potential positions of practical implantation has been compared to the pre-defined value according to the design requirement (equal to or larger than -20 dBi at 2.45 GHz). Trade-off's between various characteristics have been carefully considered to ensure robust performance inside the human body where detuning happens.

The structure of the proposed antenna has been simulated in homogeneous tissue phantoms and evaluated regarding the possibility for implantable application usage and the effects of capsule dimensions, internal batteries, biocompatible insulation, and material properties of different organs. The Gustav human body model has then been utilised to further improve performance.

A homogeneous mixture has been made and a calibrated VNA with a 50 Ω RF cable has been utilised for the practical measurements. Results achieved from measurements showed good agreement with the simulations. The novelty of exploiting SRRs has been analysed and comparisons have been made with other related published works. The SRRs not only allow miniaturisation of overall antenna size but also improve matching and enhance radiation efficiency. This proposed design works over the MICS band, the MedRadio bands, and the ISM bands, which makes it suitable for use in low power or passive implant communication systems with acceptable performance.

3.7 References

[1] G. Virone *et al.*, “An advanced wireless sensor network for health monitoring,” in *Proceedings of the Transdisciplinary Conference on Distributed Diagnosis and Home Healthcare*, Apr. 2006.

[2] C. P. Ráez, “Overview of wireless sensor networks applications in medical care,” in *Proceedings of the Second International Symposium on Medical Information and Communication Technology*, Dec. 2007.

[3] A. Kiourti, K. A. Psathas, and K. S. Nikita, “Implantable and ingestible medical devices with wireless telemetry functionalities: A review of current status and challenges,” in *Bioelectromagnetics*, vol. 35, no. 1, pp. 1–15, Jan. 2015.

[4] P. M. Szczypinski, R. D. Sriram, P.V. J. Sriram, and D. N. Reddy, “A model of deformable rings for interpretation of wireless capsule endoscopic videos,” in *Med. Image Anal.*, vol. 13, no. 2, pp. 312–324, Apr. 2009.

[5] W. Cui *et al.*, “Design of wideband implantable antenna for wireless capsule endoscope system,” in *IEEE Antennas Wireless Propag. Lett.*, vol. 18, no. 12, pp. 2706–2711, Dec. 2019.

[6] D. Nikolayev, M. Zhadobov, L. L. Coq, P. Karban, and R. Sauleau, “Robust ultraminiature capsule antenna for ingestible and implantable applications,” in *IEEE Trans. Antennas Propag.*, vol. 65, no. 11, pp. 6107–6119, Nov. 2017.

[7] J. Faerber *et al.*, “In vivo characterization of a wireless telemetry module for a capsule endoscopy system utilizing a conformal antenna,” in *IEEE Trans. Biomed. Circuits Syst.*, vol. 12, no. 1, pp. 95–105, Feb. 2017.

[8] J. Wang, M. Leach, E. G. Lim, Z. Wang, R. Pei, and Y. Huang, “An implantable and conformal antenna for wireless capsule endoscopy,” in *IEEE Antennas Wireless Propag. Lett.*, vol. 17, no. 7, pp. 1153–1157, Jul. 2018.

[9] R. Alrawashdeh, Y. Huang, P. Cao, and E. Lim, “A new small conformal antenna for capsule endoscopy,” in *Proc. 7th Eur. Conf. Antennas Propag. (EuCAP)*, Gothenburg, Sweden, pp. 220–223, Apr. 2013.

[10] S. Yun, K. Kim, and S. Nam, “Outer-wall loop antenna for ultrawideband capsule endoscope system,” in *IEEE Antennas Wireless Propag. Lett.*, vol. 9, pp. 1135–1138, Nov. 2010.

[11] Md. S. Miah, A. N. Khan, C. Icheln, K. Haneda, and K. Takizawa, “Antenna system design for improved wireless capsule endoscope links at 433 MHz,” in *IEEE Trans. Antennas Propag.*, vol. 67, no. 4, pp. 2687–2699, Apr. 2019.

[12] W. A. Qureshi, “Current and future applications of the capsule camera,” in *Nature Rev. Drug Discovery*, vol. 3, pp. 447–450, May 2004.

[13] W. Lei, H. Chu, and Y.-X. Guo, “Design of a circularly polarized ground radiation antenna for biomedical applications,” in *IEEE Trans. Antennas Propag.*, vol. 64, no. 6, pp. 2535–2540, Jun. 2016.

[14] K. Asimina, and S. N. Konstantina, “A review of implantable patch antennas for biomedical telemetry: challenges and solutions,” in *IEEE Antennas and Propagation Magazine*, vol. 54, no. 3, pp. 210-228, 2012.

[15] A. Sondas, and M. Ucar, “An implantable microstrip antenna design for biomedical telemetry,” in *International Conference on Electronics, Computer and Computation (ICECCO) 2013*, pp. 1595-1598, 2013.

[16] C. L. Yang, C. L. Tsai, and S. H. Chen, “Implantable high-gain dental antennas for minimally invasive biomedical devices,” in *IEEE Trans. Antennas Propag.*, vol. 61, no. 5, pp. 2380–2387, May. 2013.

[17] H. Li, Y. X. Guo, C. Liu, S. Xiao, and L. Li, “A miniature-implantable antenna for Medradio-band biomedical telemetry,” in *IEEE Antennas Wireless Propag. Lett.*, vol. 14, pp. 1176–1179, Jan. 2015.

[18] X. Cheng, D. E. C. Kim, and Y. Yoon, “A compact omnidirectional self-packaged patch antenna with complementary split-ring resonator loading for wireless endoscope applications,” in *IEEE Antennas Wireless Propag. Lett.*, vol. 10, pp. 1532–1535, 2011.

[19] J. D. Baena *et al.*, “Equivalent-circuit models for split-ring resonators and complementary split-ring resonators coupled to planar transmission lines,” in *IEEE Trans. Microw. Theory Techn.*, vol. 53, no. 4, pp. 1451–1461, Apr. 2005.

[20] S. Ma, L. Sydanheimo, L. Ukkonen and T. Bjorninen, "Split-ring resonator antenna system with cortical implant and head-worn parts for effective far-field implant communications," in *IEEE Antennas Wireless Propag. Lett.*, vol. 17, no. 4, pp. 710-713, April 2018.

[21] C. Gabriel, "Compilation of the dielectric properties of body tissues at RF and microwave frequencies," Brooks Air Force Base, San Antonio, TX, USA, Tech. Rep. AL/OE-TR-1996-0037, 1996.

[22] R. S. Alrawashdeh, Y. Huang, and P. Cao, "Flexible meandered loop antenna for implants in MedRadio and ISM bands," in *Electron. Lett.*, vol. 49, no. 24, pp. 1515–1517, Dec. 2013.

[23] Z. Duan and L. Xu, "Dual-ban implantable antenna with circular polarization property for ingestible capsule application," in *Electron. Lett.*, vol. 53, no. 16, pp. 1090–1092, Aug. 2017.

[24] F. Merli, B. Fuchs, J. R. Rosig, A. K. Skrivervik, "The effect of insulating layers on the performance of implanted antennas," in *IEEE Trans. Antennas Propag.*, vol. 59, no. 1, pp. 21-31, Jan. 2011.

[25] A. Kiourti and K. Nikita, "Miniature scalp-implantable antennas for telemetry in the MICS and ISM bands: Design, safety considerations and link budget Analysis," in *IEEE Trans. Antennas Propagat.*, vol. 60, no. 8, pp. 3568-3575, Aug. 2012.

[26] F. Merli, "Implantable antennas for biomedical applications," Ph.D. dissertation, Department of Electrical Engineering, EPFL Univ., Lausanne, Switzerland, 2011.

[27] IEEE Standard for Safety Levels with respect to Human Exposure to Radio Frequency Electromagnetic Fields, 3KHz to 300 GHz, IEEE Standard C95. 1-1999, 1999.

[28] R. Moore, "Effects of a surrounding conducting medium on antenna analysis," in *IEEE Trans. Antennas Propag.*, vol. 11, no. 3, pp. 216–225, May 1963.

[29] T. Yilmaz, T. Karacolak, and E. Topsakal, "Characterization and testing of a skin mimicking material for implantable antennas operation at ISM band (2.4 GHz–2.48 GHz)," in *IEEE Antennas Wireless Propag. Lett.*, vol. 7, pp. 418-420, 2008.

[30] X. Liu, Z. Wu, Y. Fan and E. M. Tentzeris, “A miniaturized CSRR loaded wide-beamwidth circularly polarized implantable antenna for subcutaneous real-time glucose monitoring,” in *IEEE Antennas Wireless Propag. Lett.*, vol. 16, pp. 577-580, 2017.

[31] C. J. Sa´nchez-Ferna´ndez *et al.*, “Dual- band implantable antenna based on short-circuited SRR” in *Proc. EuCAP2010*, Barcelona, Spain, pp.1-4, 2010.

[32] S. M. Asif *et al.*, “Design and in vivo test of a battery-less and fully wireless implantable asynchronous pacing system,” in *IEEE Trans. Biomedl Eng.*, vol. 63, pp. 1070–1081, Sept. 2016.

[33] R. Li, Y. X. Guo and G. Du, “A conformal circularly polarized antenna for wireless capsule endoscope systems,” in *IEEE Trans. Antennas Propag.*, vol. 66, no. 4, pp. 2119–2124, April. 2018.

[34] R.Das and H. Yoo, “A wideband circularly polarized conformal endoscopic antenna system for high-speed data transfer,” in *IEEE Trans. Antennas Propag.*, vol. 65, no. 6, pp. 2816–2826, Jun. 2017.

[35] Z. Duan *et al.*, “Integrated design of wideband omnidirectional antenna and electronic components for wireless capsule endoscopy systems,” in *IEEE Access*, vol. 6, pp. 29626–29636, May 2018.

[36] W. Lei and Y. X. Guo, “Design of a dual-polarized wideband conformal loop antenna for capsule endoscopy systems,” in *IEEE Trans. Antennas Propag.*, vol. 66, no. 11, pp. 5706–5715, Nov. 2018.

[37] P. M. Izdebski, H. Rajagopalan, and Y. Rahmat-Samii, ‘‘Conformal ingestible capsule antenna: A novel chandelier meandered design,’’ in *IEEE Trans. Antennas Propag.*, vol. 57, no. 4, pp. 900–909, Apr. 2009.

CHAPTER 4. A COMPACT DUAL-POLARISED ANTENNA FOR WPANS WITH INDOOR/OUTDOOR LOCALISATION

Chapter 3 presented a novel wideband implantable/ingestible antenna with desirable characteristics regarding operation bandwidth, realised gain, radiation efficiencies, and SAR for healthcare in the field of WBAN communication. To develop this theme further by considering the requirements of WPANs in which localisation of devices is often desirable, this chapter focuses on a novel wideband dual-polarised antenna for medical telemetry and indoor/outdoor localisation. This antenna operates in the WMTS band (1.395 GHz~1.4 GHz) for medical services, the Global Navigation Satellite System (GNSS) L1/E1 band (1.57 GHz) and Global Positioning System (GPS) L5 band (1.17 GHz) for outdoor localisation, and an ISM band (2.45 GHz) for indoor localisation.

To ensure a reliable communication link, the antenna is designed with an operational bandwidth for S_{11} <-10 dB from 1.15 GHz to 2.62 GHz, which is wide in comparison to other published works as will be detailed later. This helps to avoid system failure due to frequency detuning of the antenna as a result of manufacturing tolerances and variable operating environments. The electrical length of the antenna is $0.25\lambda_0 \times 0.25\lambda_0 \times 0.006\lambda_0$ on FR4 printed circuit board (PCB). Meanwhile, a vacant-quarter printed ring structure is employed as a 90° phase delay line to realise circular polarisation (CP). The measured axial ratio (AR) bandwidths (AR < 3 dB) for the manufactured antenna are from 1.05 GHz to 1.23 GHz (6.84%), from 1.42 GHz to 1.78 GHz (19.11%), and from 2.29 GHz to 2.47 GHz (11.25%). Simulated and experimental outcomes are in good agreement, which illustrates this design operates with LP radiation at 1.4 GHz for wireless medical telemetry, and CP radiation over 1.17, 1.57, and 2.4 GHz for indoor and outdoor localisation. Therefore, this antenna is capable of continuous and integrated communication and tracking for WBAN/WPAN applications.

4.1 Introduction

WPAN represents a type of dynamic personal network which enables people to interconnect any devices located within their direct vicinity and communicate or transfer data amongst them with aid of wireless communication technologies [1]-[5]. It is considered to cover a range of approximately 10 m around the user, extending the communication link from around 2 m for WBAN [2]. One typical application is the remote health monitoring WPAN, which aims at monitoring and collecting vital bio-information from the human body whilst simultaneously tracking its location. The GNSS, which provides people with both autonomous geo-spatial positioning and time information of a user's location [6], [7], is accessible for positioning applications. GNSS-enabled systems typically transmit and receive CP waves to avoid sensitivity to the influence of Faraday rotation as mentioned in Chapter 1. Considering the feed configuration of a CP antenna, the single feed configuration is preferable and suitable as it eliminates the need for additional power dividers, which are commonly used in the dual-feed structure [8], [9]. Hence, the antenna for WPAN applications discussed in this chapter is equipped with dual-polarised characteristics and powered by a single feed structure.

The general solution to achieving CP behaviour is to generate two orthogonal current paths with the same amplitude but 90° phase difference flowing on the antenna. A popular antenna structure utilised to obtain a CP characteristic is the patch. This is commonly achieved by truncating the patch corners or adding slits aligned in the diagonal directions [10]-[15]. Despite easy completion, a common problem identified with this configuration in published work is the relatively narrow fractional impedance bandwidth. Furthermore, a practical antenna with GPS capability should meet the operational requirement, that is, the 3 dB AR beamwidth (ARBW) is required to be no less than 120° [6]. Wide 3 dB ARBW ensures the stability of communication and good positioning accuracy. In some recent publications [13]-[15], the 3 dB ARBW is not mentioned, and antennas in these papers operate with 1%, 1.4% and 1.84% equivalent

fractional bandwidth at 1575 MHz, 1575 MHz, and 1760 MHz, respectively. Consequently, these antennas require a high fabrication precision and could suffer from mismatch due to frequency shifting. In addition to these requirements, an antenna for WPAN should be compact to meet the needs of typical device's, hence consideration must be made towards antenna size miniaturisation.

Contemplating the aforementioned aspects, the target of this chapter is to design a compact LP/CP antenna, which covers the WMTS band (1400 MHz) for wireless medical telemetry and GNSS L1/E1 band (1575 MHz), GPS L5 band (1176 MHz), and 2.45 GHz ISM band for indoor and outdoor localisation. Instead of adopting a patch structure, a dual cross dipole is selected as the starting point. A novel single feed topology is utilised with an annular ring to achieve the desired CP behaviour and reduce antenna size. Furthermore, the CP bandwidth of the proposed design should be relatively wide enabling coverage of the operating bands of interest discussed above.

The structure of this chapter is as follows: firstly Section 4.2 begins with a description of why the crossed dipole is selected for the initial study and how a multi-loop structure is achieved. This section also offers a discussion of design configuration and operating mechanism, including detailed parametric analysis and CP behaviour. Section 4.3 then provides both simulation and measurement outcomes. Comparisons with other works are also made in this section. Finally, concluding remarks are provided in Section 4.5.

4.2 Design Configuration and Working Mechanism

An elliptical-shaped cross dipole structure has been studied as the starting point of this work because of its wide operating bandwidth. As is depicted in Fig. 4-1(a), two pairs of elliptical cross dipoles that are orthogonal to each other are printed on both sides of the substrate. A novel feeding network as proposed in [16] is adopted to generate a 90° phase delay at specific design frequencies and therefore offer CP radiation behaviour. The overall board dimension is 64 × 64 × 1.57 mm^3. The simulated S_{11} of this reference antenna is given in Fig. 4-2. The resonant frequency is at 1.14 GHz and the bandwidth

of this antenna for S_{11} <-10 dB is from 1.08 GHz to 1.23 GHz (150 MHz) and from 1.79 GHz to 2.68 GHz (890 MHz). With the intention of covering the GNSS L1/E1 band (1.57 GHz) and improving the matching performance at higher frequencies (up to 2.4 GHz), the radiators of the reference antenna are modified to a multi-loop structure, which is shown in Fig. 4-1(b). The related S_{11} results in Fig. 4-2 demonstrate that the proposed multi-loop dipole antenna resonates at 1.17 GHz, 1.57 GHz, 2.1 GHz, and 2.4 GHz with a wide bandwidth from 1.07 GHz to 2.61 GHz (1540 MHz), achieving the initial goal of band coverage. The detailed design process and evaluation are provided in the following sub-sections.

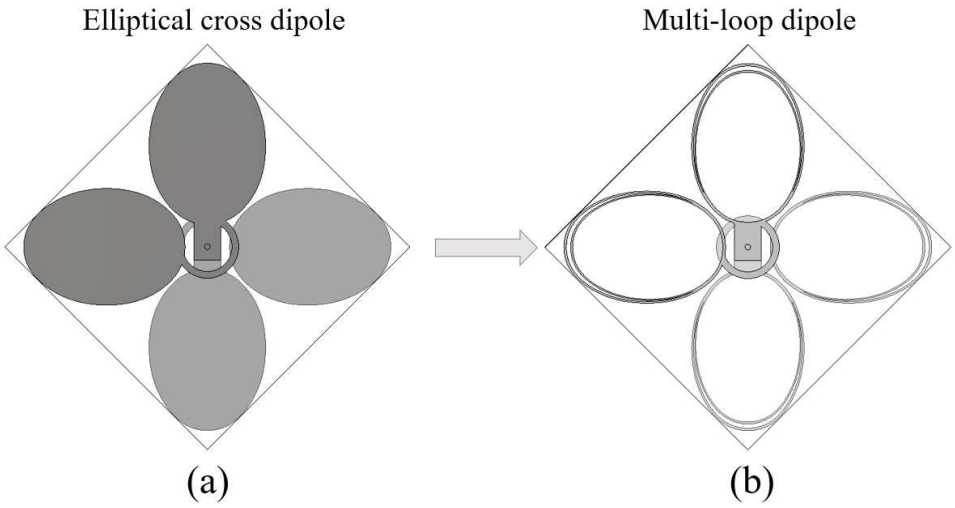

Fig. 4-1: Evolution of the proposed structure: from (a) an elliptical cross dipole to (b) a modified multi-loop dipole.

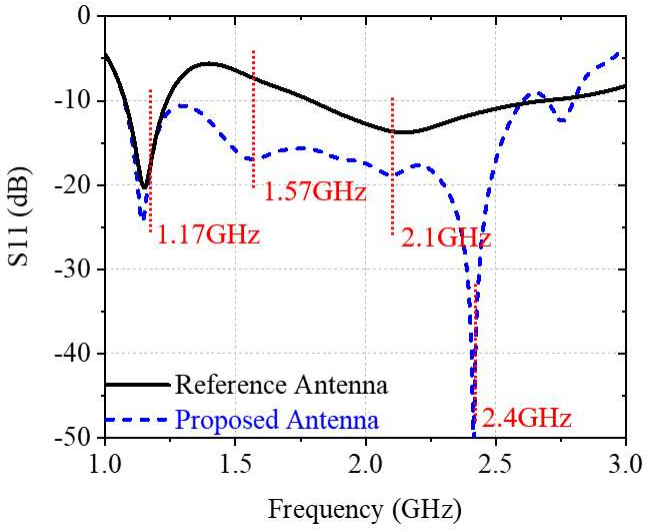

Fig. 4-2: Simulated S_{11} of the reference antenna and the proposed antenna.

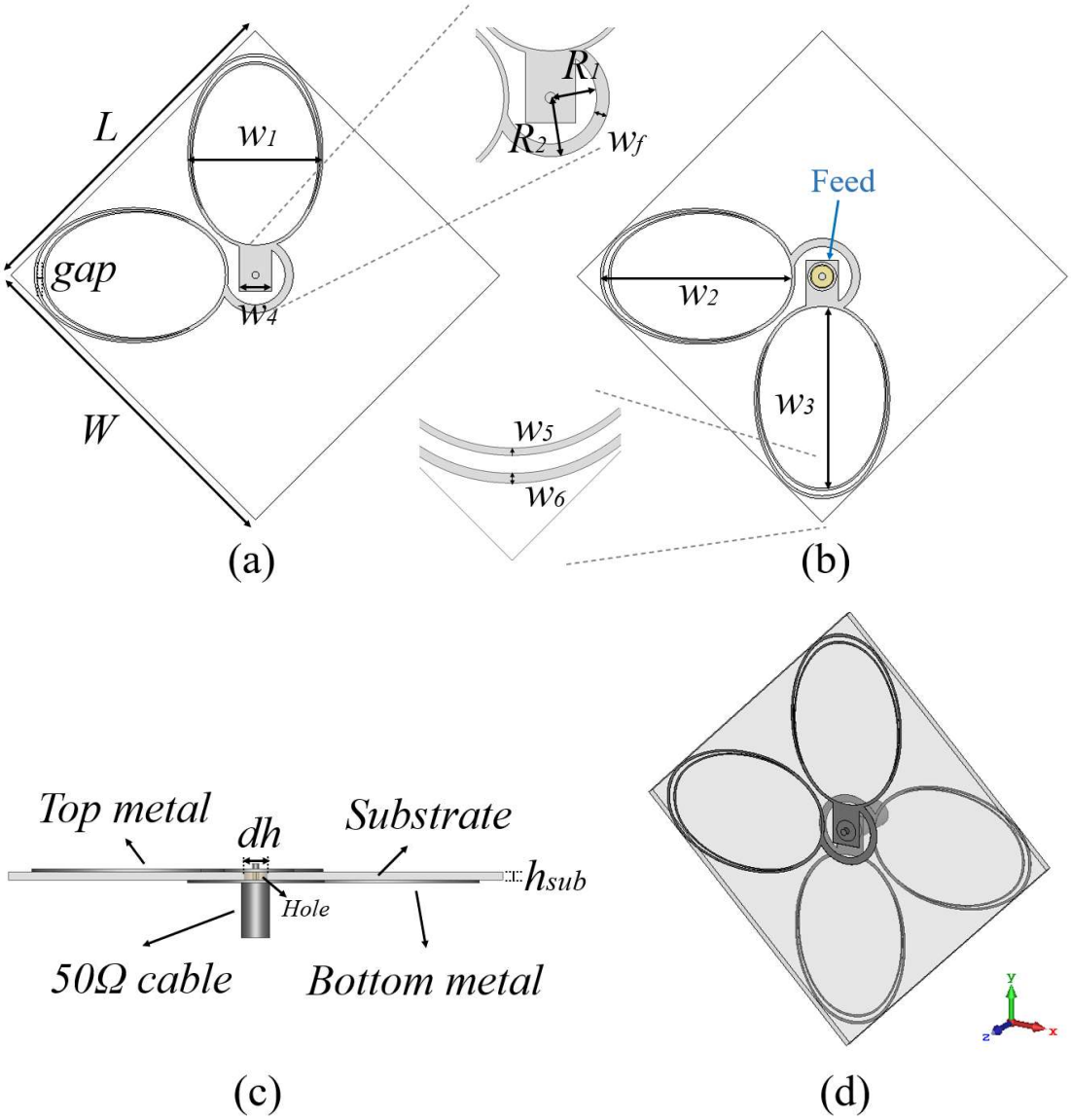

Fig. 4-3: Geometry of the proposed antenna: (a) top view with feeding structure; (b) bottom view; (c) side view; (d) 3-D view.

4.2.1 Antenna Design

The configuration of the proposed antenna is depicted in Fig. 4-3 shown in top view, bottom view, side view, and 3-D view. It is printed on both sides of an FR-4 substrate with relative permittivity $\varepsilon_r = 4.3$ and thickness of 1.5 mm. A standard 50 Ω coaxial connector is used to feed the structure, with the core (inner conductor) extended through the substrate and connected to the top feeding line. The outer conductor of the connector is connected to the bottom feeding line. A vacant-quarter printed ring is employed as a

90° phase delay line to produce a dual CP behaviour, that is, the right-hand CP (RHCP) radiation from the top side and the left-hand CP (LHCP) from the bottom side of the antenna. The overall dimension is 64 × 64 × 1.57 mm^3 with a corresponding electrical length of $0.25\lambda_0 \times 0.25\lambda_0 \times 0.006\lambda_0$ where the free space wavelength is λ_0 = 256 mm at the lowest resonant frequency f_L = 1.17 GHz (GPS L5 band). Table 4-1 summarises the optimised geometrical parameters of this antenna after conducting parametric studies using CST 2017.

Table 4-1: Optimised Dimensions of the Proposed Antenna (Millimetre)

Parameter	**Value**	**Parameter**	**Value**
L	64.00	w_f	1.50
W	64.00	w_1	25.00
R_1	5.50	w_2	35.40
R_2	7.00	w_3	33.50
h_{sub}	1.50	w_4	5.60
dh	4.20	w_5	0.38
gap	0.98	w_6	0.54

4.2.2 Parametric Analysis

The influence of the key parameters including w_1, w_2, w_3, w_6, and gap, on S_{11}, is examined, and the corresponding results are demonstrated in the following. Fig. 4-4 shows the relationship between S_{11} and w_1. Overall, a wider bandwidth is obtained as

the width w_1 is independently increased. The impedance bandwidth increases from 910 MHz to 1126 MHz, 1561 MHz, and 1530 MHz as the value of w_1 increases from 17 mm to 21 mm, 23 mm, and 25 mm, respectively. Despite the slightly smaller bandwidth when w_1 is 25 mm compared with 23 mm, the matching performance at the desired frequency of 2.45 GHz is much better, which can be seen from the results of S_{11} (from -16.2 dB to -53.3 dB). When w_1 reaches 27 mm, the radiators on the same side will be connected and the resonant frequency at 2.45 GHz is affected severely. As a trade-off, w_1 = 25 mm is selected as the optimal value.

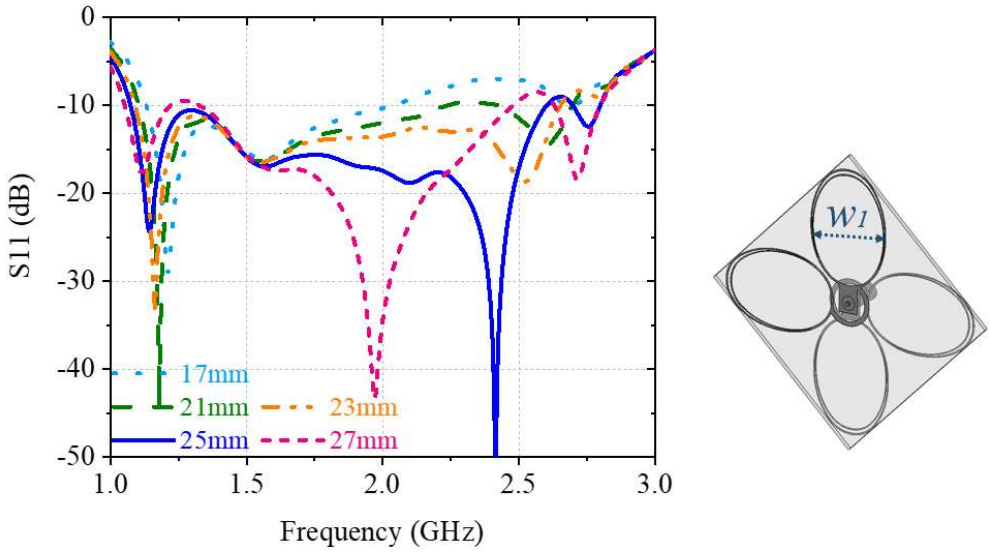

Fig. 4-4: Effects on S_{11} with different values of w_1.

The values of w_2 and w_3 have also been evaluated and the corresponding results can be seen in Fig. 4-5. The first resonant frequency mainly depends on w_2 and the fourth resonant frequency is mainly dependent on w_3. The lowest resonant frequency shifts down as the value of w_2 increases. Similarly, the resonant frequency at 2.4 GHz also decreases as w_3 increases. By carefully selecting the values of w_2 and w_3, the desired resonant frequencies 1.17 GHz and 2.4 GHz can be covered, and the corresponding optimised results are w_2 = 35.4 mm, and w_3 = 33.5 mm.

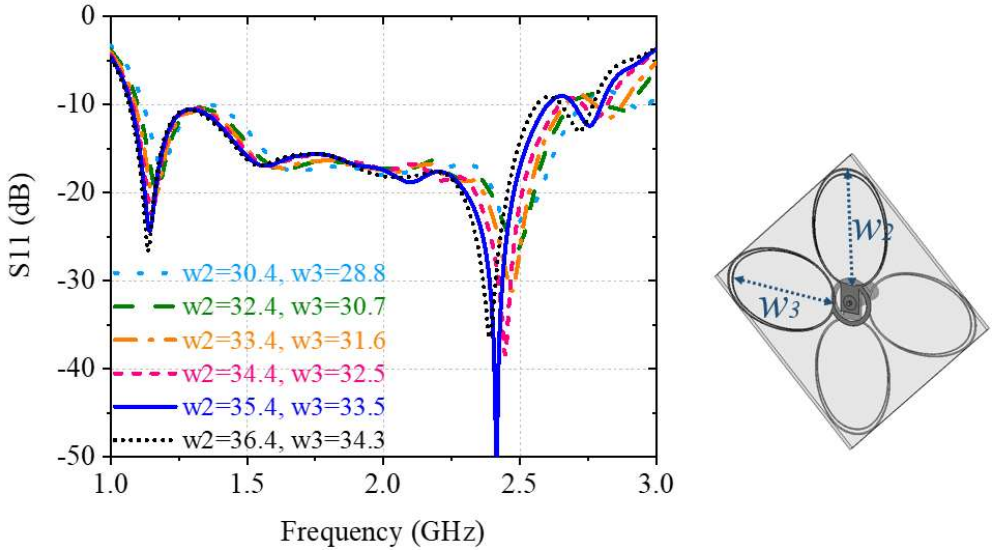

Fig. 4-5: Effects on S_{11} with different values of w_2 and w_3.

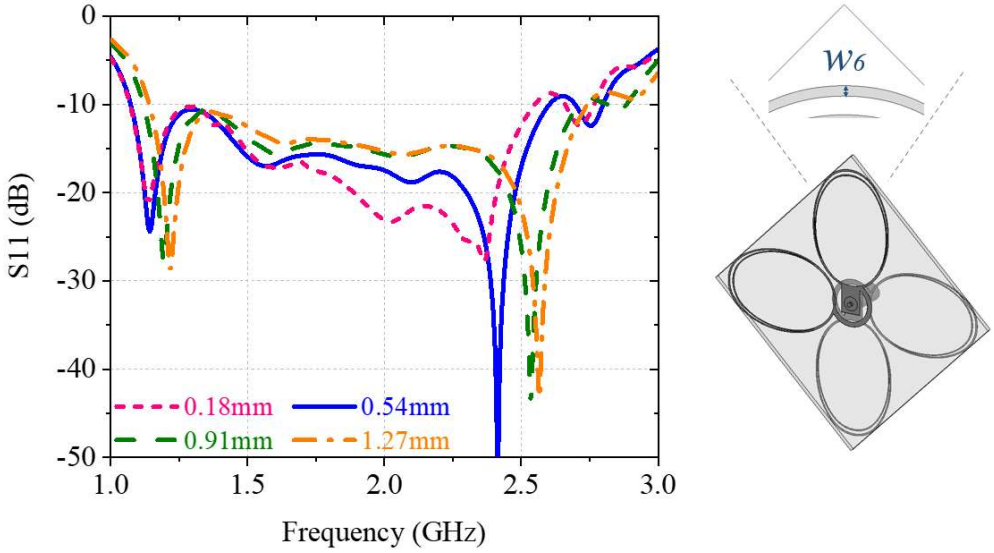

Fig. 4-6: Effects on S_{11} with different values of w_6.

The effect on S_{11} of varying w_6 is demonstrated in Fig. 4-6. The operation bandwidth is 1477.4 MHz when w_6 is 0.18 mm. The bandwidths increase by 62.6 MHz, 117.8 MHz, and 122.2 MHz as w_6 varies through to 0.54 mm, 0.91 mm, and 1.27 mm, respectively. This phenomenon indicates that the operating bandwidth becomes wider as the track width of the big loop w_6 increases. Moreover, better impedance matching can be achieved by tuning the value of w_6. The S_{11} results at the first desired resonant frequency (1.17 GHz) are -20.54 dB, -24.21 dB, -13.69 dB, and -10.50 dB when w_6 is varied through 0.18 mm, 0.54 mm, 0.91 mm, and 1.27 mm, respectively. Meanwhile, S_{11} at

the fourth desired resonant frequency (2.4 GHz) in each case is -19.70 dB, -53.33 dB, -17.50 dB, and -16.53 dB, respectively. Therefore, the most suitable value of w_6 is 0.54 mm, where both resonant frequencies are minimised.

Finally, the *gap* between the two loop structures is evaluated in terms of S_{11}. As is shown in Fig. 4-7, the fourth resonant frequency (2.4 GHz) is affected prominently by the *gap*. It shifts upwards from 2.34 GHz to 2.48 GHz with increasing values of *gap*. The results of S_{11} at 2.4 GHz are -38.27 dB, -53.33 dB, -28.24 dB, and -19.77 dB when *gap* is varied through 0.71 mm, 0.98 mm, 1.23 mm, and 1.48 mm, respectively. On the other hand, the first resonant frequency (1.17 GHz) appears independent of the *gap*. Following careful tunning, the optimised result for *gap* is set to 0.98 mm.

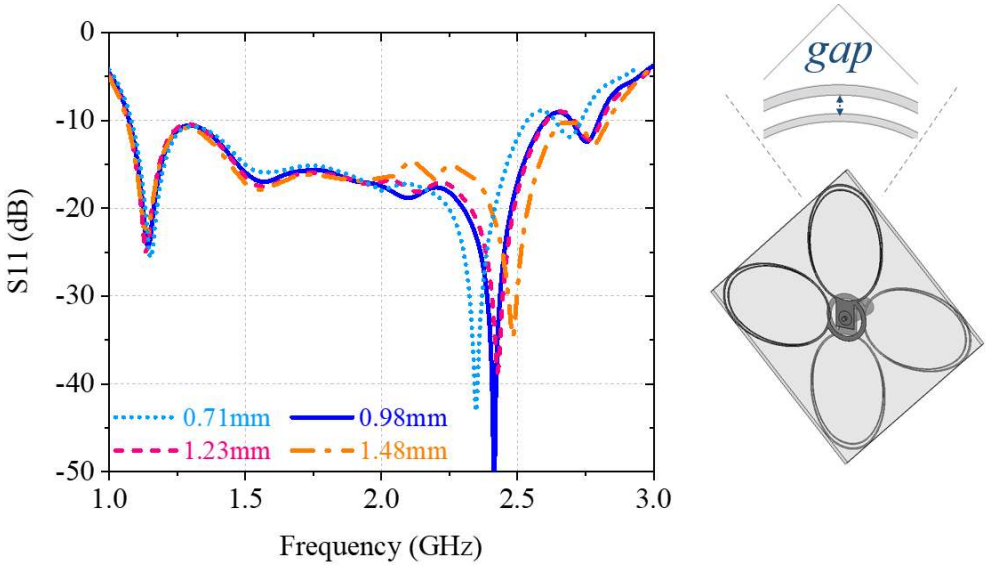

Fig. 4-7: Effects on S_{11} with different values of *gap*.

4.2.3 Circular Polarisation Mechanism

Circular polarisation behaviour is achieved in three frequency bands through the use of the vacant-quarter printed ring structure as depicted in Fig. 4-3. The incoming current from the feed flows into the connected radiator first and then travels through the vacant-quarter printed ring and reaches the secondary radiator. The 90° phase delay between the radiators is controlled by the length of the vacant-quarter printed ring structure. The surface current distribution at f = 1.57 GHz for the GNSS L1/E1 band is selected as an

example to show the CP mechanism. Fig. 4-9 demonstrates the phase progression at quarter wavelength time instants for the proposed antenna. Looking at the structure from the front, the magnitudes of the current distribution at 0° are equal to those at 180°, but the phases are opposite. A similar phenomenon is observed for the current distributions at 90° and 270°. The overall rotation of the current distribution looking from the front is anti-clockwise, hence, achieving RHCP behaviour.

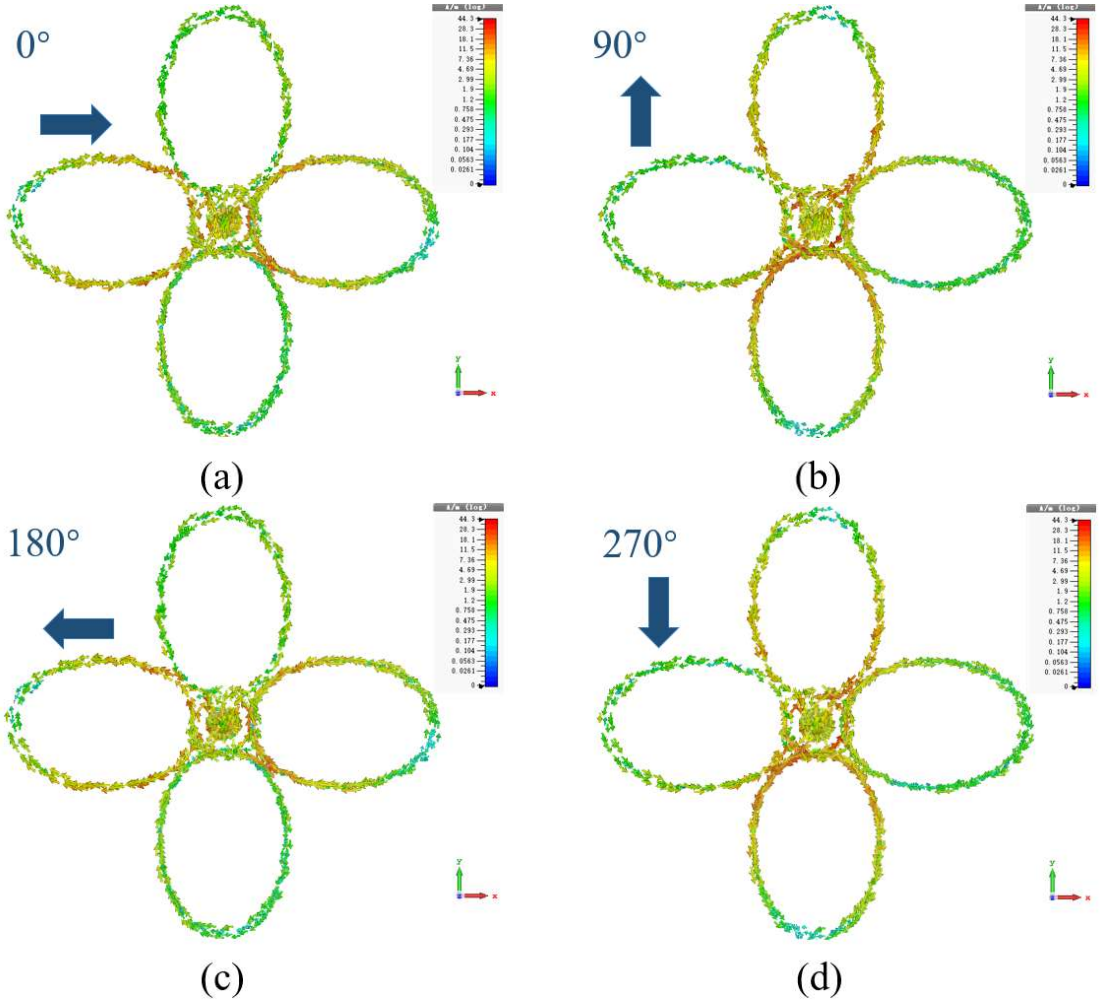

Fig. 4-8: Surface current distribution on the top side of the proposed antenna at 1.57 GHz at (a) 0°, (b) 90°, (c) 180°, and (d) 270°.

Looking at the whole structure from the back, the rotation of the current distribution is clockwise as is depicted in Fig. 4-9. Similar observations that the magnitudes of the current distribution at 0° and 90° are equal to those at 180° and 270°, respectively, and the phases at 0° and 90° are opposite to those at 180° and 270°, respectively. Therefore, it achieves LHCP behaviour from the back.

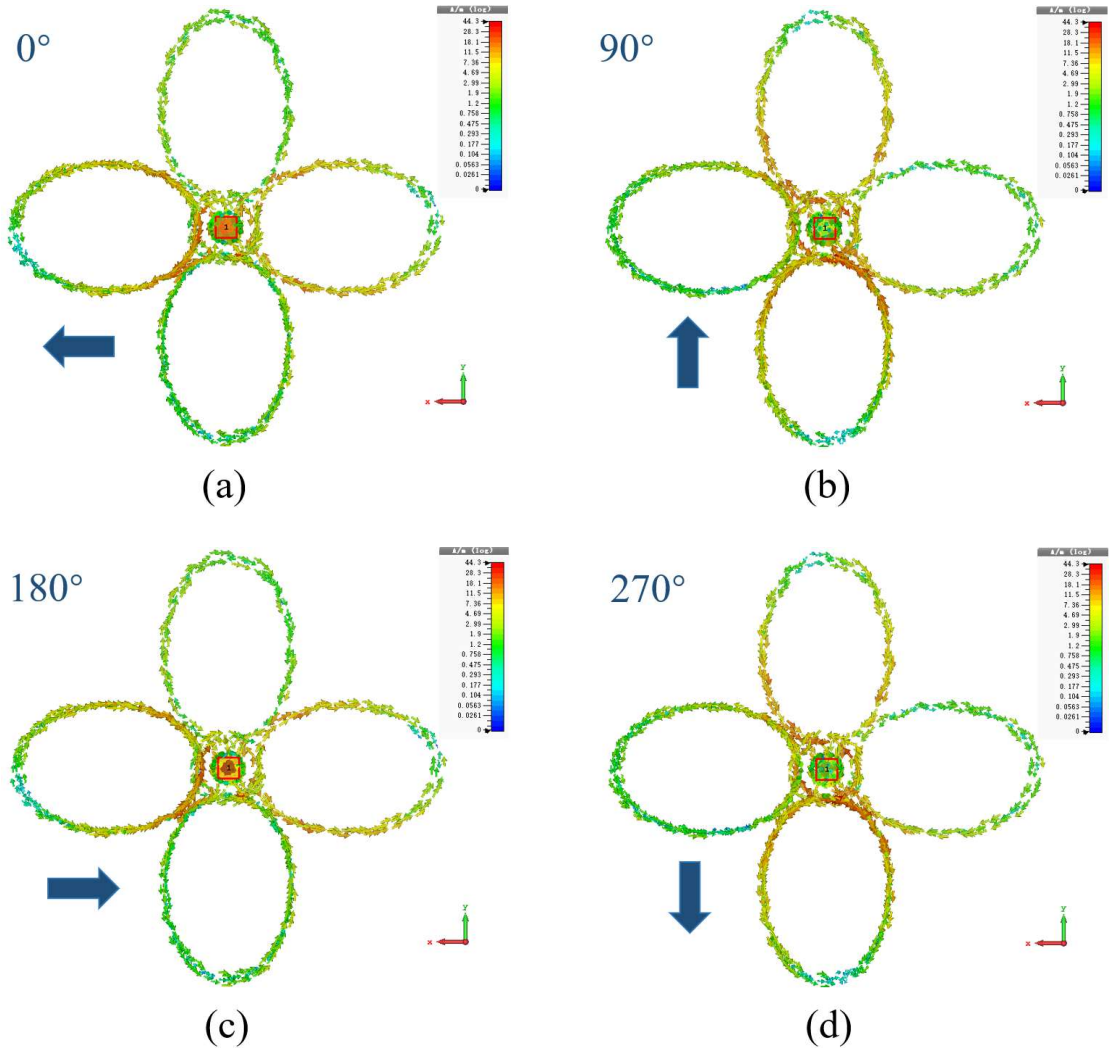

Fig. 4-9: Surface current distribution on the bottom side of the proposed antenna at 1.57 GHz at (a) 0°, (b) 90°, (c) 180°, and (d) 270°.

In addition to observing the surface current, another parameter used to evaluate the CP characteristic is AR, which is the ratio of the major to minor axes (magnitudes of orthogonal components) of the antenna's E-field. Ideally, it equals to 0 dB for a perfect CP antenna. Practically, an antenna with an AR of less than 3 dB can be treated as a CP antenna. The simulated AR values at 1.57 GHz are evaluated on its two principal planes of phi = 0° and phi = 90°, respectively, and the corresponding results are depicted in Fig. 4-11. At boresight (theta = 0°), AR equals to 2.367 dB, which is less than 3 dB. Overall, the AR is less than 3dB for theta = ±60° and theta = ±66° from the main beam on the phi = 0° and phi = 90° planes, respectively. As a result, the realised 3 dB AR beamwidth is 120° at 1570 MHz, which meets the required AR beamwidth for GPS

usage. Therefore, this antenna has a sufficiently good CP behaviour for GPS applications.

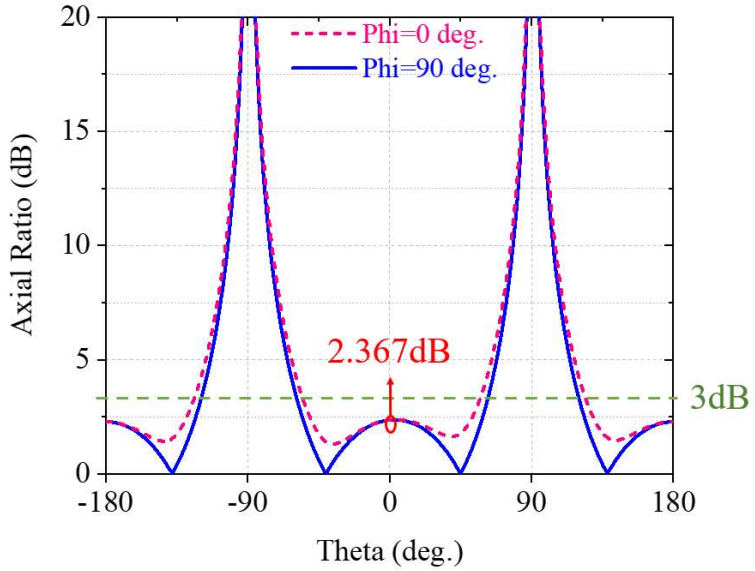

Fig. 4-10: Performance of simulated AR at 1570 MHz.

4.3 Realisation and Measurements

The proposed structure was fabricated on a 1.5 mm thick FR-4 board with an overall dimension of 64 × 64 × 1.57 mm^3 using an etching process. The bottom and top views are depicted in Fig. 4-12. Its performance is validated and evaluated in terms of its return loss, radiation patterns, realised gains, AR, and radiation efficiency in this section.

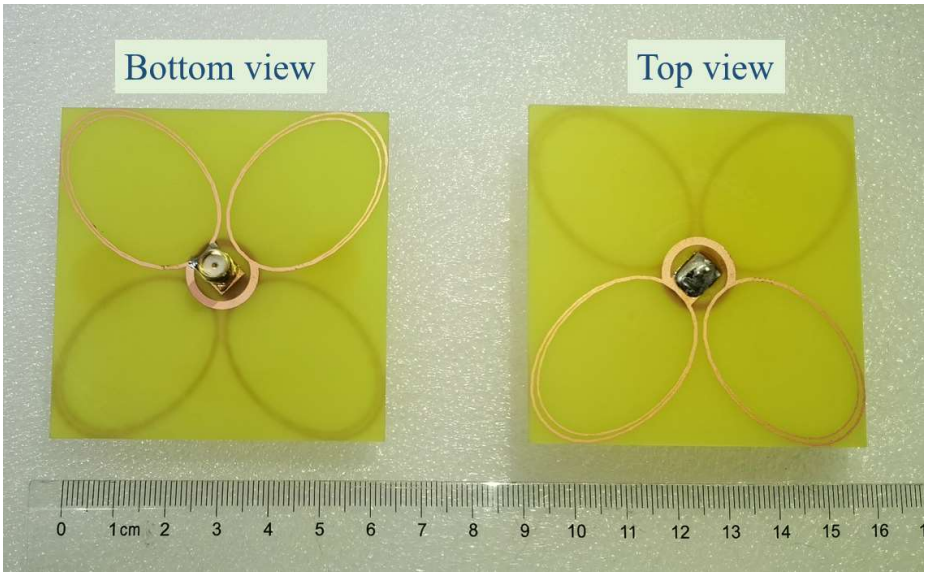

Fig. 4-11: Bottom and top views of the manufactured prototypes.

4.3.1 Evaluation of Return Loss

The reflection coefficient (S_{11}) of the proposed antenna was measured using a portable VNA (model N9917A FieldFox Microwave Analyser from Keysight) calibrated with a standard 50 Ω RF cable. The measurement setup is provided in Fig.4-12 and the corresponding impedance matching response is plotted in Fig. 4-13.

Fig. 4-12: S_{11} measurement setup of the proposed antenna.

Overall, the operating bandwidth for S_{11} <-10 dB is from 1.15 GHz to 2.62 GHz (1470 MHz), which covers all desired frequency bands with a slight reduction of 70 MHz compared with the simulated results. The impedance matching remains well below -15 dB from 1.39 GHz to 1.74 GHz and from 2.18 GHz to 2.54 GHz, which covers most of the desired frequencies (1.57 GHz and 2.4 GHz). The lower resonance shifts up from 1.17 GHz to 1.27 GHz whilst the higher one at 2.4 GHz remains stable. Despite the upward shifts in the lower resonant frequencies, the matching performance at 1.40 GHz and 1.57 GHz improve in comparison to the simulation as the S_{11} measurements are -15.24 dB and -22.65 dB, deepened by 2.82 dB and 5.68 dB. Probable reasons for these differences are fabrication errors and connectivity issues.

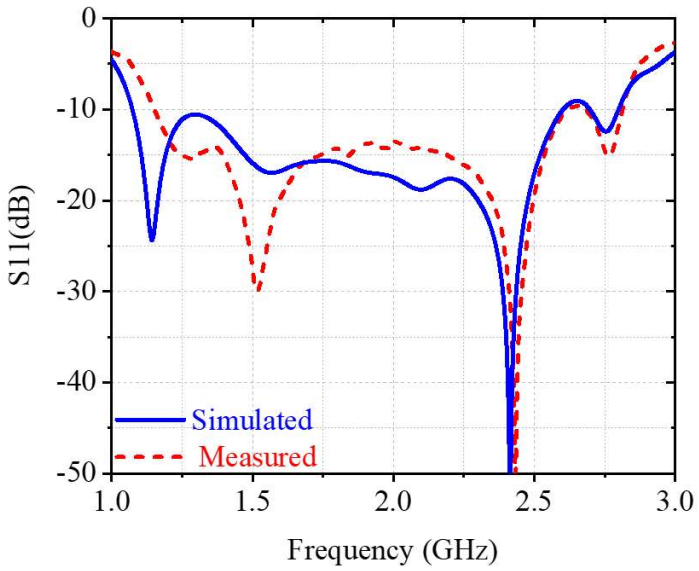

Fig. 4-13: Simulated and measured S_{11} of the proposed design.

4.3.2 Evaluation of CP Characteristic

Due to equipment limitations, the CP purity of the proposed antenna has been evaluated by comparing the far-field coupling strength for two orthogonal polarisations between the antenna under test (AUT) at 0° and 90° and a standard gain LP pyramidal horn antenna in an anechoic environment [17]. When the magnitudes of S_{21} for the two polarisations are equal or the difference between them is less than 3 dB, then it indicates that the AUT behaves with CP. The corresponding measurement setup is depicted in Fig. 4-14 (a) and the positions of AUT can be seen in Fig. 4-14 (b) and Fig. 4-14 (c). Reflection coefficients are recorded by an Agilent PNA-L network analyser (N5230C) and analysed with aid of a PC.

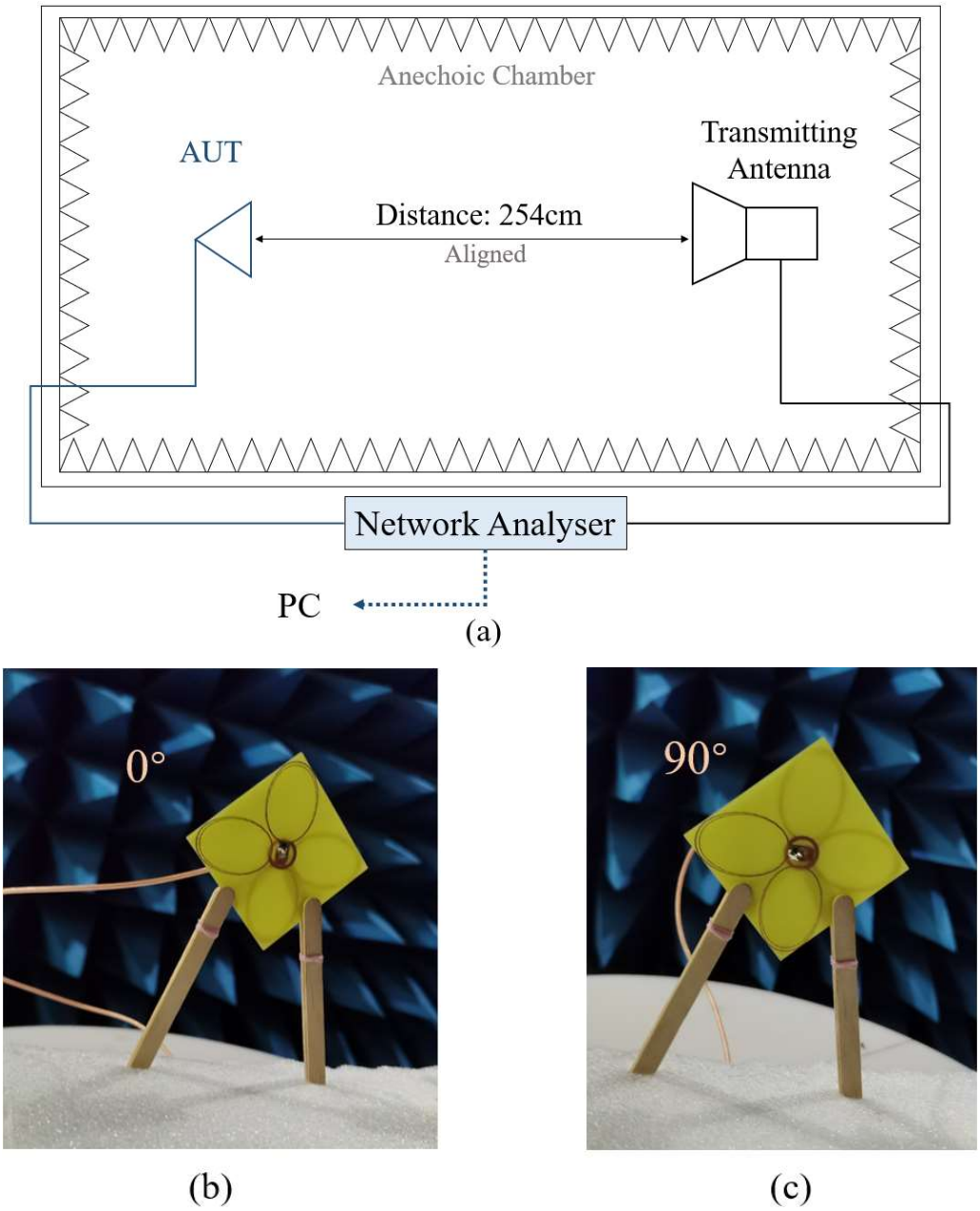

Fig. 4-14: (a) Schematic of the measurement setup; (b) AUT placed at 0°; and (c) AUT placed at 90°.

The measured coupling strengths ($|S_{21}|$) for the orthogonal polarisations and their difference are plotted in Fig. 4-15. Relatively good polarisation purity is achieved at around 1.13 GHz, 1.46 GHz, and 2.38 GHz as $|S_{21}|_{0°} \approx |S_{21}|_{90°}$. Moreover, the measured 3 dB AR bandwidths are around 180 MHz (from 1.05 GHz to 1.23 GHz), 360 MHz (from 1.42 GHz to 1.78 GHz), and 180 MHz (from 2.29 GHz to 2.47 GHz) over the frequency range.

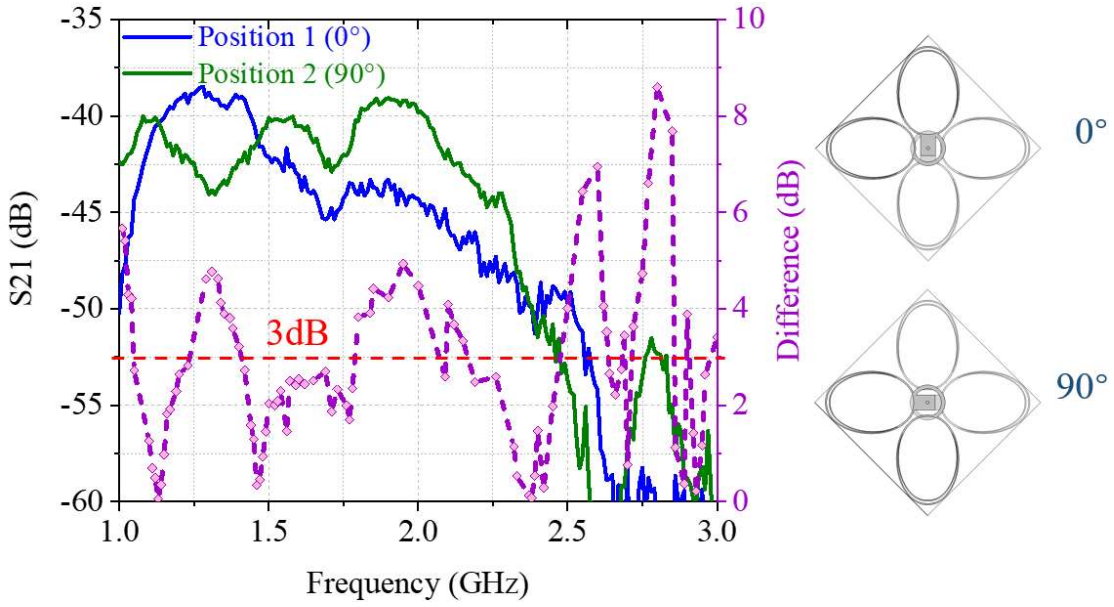

Fig. 4-15: Measured $|S_{21}|$ when placing the AUT at 0° and 90° and their differences.

Fig. 4-16 compares the simulated and measured AR characteristics. The simulated ARBWs of the proposed antenna for AR < 3 dB are 1.15~1.23 GHz, 1.45~1.75 GHz, and 2.20~2.47 GHz. Overall, the measured results show a good agreement with the simulated results. Moreover, the measured AR at the GNSS L1/E1 band (1570 MHz) is 2.506 dB, which is close to the simulated result of 2.367 dB. Therefore, the proposed antenna can be considered as having good CP performance and hence suitable for localisation applications.

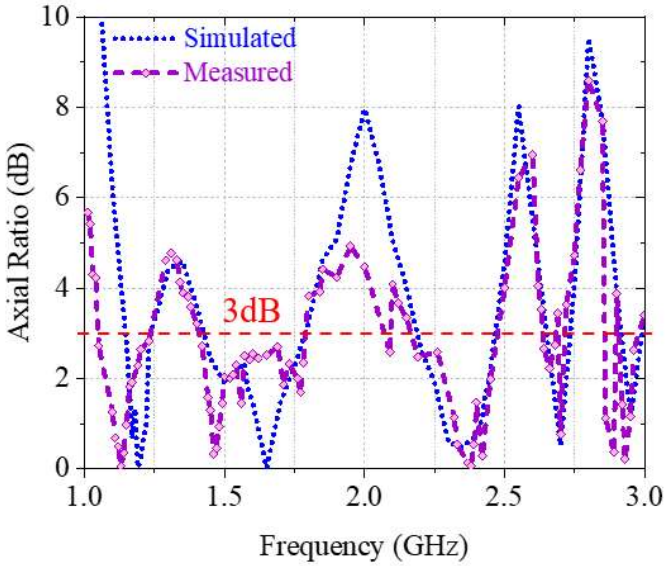

Fig. 4-16: Measured and simulated AR.

4.3.3 Evaluation of Radiation Patterns

Measurements of the far-field radiating characteristics are conducted inside an anechoic chamber. Fig. 4-17 depicts the corresponding measurement setup. A standard gain LP pyramidal horn antenna is used as the transmitter and the proposed antenna under test (AUT) is placed 254 cm away as the receiver. A rotator controlled by a PC is connected to the AUT and an Agilent PNA-L network analyser (N5230C) is used to record the *S*-parameters. To conduct the measurements across the full frequency range of interest two standard LP pyramidal horns covering different frequency ranges (1-2 GHz and 2-3 GHz) are used to measure the co-polarisation and cross-polarisation of the proposed antenna. The *S*-parameters are recorded for rotation steps of 1° allowing the radiation pattern to be plotted at the desired frequencies.

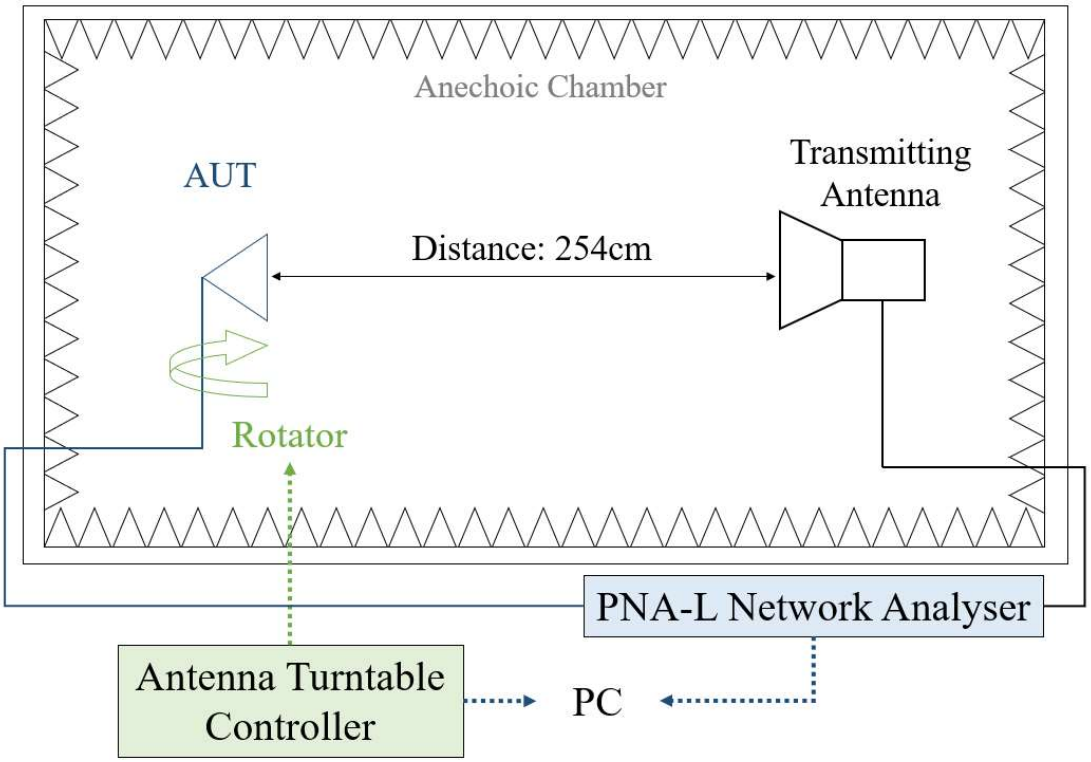

Fig. 4-17: Schematic of the measurement setup.

Four LP measurement sets have been obtained using each of the available standard gain horns in order to evaluate the CP radiation characteristics as described in Fig. 4-18. The four radiation patterns recorded are the copolar and crosspolar results on both H-plane and E-plane. Firstly, the AUT is set at P_1 with the transmitting antenna placed

horizontally to the ground (H_1) with the antennas on the boresight. The rotator rotates the AUT by 360° horizontally and the network analyser records transmission coefficients at all angles over 1 to 2 GHz. The second experiment is performed after rotating the AUT by 90° horizontally (P_2) and then repeating the same process. The third and final experiments are conducted in the same way but with the transmitting antenna placed vertically to the ground (V_1). Therefore, the recorded results are the copolar and crosspolar information on H-plane and E-plane. The entire process is repeated with the second standard gain horn over the frequency range from 2 to 3 GHz.

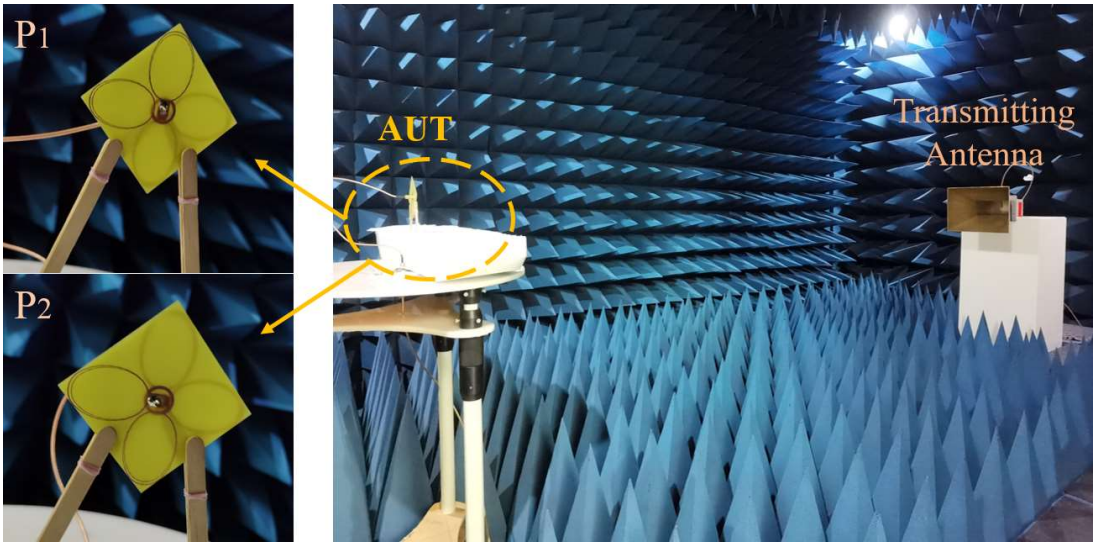

(a)

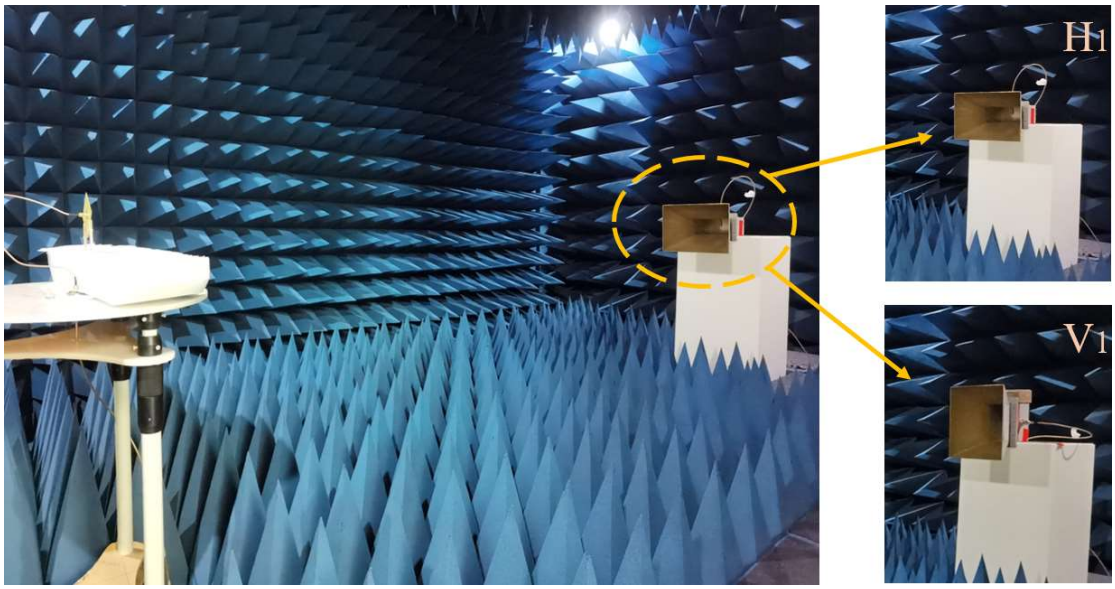

(b)

Fig. 4-18: Measurement setup in the anechoic chamber: (a) place the AUT at two positions P_1 and P_2; (b) place the transmitting horn at two positions H_1 and V_1.

Simulated copolar and crosspolar data for the H-plane (*xoz* plane) and E-plane (*yoz* plane) are exported from CST 2017 for comparison. The measured and simulated normalised radiation patterns at 1.40 GHz are depicted in Fig. 4-19 with a 3D radiation pattern for illustration. It shows that this antenna has a maximum directivity of 2.37 dBi at 1.40 GHz. The measured 2D results are close to the simulated 2D results, which verify the good agreement between simulation and measurement.

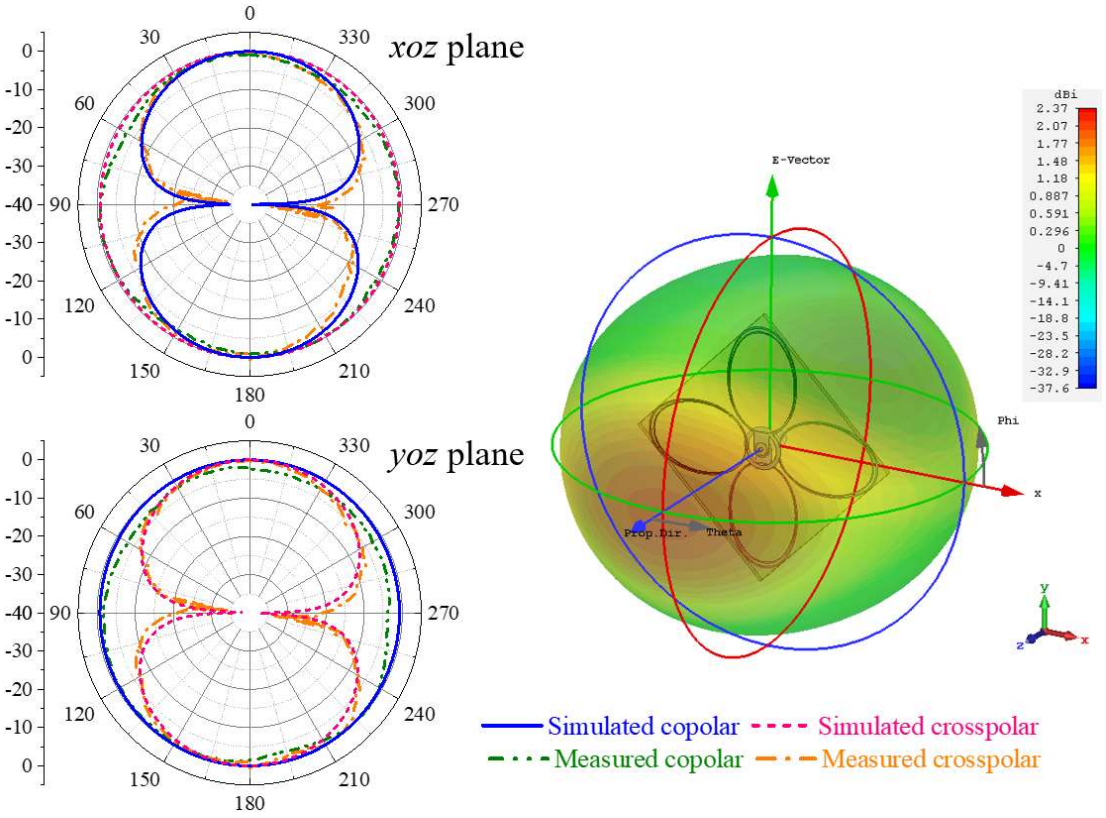

Fig. 4-19: 3D simulated radiation pattern and 2D simulated and measured radiation patterns over (a) *xoz* plane at 1.40 GHz, (b) *yoz* plane at 1.40 GHz.

The measured and simulated normalised radiation patterns at 1.17 GHz, 1.57 GHz and 2.40 GHz are depicted in Fig. 4-20. The radiation patterns at the desired frequencies are bidirectional with a relatively broad half-power beamwidth (HPBW). For example, the HPBW at 1.57 GHz is 121.5° for E-plane, and 120.5° for H-plane. The HPBW for other frequencies is summarised in Table 4-2. Overall, the measured outcomes agree well with the simulated outcomes, which confirm the theoretical evaluation. The difference between the measured and simulated results is most likely caused by fabrication inaccuracy and measurement limitations.

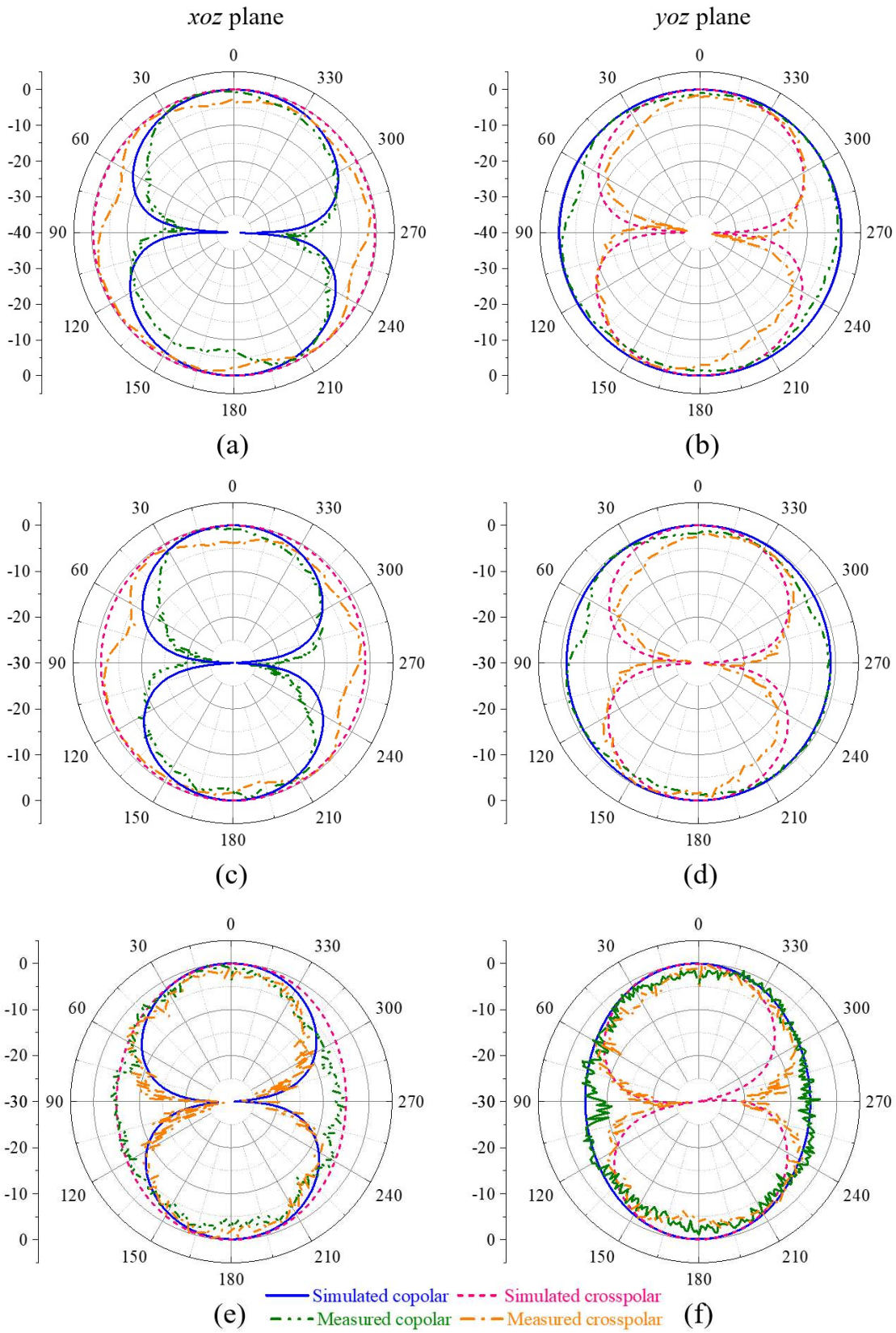

Fig. 4-20: Simulated and measured radiation patterns over (a) *xoz* plane at 1.17 GHz, (b) *yoz* plane at 1.17 GHz, (c) *xoz* plane at 1.57 GHz, (d) *yoz* plane at 1.57 GHz, (e) *xoz* plane at 2.40 GHz, and (f) *yoz* plane at 2.40 GHz.

Table 4-2: HPBW of the Proposed Antenna at Desired Frequency

	1.17 GHz	**1.57 GHz**	**2.40 GHz**
Phi=0°	353.8°	121.5°	80.9°
Phi=90°	128.4°	120.5°	79.1°

Another measurement using a pair of the proposed antenna was conducted to verify the dual CP characteristics. The measurement setup is described in Fig. 4-21, which is similar to the previous experiments but using two of the proposed crossed-dipole antennas. The two crossed-dipole antennas are placed on boresight, and the AUT is measured in two orientations with 90° difference (P_1 and P_2 as shown in Fig. 4-21). Numerical analysis was conducted using CST 2017 and the simulated and measured results are given in Fig. 4-22.

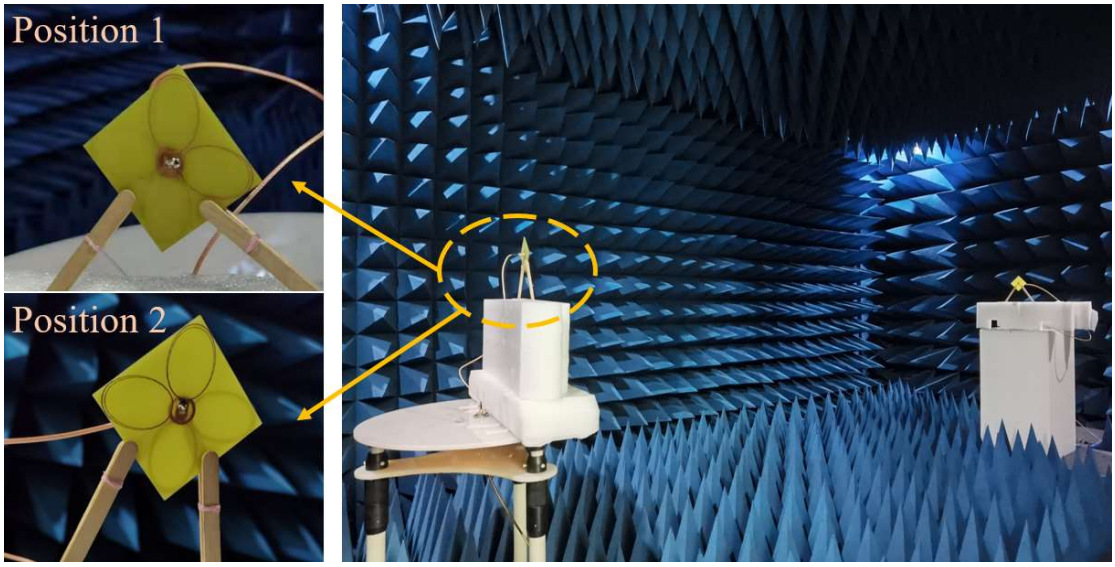

Fig. 4-21: Measurement setup in the anechoic chamber with the proposed antenna used as transmitter and receiver.

Fig. 4-22 (a) and (b) provide the simulated radiation patterns in the *xoz* and *yoz* planes, respectively. Broad unidirectional RHCP patterns are achieved in the positive *z*-direction and broad unidirectional LHCP patterns are achieved in the negative *z*-direction. The patterns are generally symmetric, which are the result of the symmetric

structure of the design. Measured radiation patterns for both cases (P_1 and P_2) are plotted in Fig. 4-22 (c) and (d). The received antenna radiates towards the boresight with low backlobes, minimising radiation towards the back side of the proposed antenna. A stable unidirectional RHCP is obtained in the positive *z*-direction with a close agreement between the simulated and measured radiation patterns in the working band.

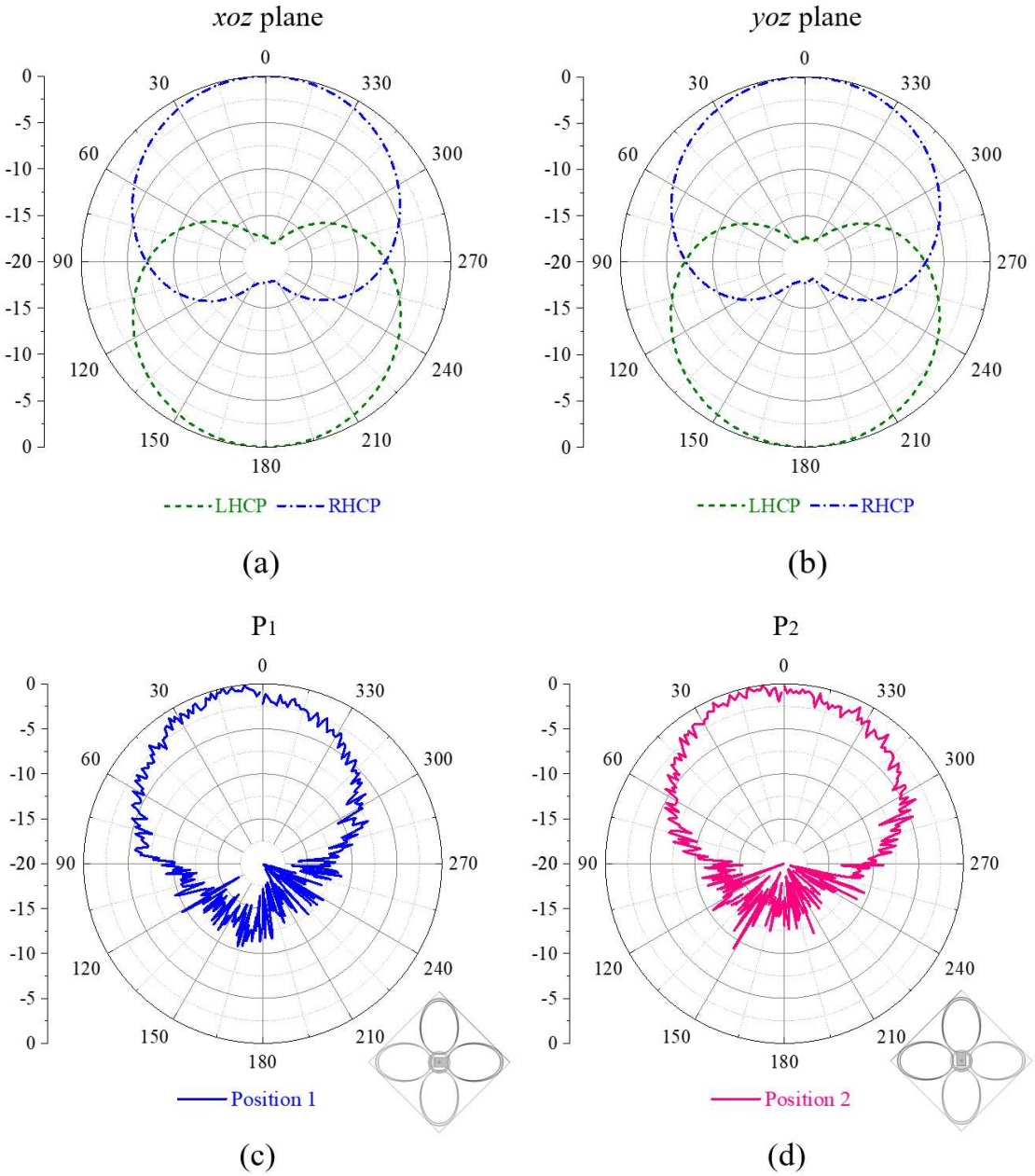

Fig. 4-22: Simulated radiation patterns at 1.57 GHz (a) on *xoz* plane, (b) on *yoz* plane; Measured radiation pattern at 1.57 GHz (c) when the received antenna places at P_1, (d) when the received antenna places at P_2.

4.3.4 Evaluations of Efficiency

The simulated total efficiency of the proposed antenna over 1.0 to 2.5 GHz is plotted in Fig. 4-23. It demonstrates that the total efficiency is greater than 85% from 1.17 to 2.50 GHz. Moreover, in the CP operating band 1.17 GHz, 1.57 GHz, and 2.40 GHz, the corresponding efficiencies are 85.6%, 90.5%, and 90.7%, respectively.

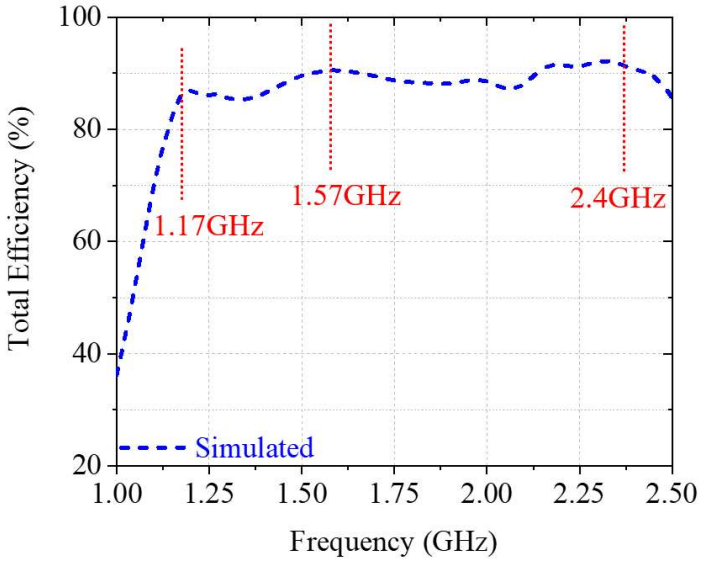

Fig. 4-23: Simulated total efficiency of the proposed antenna.

4.4 Novelty

A performance comparison between the proposed broadband dual-polarised antenna and other recently reported designs is summarised in Table 4-3 in terms of basic structure, substrate material, operation frequency bands, electrical size, polarisation, LP and CP bands, LP and CP bands functions, AR, 3 dB ARBW, and HPBW for a fuller evaluation. Overall, the proposed antenna realises a compact size and relatively wide operation bandwidth. The WMTS band is reserved for medical telemetry services and is novel in its inclusion here as other published works do not provide this functionality. Three CP bands are achieved with a relatively wide AR (6.84%, 19.11%, and 11.25% at 1.17 GHz, 1.57 GHz, and 2.4 GHz, respectively) available to be used for indoor and outdoor localisation. The 3 dB ARBW around 1.57 GHz is 120°, which meets the requirement for GPS applications. Moreover, the proposed antenna can be printed on a

low-cost PCB such as FR-4 with a compact dimension and relatively wide impedance and CP bandwidth, which makes it suitable for localising and tracking applications.

Table 4-3: Comparisons of the Proposed Antenna with Other Work

Ref.	[15]	[18]	[19]	[20]	This work
Basic Topology	Patch	Patch	Planar Monopole	Patch	Cross dipole
Substrate	RO3003C	Felt	RO4003C	NA	FR-4
***f* (GHz)**	1.564~1.593 2.439~2.457	1.575 2.45	1.88 2.5	1.228 1.575	1.15~2.62
Size (λ_0^3)	0.68 × 0.68 × 0.053	0.4 × 0.4 × 0.02	0.33 × 0.33× 0.04	0.368× 0.105 (D×H)	0.25 × 0.25 × 0.006
Polarisation	CP/LP	CP/LP	RHCP /LHCP	RHCP	LP /RHCP /LHCP
LP Bands (GHz)	2.439~2.457	2.45	NA	NA	1.4
LP function	Indoor localisation	Indoor localisation	NA	NA	Medical Telemetry Services
CP Bands	GPS L1	GPS L1	ISM (2.4 GHz)	GPS L1 GPS L2	GNSS L1/E1 GPS L5 ISM (2.4 GHz)
CP function	Outdoor localisation	Outdoor localisation	Outdoor localisation	Outdoor localisation	Indoor & Outdoor localisation
% AR (GHz)	0.70% @1.575	9.00% @1.575	2.66% @1.88 2.00% @2.50	NA	6.84% @1.17 19.11% @1.57 11.25% @2.40
3 dB AR beamwidth @ GPS L1	97.5°	NA	NA	173°	120°
HPBW (GHz)	NA	NA	81°/111°@1.88 90°/87°@2.50	107° @1.575	353.8°/128.4°@1.17 121.5°/120.5°@1.57 80.9°/79.1°@2.40

(*NA: not available)

4.5 Summary

In this chapter, a novel compact wideband dual-polarised antenna designed on a FR-4 substrate has been proposed, optimised, fabricated and evaluated for medical telemetry and indoor/outdoor localisation applications. The proposed multi-loop radiators originated from an elliptical-shape cross dipole, which can generate two orthogonal current flows with similar magnitudes but 90° phase difference. Through parameter tuning of the radiators' structure, the design achieves the target of operating over a wider frequency range than covered by other published work: WMTS band with linear polarisation, and GNSS L1/E1 band, GPS L5 band, and one ISM band (2.4 GHz) with circular polarisations. A vacant-quarter printed ring feeding network is utilised as a 90° phase delay line between the radiators on both sides of the substrate material. It allows two dipole pairs to be configured with a single feed and accomplishes CP behaviour at the desired frequency. The overall size is $64 \times 64 \times 1.57$ mm^3 ($0.25\lambda_0 \times 0.25\lambda_0 \times 0.006\lambda_0$), which can be regarded as a compact design compared to other work.

Parametric evaluations of the structural parameters including w_1, w_2, w_3, w_6, and *gap* have been conducted in CST 2017 for optimisation. With the obtained optimised dimensions, the CP characteristic has been evaluated in terms of the surface current distribution and AR at f = 1.57 GHz as an example. The overall rotation of the current distribution on the top side of the antenna is anti-clockwise, which leads to RHCP. Meanwhile, a clockwise current distribution is observed on the bottom side, which indicates LHCP exists. The related axial ratio beamwidth is 120°, which meets the required beamwidth for GPS usage.

Practical measurements have been conducted to analyse antenna performance. A portable N9917A FieldFox VNA is used to determine the impedance bandwidth and the operating bandwidth for S_{11} <-10 dB, which was 1470 MHz (from 1.15 to 2.62 GHz), meaning all desired bands are covered. Further investigations in terms of AR, radiation patterns and HPBW have been realised inside the anechoic chamber.

Good polarisation purity was achieved at 1.13 GHz, 1.46 GHz, and 2.38 GHz as $|S_{21}|_{0^\circ} \approx |S_{21}|_{90^\circ}$. The measured 3 dB AR bandwidths are around 6.84% (1.17 GHz), 19.11% (1.57 GHz) and 11.25% (2.4 GHz). Moreover, good agreement is observed between the measured radiation patterns and the simulated results, which shows the proposed antenna has a relatively good quality of CP behaviour. Overall, with the features of low profile, compact size, wide impedance bandwidth and adequate CP bandwidth (CPBW), the proposed antenna has great potential for use in WPAN applications requiring multiple RF functions.

4.6 References

[1] IEEE Standard for Low-Rate Wireless Networks, IEEE Std 802.15.4™-2020.

[2] IEEE Standard for High Data Rate Wireless Multi-Media Networks, IEEE Std 802.15.3-2016.

[3] H.-B. Li, K.-I. Takizawa, B. Zhen, and R. Kohno, "Body area network and its standardization at IEEE 802.15. MBAN," in *Proc. 16th IST Mobile Wireless Commun. Summit*, Jul. 2007, pp. 1–5.

[4] G. Fang, E. Dutkiewicz, M. A. Huq, R. Vesilo, and Y. Yang, "Medical body area networks: Opportunities, challenges and practices," in *Proc. Commun. Inf. Technol. Int. Symp.*, Oct. 2011, pp. 562–567.

[5] S. Yan, P. Soh, and G. Vandenbosch, "Wearable dual-band magneto-electric dipole antenna for WBAN/WLAN applications," *IEEE Trans. Antennas Propag.*, vol. 63, no. 9, pp. 4165–4169, Sep. 2015.

[6] J. J. H. Wang, "Antennas for global navigation satellite system (GNSS)," *Proc. IEEE*, vol. 100, no. 7, pp. 2349-2355, Jul. 2012.

[7] A. Dierck, H. Rogier, and F. Declercq, "An active wearable dual-band antenna for GPS and Iridium satellite phone deployed in a rescue worker garment," in *Proc. IEEE Int. Conf. RFID-Technol. Appl. (RFID-TA)*, Sep. 2013, pp. 1-5.

[8] W.-J. Tseng and S.-J. Chung, “A dual CP slot antenna using a modified Wilkinson power divider configuration,” *IEEE Microw. Guided Wave Lett.*, vol. 8, no. 5, pp. 205-207, May 1998.

[9] X. Cai and K. Sarabandi, “Broadband Omnidirectional Circularly Polarized Antenna with Asymmetric Power Divider,” *IEEE Trans. Antennas Propag.*, vol.68, no. 7, pp. 5171–5181, Mar. 2020.

[10] X. Qing, and Z. Chen, “Compact asymmetric-slit microstrip antennas for circular polarisation,” *IEEE Trans. Antennas Propag.*, vol. 59, no. 1, pp. 285-288, Jan. 2011.

[11] W. Chen, C. Wu, and K.Wong, “Novel compact circularly polarised square microstrip antenna,” *IEEE Trans. Antennas Propag.*, vol. 49, no. 3, pp. 340-342, Mar. 2001.

[12] S. Ma and J. Row, “Design of single-feed dual-frequency patch antenna for GPS and WLAN applications,” *IEEE Trans. Antennas Propag.*, vol. 59, no. 9, pp. 3433-3436, Sep. 2011.

[13] J. Lin, Z. Qian, W. Cao, S. Shi, Q. Wang, and W. Zhong, “A low-profile dual-band dual-mode and dual-polarized antenna based on AMC,” *IEEE Antennas Wireless Propag. Lett.*, vol. 16, pp. 2473-2476, 2017.

[14] M. Rahimi, A. Keshtkar, F. B. Zarrabi, and R. Ahmadian, “Design of compact patch antenna based on zeroth-order resonator for wireless and GSM applications with dual polarization,” *AEU-Int. J. Electron. Commun.*, vol. 69, no. 1, pp. 163-168, Jan. 2015.

[15] K. N. Paracha, S. K. A. Rahim, P. J. Soh, M. R. Kamarudin, K.-G. Tan, Y. C. Lo, and M. T. Islam, “A low profile, dual-band, dual polarised antenna for Indoor/Outdoor wearable application,” *IEEE Access*, vol. 7, pp. 33277-33288, 2019.

[16] S. X. Ta, H. Choo, I. Park, and R. W. Ziolkowski, “Multi-band, wide-beam, circularly polarised, crossed, asymmetrically barbed dipole antennas for GPS applications,” *IEEE Trans. Antennas Propag.*, vol. 61, no. 11, pp. 5771–5775, Nov. 2013.

[17] C. Liu, Y. X. Guo, and S. Xiao, “Capacitively loaded circularly polarized implantable patch antenna for ISM band biomedical applications,” I*EEE Trans. Antennas Propag.*, vol. 62, no. 5, pp. 2407–2417, May 2014.

[18] R. Joshi, *et.al*, “Dual-Band, Dual-Sense Textile Antenna with AMC Backing for Localization Using GPS and WBAN/WLAN,” *IEEE Access*, vol. 8, pp. 89468-89478, 2020.

[19] T. Yue, Z. H. Jiang, and D. H. Werner, “A compact metasurface-enabled dual-band dual-circularly polarized antenna loaded with complementary split ring resonators,” *IEEE Trans. Antennas Propag.*, vol. 67, no. 2, pp. 794-803, Feb. 2019.

[20] Z. Zhong, et.al, “A Compact Dual-Band Circularly Polarized Antenna with Wide Axial-Ratio Beamwidth for Vehicle GPS Satellite Navigation Application” *IEEE Trans. Veh. Technol.*, vol. 68, no. 9, pp. 8683–, Sept. 2019.

CHAPTER 5. TWO NOVEL SWIPT METHODS WITH HARDWARE IMPLEMENTATIONS

In Chapter 3 and Chapter 4, two novel antennas were presented for WBAN and WPAN applications supporting multiband functionality and hence enabling multiple simultaneous services to be provided. This chapter aims at developing new techniques that allow data and power to be transmitted simultaneously with reduced receiver losses. Hardware implementations from a circuit perspective are realised to facilitate a sustainable SWIPT receiver.

This chapter begins with a review of the four commonly used SWIPT receiver techniques. Limitations regarding these techniques are clarified and the direction in which this research will move is defined. Two novel techniques are proposed as alternative receiver approaches in this chapter. The first one is based on a technique named here as symbol-splitting (SS) and the second utilises a harmonic-recycling technique.

Symbol Splitting

The SS technique makes use of the fact that many common modulated signals have spectral components that represent the transmitted data and other spectral artefacts that contain only RF power. In this work SWIPT is realised by separating these spectral allowing data to be detected from the information carrying components and the power to be rectified and harvested from the remaining non-information carrying spectral components. The separation of the components is realised using a basic RF component, the rat-race coupler, between the antenna terminal and the rectifying circuit terminal. An advantage of this is that it can make use of commonly used modulations schemes such as amplitude modulation (AM), amplitude shift keying (ASK), phase shift keying (PSK). Some of these (e.g., AM) could be tweaked at the transmitter to directly adjust the amount of power the received signal would contain for rectification and hence meet

the receiver's power needs on demand and additionally, the data detection can be performed in a straightforward manner.

The integrated rectifier-receiver (IRR) realisation shows RF-to-DC PCE is over 60% when the system is supplied with an input power of -4 dBm. A PCE of around 50% is retained down to input powers of -10 dBm in measurements using both continuous wave signals and binary phase shift keying (BPSK) modulated signals with different data rates as inputs. The transferred data are correctly detected at the isolation port of the rat-race coupler.

Harmonic Recycling

The second compact hardware receiver implementation developed here is based on the unexploited third harmonics generated by the rectifying circuit required for the power transfer side of the receiver. This IRR fully utilises the entire received signal without splitting in time/power/antenna or frequency domain, the commonly applied approaches which will be discussed below. A branch-line coupler is adopted to deliver the incident waves to the rectifier and then to couple the third harmonics reflected at the rectifier input back to its isolation port. Mathematical analysis confirms the generation of third harmonics and analysis of the operating mechanism indicates the possibility of collecting the third harmonics for data reception. Measurements validate the recycling idea, and the fabricated IRR shows a maximum RF-to-DC PCE of 55.2% is reached at 920 MHz when the input power level is -7 dBm.

Practical outcomes for both designs verify the proposed architectures, which therefore become suitable for achieving stable wireless communications with simultaneous WPT for WBAN/WPAN applications.

5.1 Introduction

The concept of SWIPT was proposed by the research community as a compact way to concurrently power distributed sensors or other devices whilst exchanging information

amongst them in the downlink [1]-[3]. The received signals are separated into two distinct parts using various splitting techniques to practically implement a SWIPT system [4]-[19]. A summary of the most popular splitting techniques is provided by Fig. 5-1.

The time switching (TS) technique in Fig. 5-1(a) often employs a switch at the receiver terminal and the received waves can be used for either information detection (ID) or energy harvesting (EH) at any given time. This technique is straightforward to implement but requires precise time synchronisation for information detection.

The power splitting (PS) technique in Fig. 5-1(b) divides the received signal into two power streams for EH and ID separately. A power divider component with a designed power ratio is utilised. The major benefit is that the received signal is used for both functions in the same time slot. However, information loss is inevitable as some porting of the information part of the signal to PT occurs and vice versa.

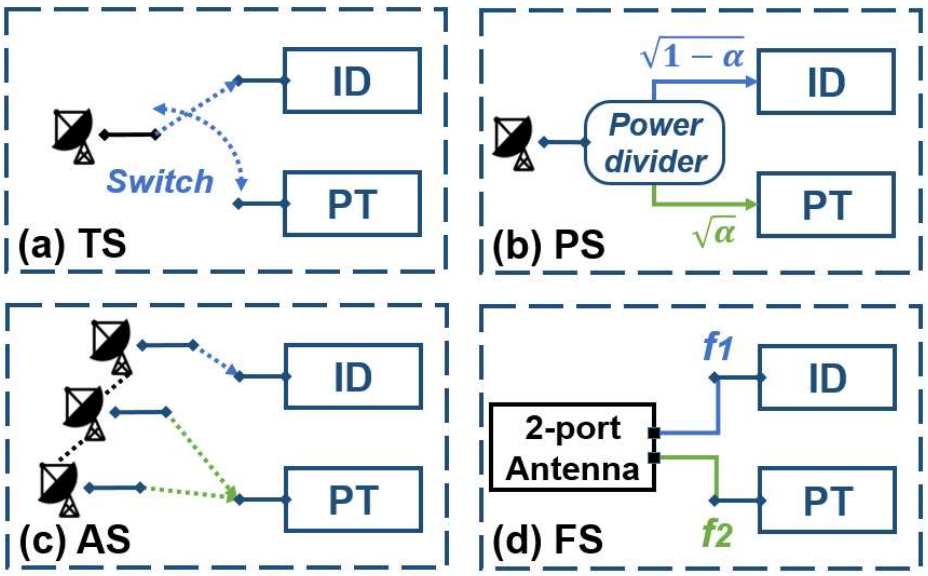

Fig. 5-1: Splitting techniques for SWIPT: (a) time switching; (b) power splitting; (c) antenna switching; (d) frequency splitting.

The antenna-switching (AS) technique in Fig. 5-1(c) and the frequency-splitting (FS) technique in Fig. 5-1(d) are similar as they use two or more frequency bands to achieve ID and EH. The information loss decreases; however, the common problem of both techniques is that they use two or more frequency bands to perform ID and EH

independently instead of dealing with the same signal concurrently. It also means that any power contained within the modulated data signal is neglected.

In this chapter, two novel techniques are proposed to achieve SWIPT with compact hardware implementations. In Section 5.2, the WPT module including analysis of several rectifier topologies and details of the circuit design process used for the rectifier are given. Section 5.3 provides a novel symbol splitting (SS) technique, which aims at separating the non-information carrying components from the information-carrying components of the received signal streams with the aid of a rat-race coupler for EH and ID, respectively. The concept of recycling reflected third harmonics generated by the rectifying circuit for ID is proposed in Section 5.4. IRR realisation and measurements are provided, analysed, and evaluated in Section 5.5 which validate the proposed splitting schemes.

5.2 WPT Module

A typical structure of the WPT receiver is depicted in Fig. 5-2.

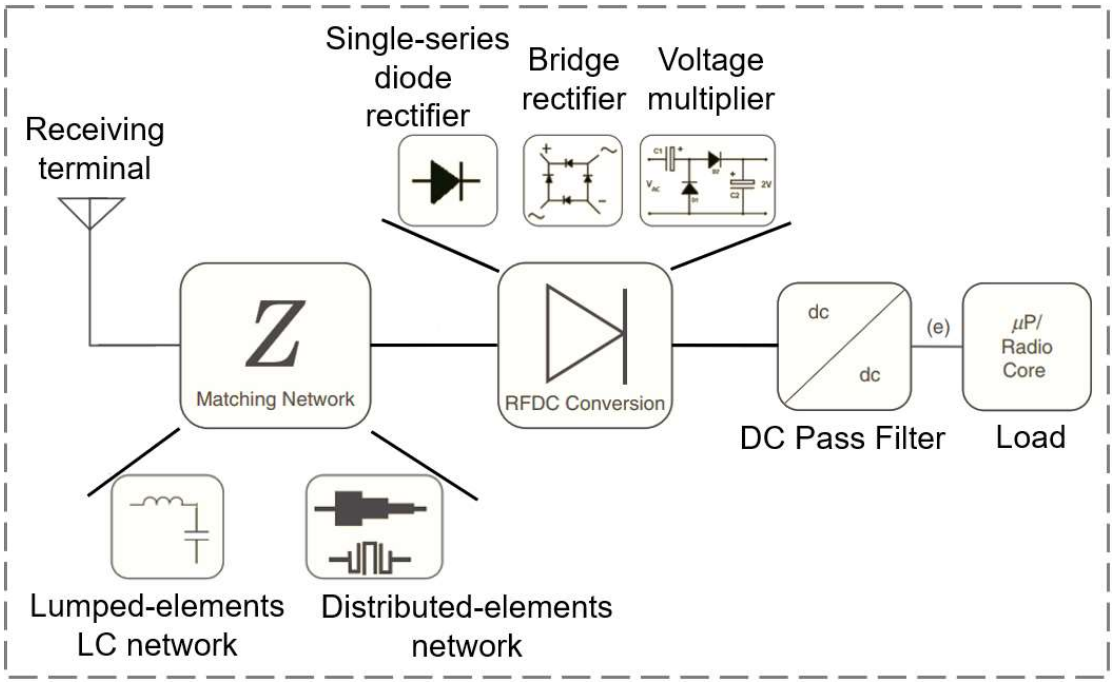

Fig. 5-2: General structure of a WPT receiver [20].

It is composed of an impedance matching network, one or multiple rectifying elements (such as diodes) for RF-DC conversion, a DC-pass filter to smooth the ripples in the rectifier output, and a load to use or save the energy collected. The design of a suitable rectifier is critical because it influences the overall RF-to-DC PCE of the IRR system severely. Therefore, four common-used topologies for RF-DC conversion will be evaluated in this section.

5.2.1 Analysis of Rectifier Topologies

A. Conventional Half-wave Rectifier

The conventional half-wave rectifier topology with a single series diode D_1 is described by Fig. 5-3. The received RF wave passes through a matching network to the rectifying element (a diode in this case). The diode then converts the RF power to DC power. The capacitor C_1 in parallel with the load functions as a low-pass filter allowing only DC to pass. This topology is simple to be constructed. However, the output voltage and PCE are low as only the positive half cycle of the received wave can be rectified by the diode and the negative half cycle is wasted blocked by the reverse biasing of the diode.

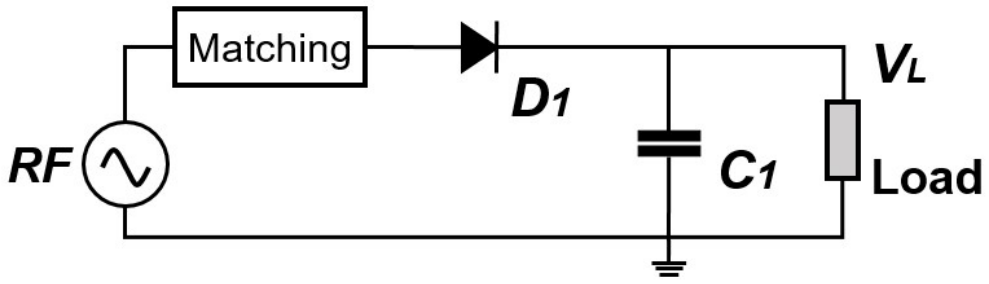

Fig. 5-3: Configuration of a conventional single series diode topology.

B. Bridge Rectifier

An improved topology called a bridge rectifier is shown in Fig. 5-4. It consists of four diodes connected in a closed-loop configuration. During the positive half cycle, the received RF wave is rectified by the diodes D_1 and D_4, and diodes D_2 and D_3 are reverse biased. During the negative half cycle, diodes D_2 and D_3 become forward biased and

rectify the received wave and diodes D_1 and D_4 are reverse biased. This topology utilises the full cycle of the received wave and ideally the PCE is double compared to the single series diode case. However, the voltage drop becomes higher as more power loss occurs due to the increased number of diodes.

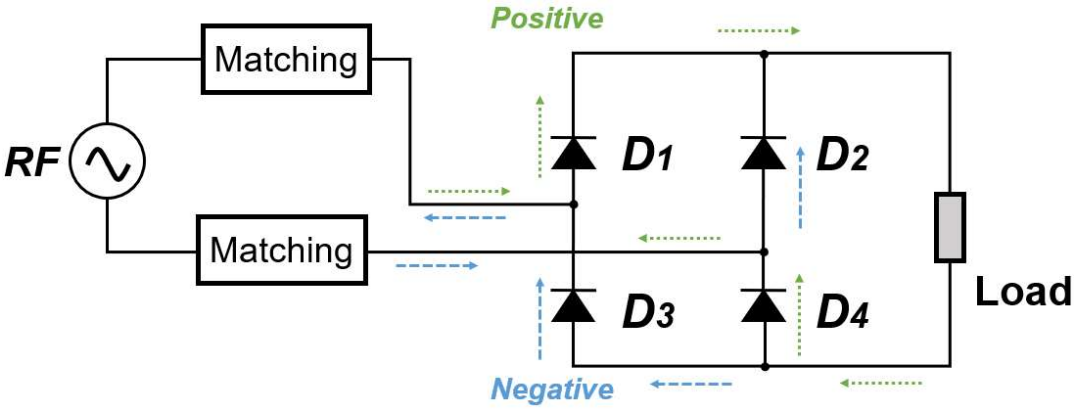

Fig. 5-4: Configuration of a bridge rectifying circuit.

C. Voltage Doubler

A further improved topology, the voltage doubler, is depicted in Fig. 5-5. The shunt diode D_1 rectifies the incoming wave and capacitor C_1 stores the energy during the negative half cycle of the circuit. When the positive half cycle arrives, the received wave is rectified by the series diode D_2 and energy is stored in capacitor C_2. In addition, Capacitor C_1 acts as an additional energy source in the positive half cycle transferring the energy it has stored to capacitor C_2. As a result, the voltage across capacitor C_2 is approximately twice the peak voltage obtained in the half-wave rectifier. The energy on C_2 is released to the load in the following period. Ideally, the voltage level is double in comparison to the single series diode case.

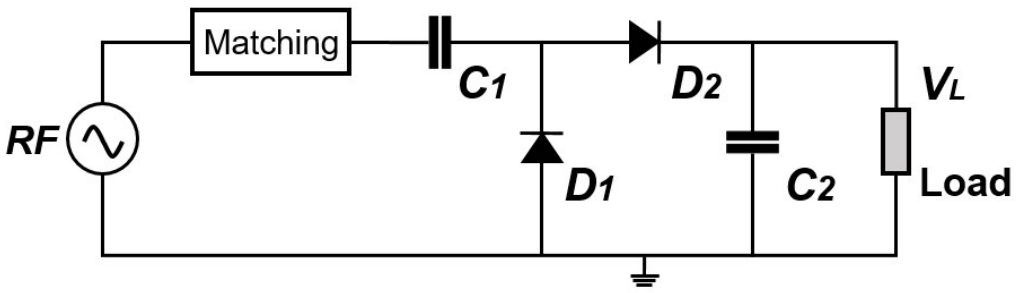

Fig. 5-5: Configuration of a voltage doubler rectifying circuit.

D. Greinacher rectifier

The final topology considered here is shown in Fig. 5-6, a full wave rectifying circuit called Greinacher rectifier [21] [22]. It is composed of two voltage doublers formed in a bridge configuration with diodes placed in the opposite direction. Compared to the voltage doubler topology discussed previously, this circuit amplifies the voltage across the load. The voltage on the load is expressed by $V_{DC} = |V^{+} - V^{-}|$.

The RF-to-DC PCE can be calculated by Eq. (5.1):

$$PCE = \frac{P_{DC}}{P_{input}} = \frac{V_{DC}^{\ 2}}{P_{input} R_L} \tag{5.1}$$

where P_{DC} is the output DC power, P_{input} is the input power, V_{DC} is the total output DC voltage, and R_L is the load impedance.

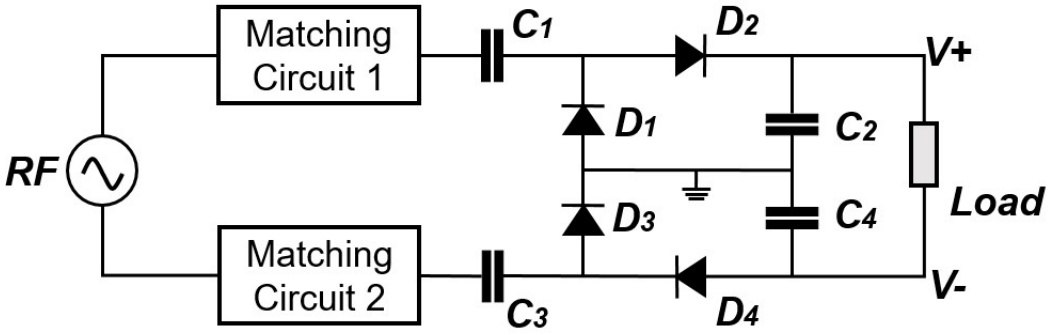

Fig. 5-6: Configuration of a full-wave Greinacher rectifying circuit.

5.2.2 Design Process of Rectifier in ADS2017

Simulations are conducted using the RF circuit simulation software Advanced Design System 2017 (ADS 2017).

The selection of the rectifying elements (such as diodes) is crucial for the overall performance of the rectifier circuit. In this work, the packaged Schottky diode SMS7630 is selected due to its low bias voltage requirement (60-120 mV at 0.1 mA) for a low power incident wave, a high saturation current, and low power loss [23]. The corresponding nonlinear Spice model with parasitic elements provided by *Skyworks*

Solutions Inc. [23] is adopted for simulation. The chip inductors and chip capacitors used in the matching circuits and the rectifier's chip capacitors are simulated as their real product models including *S*-parameter files provided by suppliers *Coilcraft* and *Murata* to improve simulation accuracy.

In addition to careful selection of the rectifying elements, the design of an impedance matching circuit is also important as it determines how much power can be transferred to the rectifying module from the antenna. The input impedance of the rectifying circuit varies when either frequency, input power or load impedance changes owing to the nonlinear property of the rectifying circuit. Therefore, the impedance matching network should assist the rectifying circuit to match the dynamic characteristics of the input to improve overall system performance.

An EM/Circuit co-simulation has been conducted in ADS 2017. The general process is as follows.

1. Circuit simulation

The Harmonic Balance (HB) and Large-signal *S*-parameter (LSSP) simulators are used in the schematic to analyse the non-linear behaviour of the diodes and find the steady-state solution in the frequency domain. The nonlinear input impedances of the rectifying circuit versus input power level are exported as touchstone *S1P* files and then Impedance Matching Toolkits are applied to find the initial values of the matching inductors and capacitors. Further optimisation of the impedance matching circuit is performed which aims to have a bandpass response, passing the fundamental frequency of received wave while rejecting the higher order harmonics generated by the rectifying circuit (nonlinear elements), further improving PCE.

2. EM simulation

Different from circuit simulation, EM simulation is used on the circuit layout. After optimisation in the schematic, a layout should be created based on the schematic, which contains all microstrip components created in the schematic. The general procedure at

this stage is: connect the pins in the layout, select the right Momentum simulator (Method of Moments), define the substrate, and setup the simulation frequency plan. The results obtained from the Momentum simulation are more accurate as it considers the potential effects such as coupling between the microstrip elements and the board edge.

3. Co-simulation

A co-simulation is required as EM solvers cannot simulated discrete components such as resistors, inductors, capacitors, and diodes. A layout component of the microstrip parts is created and then placed into the schematic, where the discrete components can be connected. The appropriate simulators (HB and LSSP) can then be set up in the schematic and the simulation performed. If the results are desirable, fabrication can be organised with the exported layout file.

5.3 SWIPT by Symbol-Splitting Technique

In this section, a compact SWIPT receiver architecture based on the novel SS technique is proposed. The purpose of this technique is to separate the non-information carrying frequency components from the information-carrying components of received modulated signals, with the aid of a conventional rat-race coupler. The block diagram of the IRR topology is given in Section 5.3.1 and theoretical analysis of the SS technique is explained in Section 5.3.2 followed by the design of rectifier in Section 5.3.3.

5.3.1 Rat-race Coupler-based IRR Topology

The proposed system topology is depicted in Fig. 5-7. A rat-race coupler is placed between a receiving antenna and a rectifying network. P_1 to P_4 in Fig. 5-7 represent the four ports of the coupler. P_1 is connected to the antenna acting as the supply port to the system. P_2 and P_3 are connected to each branch of the Greinacher rectifying circuit each via matching networks. V^+ and V^- are the amplitudes of the output DC signals across a

load, rectified in different directions by the positive and negative sub-rectifiers, respectively. The voltage across the load is $|V^+ - V^-|$. P_4 is connected to a digital oscilloscope where the extracted signal waveform can be detected.

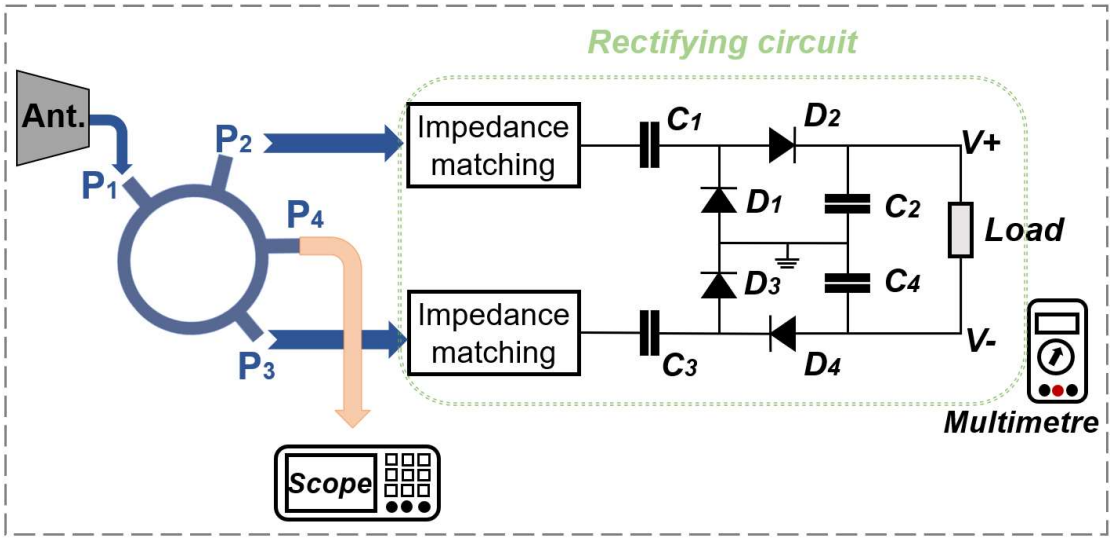

Fig. 5-7: Schematic of the proposed topology with a rat-race coupler.

The rat-race coupler (also known as a hybrid ring coupler), is a 3 dB power splitter widely used in RF and microwave systems [24]. It has four ports, each spaced at a distance of $\lambda/4$ around half of the ring circumference. The total circumference of a rat-race coupler is 1.5λ. As shown in Fig. 5-15, a wave entering port P_1 will be equally divided into two waves travelling in opposite directions around the ring. These two waves have travelled distances of $\lambda/4$ and $5\lambda/4$ respectively to reach port P_2; meanwhile they have each travelled distances of $3\lambda/4$ to reach port P_3. The signals at ports P_2 and P_3 have a difference of $\lambda/2$, which mean the signal at port P_3 is out-of-phase with that at port P_2. The two waves travel around the ring $\lambda/2$ and λ respectively to reach port P_4, which means they are out of phase and carry zero power to the output. Thus, port P_4 is well-isolated from port P_1. The *S*-parameter matrix for an ideal rat-race coupler is given in Eq. (5.2) according to the odd-even mode theory [25].

$$S = -\frac{1}{\sqrt{2}}\begin{bmatrix} 0 & j & -j & 0 \\ j & 0 & 0 & j \\ -j & 0 & 0 & j \\ 0 & j & j & 0 \end{bmatrix} \tag{5.2}$$

The simulated *S*-parameters (in dB) of a rat-race coupler designed on RT/Duroid 5880 (relative permittivity $\varepsilon_r = 2.2$ and thickness of 1.575 mm) substrate are shown in Fig. 5-8. These figures demonstrate the possibility of differentially distributing the incident signal at f_c (2.45 GHz is selected) from port P_1 to ports P_2 and P_3 ($S_{21} \approx S_{31} \approx$ -3 dB, $S_{21} \approx S_{31}$*), where port P_1 is well matched ($S_{11} \approx$ -21 dB), and port P_4 is well-isolated ($S_{41} \approx$ -46 dB, $S_{44} \approx$ -20 dB).

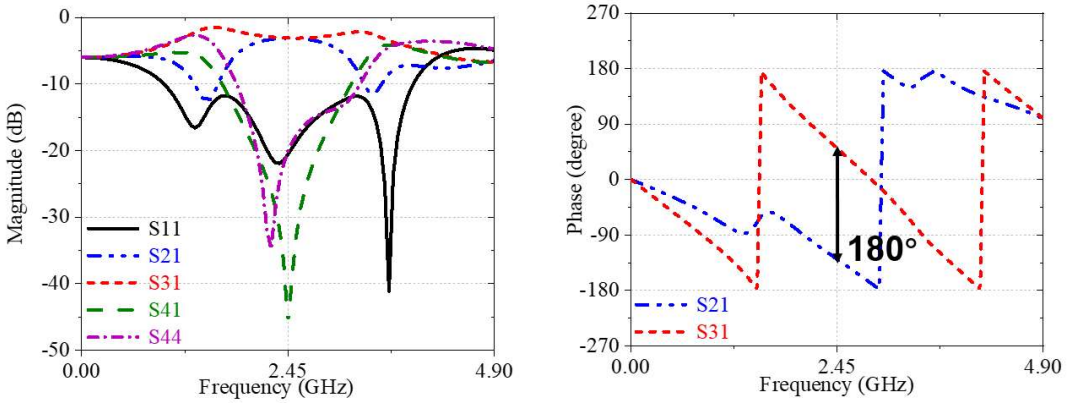

Fig. 5-8: Simulated *S*-parameters of the rat-race coupler designed on RT/Duroid 5880: (a) magnitudes of S_{11}, S_{21}, S_{31}, S_{41}, S_{44} and (b) phases of S_{21}, S_{31}.

5.3.2 Mechanism of SS

BPSK is selected as an example to show how SS works as it is one of the most commonly utilised modulation schemes and is approved for low-rate wireless networks according to the IEEE Standard for Low-rate Wireless Network [26]. The expressions describing a BPSK modulated signal are given in Eq. (5.3)-(5.6):

Binary '0':

$$s_0(t) = V_m \sin(2\pi f_c t), \quad 0 \le t < \mathrm{T_b} \tag{5.3}$$

Binary '1':

$$s_1(t) = V_m \sin(2\pi f_c t + \pi), \quad 0 \le t < \mathrm{T_b} \tag{5.4}$$

and

$$\mathrm{T_b} = N\mathrm{T}_c \tag{5.5}$$

Transmission data rate R_b:

$$R_b = \left(f_c / N \right) \tag{5.6}$$

where f_c is the carrier frequency, T_c is the carrier period, T_b is the bit duration, N is the number of carrier cycles in T_b, and V_m is the amplitude.

Every T_b seconds, the modulator transmits one of these two carrier bursts corresponding to the information bit being '0' or '1'. Eq. (5.3) and (5.4) can be re-written as in Eq. (5.7):

$$s_1\left(t\right) = V_m \sin(2\pi f_c t) + V_m \mathrm{rect}(t) \bullet \left\{ \sin(2\pi f_c t + \pi) - \sin(2\pi f_c t) \right\} \tag{5.7}$$

and the rectangular pulse rect(t) is:

$$\mathrm{rect}(t) = \begin{cases} 0, & \mathrm{T_b} \le \mathrm{t} \\ 1, & 0 \le t < \mathrm{T_b} \end{cases} \tag{5.8}$$

Comparing Eq. (5.3) and (5.4) to Eq. (5.7), the common term between bit '0' and bit '1' is the first term $V_m \sin(2\pi f_c t)$ which is a pure sine signal. Hence, this term is defined as the non-information carrying component. The information carried entirely depends on the remainder of the expression $\mathrm{rect}(t) \bullet \left\{ \sin(2\pi f_c t + \pi) - \sin(2\pi f_c t) \right\}$. As a result, this term is defined as the information-carrying component.

From a frequency response perspective, the data sequence (base signal) is a continuous sinc() function over the frequency spectrum as shown in Fig. 5-9(a). The carrier in Fig. 5-9(b) is an impulse centred at f_c. The convolution of them becomes the corresponding frequency spectrum of the BPSK signal as depicted in Fig. 5-9(c). The core idea of the SS technique is to extract the impulse at f_c for rectification and retain the remainder for data detection. Based on the principal behaviour of a rat-race coupler, the *narrow-band band-stop* property of the isolation port offers a route to SS. The impulse at f_c will pass through ports P_2 and P_3 with the remainder rejected. The *narrow-band band-stop* property of the isolation port will reject the main impulse and reflect it back to ports P_2

and P_3 (which has been proved to further improve the PCE in [27]) and allow the continuous part to pass through. Therefore, an incoming wave that arrives at port P_1 will be equally divided and delivered to ports P_2 and P_3 with the information-carrying components being 'filtered' through port P_4. A digital oscilloscope can be connected to port P_4 to detect the output waveform.

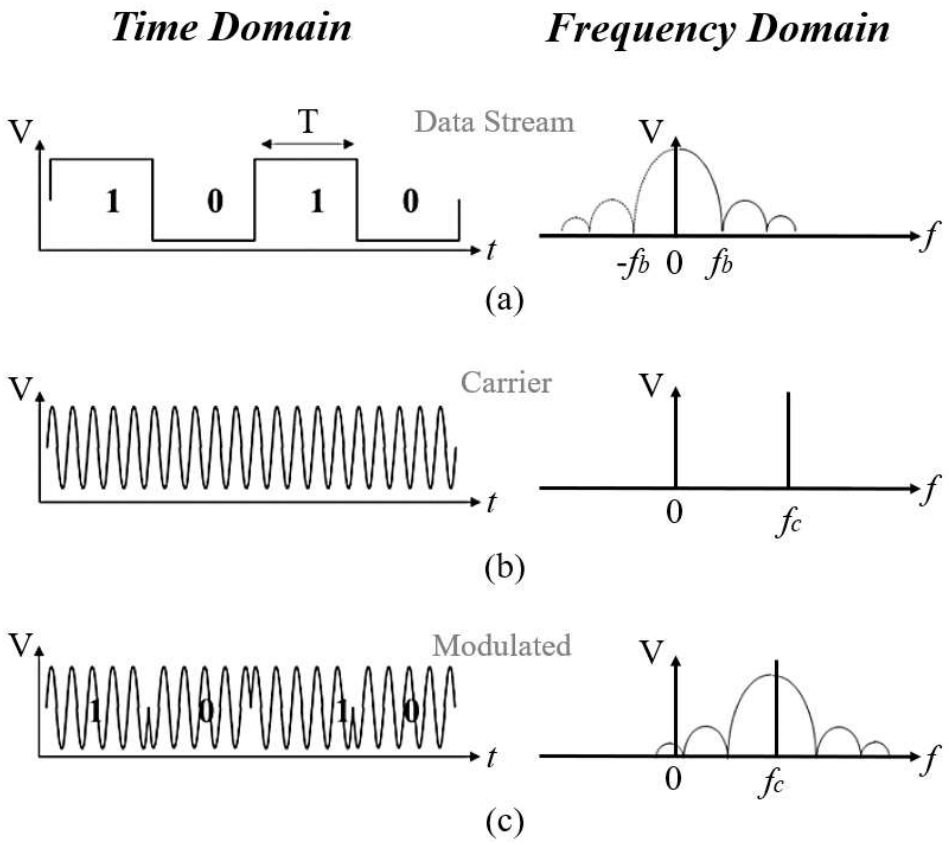

Fig. 5-9: Frequency response of (a) base signal; (b) carrier signal; (c) modulated BPSK signal [28].

5.3.3 Rectifier Design

The Greinacher rectifier is selected for use in the IRR. The layout and optimised parameter dimensions for the rectifier circuit designed on RT/Duroid 5880 substrate are given in Fig. 5-10 and Table 5-1.

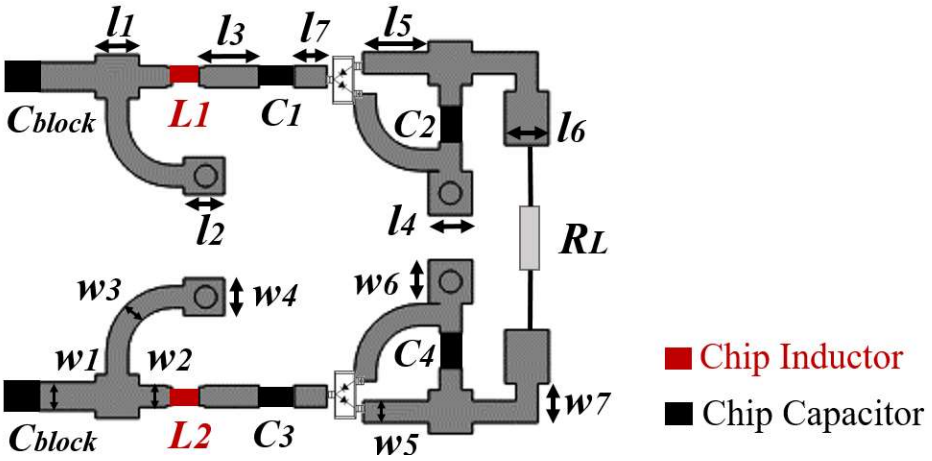

Fig. 5-10: Layout of the rectifying circuit.

Table 5-1: Optimised Circuit Dimensions (Millimetre)

Parameter	Value	Parameter	Value	Parameter	Value
l_1	2.00	w_1	2.78	L_1	2 nH
l_2	1.70	w_2	1.30	L_2	2 nH
l_3	2.50	w_3	1.00	C_1	100 nF
l_4	2.00	w_4	1.70	C_2	100 nF
l_5	3.00	w_5	1.00	C_3	100 nF
l_6	2.00	w_6	2.00	C_4	100 nF
l_7	1.50	w_7	0.79	C_{block}	20 pF
L	49.3	W	51.7		

5.4 SWIPT by Recycling Third Harmonics

In this section, another novel data detection technique based on the recycling of the third harmonics generated and reflected by the rectifier is proposed, together with the design of a compact receiver architecture to facilitate the method for SWIPT. A 3 dB

directional coupler is employed here as it can deliver the incident received wave, at its fundamental frequency f_0, to the rectifier and couple the third harmonic waves reflected from the rectifier input to the isolation port. This reflected third harmonic is verified to carry the same information as is contained in the received signal at the fundamental frequency. The IRR topology is provided in Section 5.4.1 and a detailed theoretical analysis of the third harmonic, including its generation and extraction is discussed in Section 5.4.2. Modulation schemes which can be adopted are discussed in Section 5.4.3 and the rectifier design with detailed dimensions is provided in Section 5.4.4.

5.4.1 Branch-line Coupler-based IRR Topology

The proposed system topology is depicted in Fig. 5-11. A 3-dB branch-line coupler in which the phase of the coupled signals ideally differs by 90° is used. P_1 to P_4 in this diagram are the four ports of the branch-line coupler. The coupled ports, P_2 and P_3 are connected to rectifying circuits (rectifier 1 and rectifier 2 respectively as shown in Fig. 5-11). V_1 and V_2 are the amplitudes of the output DC signals across a load, rectified by the positive-direction rectifier (Rectifier 1) and negative-direction rectifier (Rectifier 2), respectively. The isolation port P_4 is connected to a digital oscilloscope to present the detected output waveform.

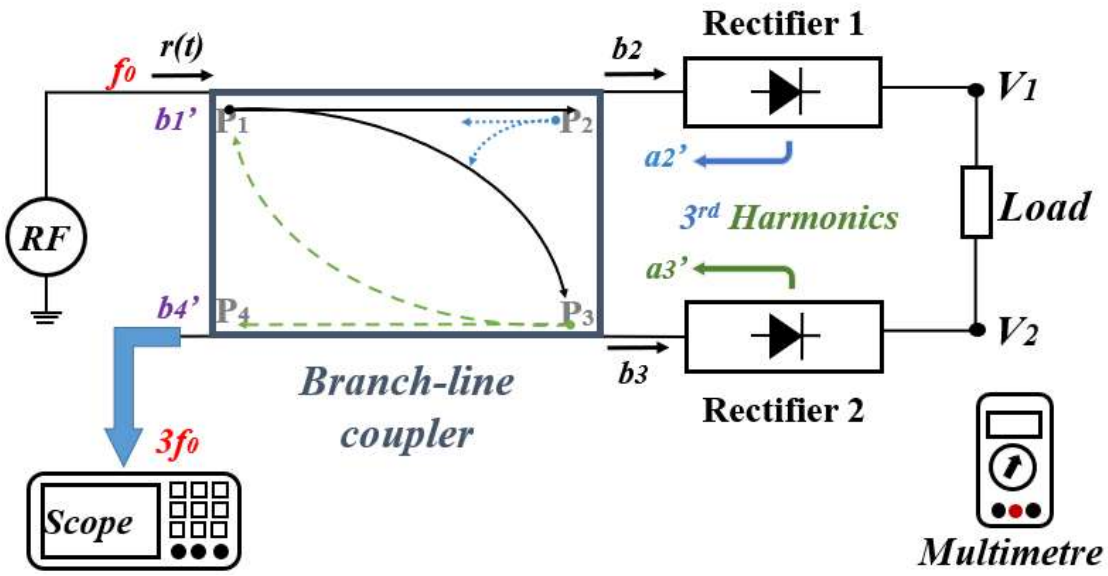

Fig. 5-11: Block diagram of the proposed IRR topology based on a branch-line coupler.

The fundamental structure of a directional branch-line coupler is composed of four $\lambda/4$ transmission lines with matched terminations at all four ports. As is shown in Fig. 5-11, the incident waves entering port P_1 will be equally divided to ports P_2 and P_3 where P_2 is leading P_3 by 90°. There is no output at the fundamental frequency f_0 leaked to port P_4, but signals at other frequencies can pass from P_4. The *S*-parameter matrix of an ideal branch-line coupler at its fundamental operating frequency is given in Eq. (5.9):

$$S=\frac{1}{\sqrt{2}}\begin{bmatrix} 0 & -j & -1 & 0 \\ -j & 0 & 0 & -1 \\ -1 & 0 & 0 & -j \\ 0 & -1 & j & 0 \end{bmatrix} \tag{5.9}$$

According to [29], the symmetry property and characteristic impedance of this coupler maintain the same operation for the frequency $3f_0$. The *S*-parameter matrix for $3f_0$ is expressed as Eq. (5.10):

$$S=\frac{1}{\sqrt{2}}\begin{bmatrix} 0 & j & -1 & 0 \\ j & 0 & 0 & -1 \\ -1 & 0 & 0 & j \\ 0 & -1 & j & 0 \end{bmatrix} \tag{5.10}$$

The *S*-parameter results from EM simulations in ADS2017 of the branch-line coupler at f_0 = 920 MHz are shown in Fig. 5-12. At f_0 = 920 MHz, the designed microstrip coupler can equally distribute the input wave to ports P_2 and P_3 (S_{21} = -2.97 dB ≈ -3 dB, S_{31} = -3.08 dB ≈ -3 dB) with a 90° phase difference. There are almost no reflections at the input port P_1 which is well matched (S_{11} ≈ -41.9 dB) and the isolation port P_4 is well-isolated (S_{41} ≈ -45.6 dB).

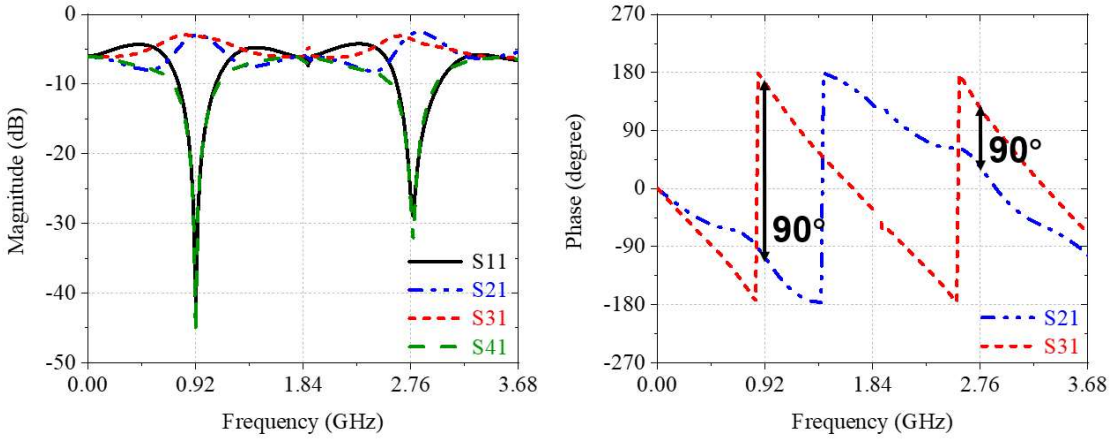

Fig. 5-12: Simulated *S*-parameters of a branch-line coupler designed on RT/Duroid 5880: (a) magnitudes of S_{11}, S_{21}, S_{31}, S_{41}, S_{44} and (b) phases of S_{21}, S_{31}.

At $3f_0$ = 2740 MHz, the overall trend is similar to the phenomenon at f_0. The transmission coefficients S_{21} = -2.9 dB and S_{31} = -3.2 dB, which are almost equal to -3 dB. The phase difference at $3f_0$ is around 90°. Reflection coefficients $S_{11} \approx$ -26.6 dB and $S_{41} \approx$ -27.2 dB indicate that there are almost no reflections found at the input port and the isolation port is well-isolated. Therefore, a branch-line coupler can work at its fundamental frequency f_0 and the third harmonic frequency $3f_0$.

5.4.2 Generation & Extraction of Third Harmonics

The channel attenuation (channel fading) is normalised to one without loss of generality so as to clarify the key point of the proposed idea. Assume a single-tone RF signal *r(t)* is received at the input port P_1 as shown in Fig. 5-11, it can be expressed by Eq. (5.11):

$$r(t) = k_1 \cos(2\pi f_0 t + \theta) \tag{5.11}$$

where k_1 is the amplitude and θ is the initial phase value.

According to the *S*-parameters matrix shown in Eq. (5.9), the streams distributed to the two rectifiers (connected to P_2 and P_3) can be expressed as Eq. (5.12) and Eq. (5.13):

$$b_2 = -jr(t) / \sqrt{2} \tag{5.12}$$

$$b_3 = -r(t)/\sqrt{2} \tag{5.13}$$

The output response of each rectifier can be modelled as a Taylor series [25], shown in Eq. (5.13) for V_2 in terms of b_3, and similarly for V_1 in terms of b_2:

$$V_2 = p_0 + p_1 b_3 + p_2 b_3^{\,2} + p_3 b_3^{\,3} + p_4 b_3^{\,4} + \ldots \tag{5.14}$$

where $p_0 \sim p_4$ are the Taylor expansion coefficients.

The nonlinear response of the two rectifiers will generate third harmonic reflections back to ports P_2 and P_3 as inputs to the coupler. These reflections then will be delivered to port P_1 (input port) and port P_4 (isolation port). According to Eq. (5.14), the third harmonics are generated from term $p_3\, b_3^{\,3}$ (and $p_3\, b_2^{\,3}$). Even though higher orders such as $b_3^{\,5}$ (and $b_2^{\,5}$) and $b_3^{\,7}$ (and $b_2^{\,7}$) can also generate $3f_0$ terms, the magnitudes are small compared to that of term $b_3^{\,3}$ (and $b_2^{\,3}$), and can therefore be neglected.

According to trigonometric equalities,

$$b_3^{\,3} = -\frac{1}{2\sqrt{2}} r(t)^3 = -\frac{1}{2\sqrt{2}} \left[k_1 \cos(2\pi f_0 t + \theta)\right]^3 \tag{5.15}$$

Thus, the third harmonics a_2' and a_3' exported to P_2 and P_3 are

$$a_3' = -\frac{1}{8\sqrt{2}} p_3 k_1^{\,3} \cos(6\pi f_0 t + 3\theta) \tag{5.16}$$

$$a_2' = \frac{j}{8\sqrt{2}} p_3 k_1^{\,3} \cos(6\pi f_0 t + 3\theta) \tag{5.17}$$

Based on the branch line coupler discussed previously, the output received at ports P_1 and P_4 are as follows. The reflections back to the source at P_1 are out of phase and cancel with each other as shown in Eq. (5.18) and the third harmonic with 3 times the phase and regular amplitude changes is exported to and exits port 4 Eq. (5.19).

$$b_1' = \frac{j}{\sqrt{2}} a_2' - \frac{1}{\sqrt{2}} a_3' = 0 \tag{5.18}$$

$$b_4^{'} = -\frac{1}{\sqrt{2}} a_2^{'} + \frac{j}{\sqrt{2}} a_3^{'} = -\frac{1}{8} j p_3 k_1^{\,3} \cos(6\pi f_0 t + 3\theta) \tag{5.19}$$

Therefore, the third harmonic products which contain the transmitted information are coupled to the isolation port of the coupler and offer an opportunity to be used for ID. Compared to other splitting techniques discussed before, this technique allows all the received wave to be used for rectification and the generated products from the rectification to be used for ID instead of eliminating them.

5.4.3 Viable Modulation Schemes

Modulated signals that can be represented by Eq. (5.11) are adoptable for use in this technique, including, amplitude shift keying (ASK) and amplitude ratio shift keying (ARSK). Comparing the use of ASK and ARSK, the influence of the distance between the base station and the sensing device can be eliminated by using the ratio (K) instead of the absolute value of amplitude. A received two-tone ARSK modulated signal can be written as:

$$r(t) = k_1 \cos(2\pi f_1 t) + k_2 \cos(2\pi f_2 t) \tag{5.20}$$

where k_1 and k_2 are the amplitudes at frequency f_1 and f_2 respectively. Note that k_1, $k_2 > 0$ and $k_1 < k_2$.

In this case, symbols are independent of the distance and channel attenuation to k_1 and k_2 are cancelled. Using the Taylor series expansion and considering the properties of the coupler, the third harmonic terms can be modelled as

$$b_4^{'} = r_1 \cos(6\pi f_1 t) + r_2 \cos(6\pi f_2 t) \tag{5.21}$$

The ratio $K = r_1 / r_2$ is with $r_1 = -jp_3 k_1^{\,3} / 8$ and $r_2 = -jp_3 k_2^{\,3} / 8$. To decode the data the third harmonic signal must be sampled and processed by FFT.

5.4.4 Rectifier Design

The voltage doubler rectifier topology is selected to be used for each branch of the branch-line coupler due to the relative size of the coupler. The layout is plotted in Fig. 5-13 and the optimised geometrical parameters for RT/Duroid 5880 substrate are detailed in Table 5-2.

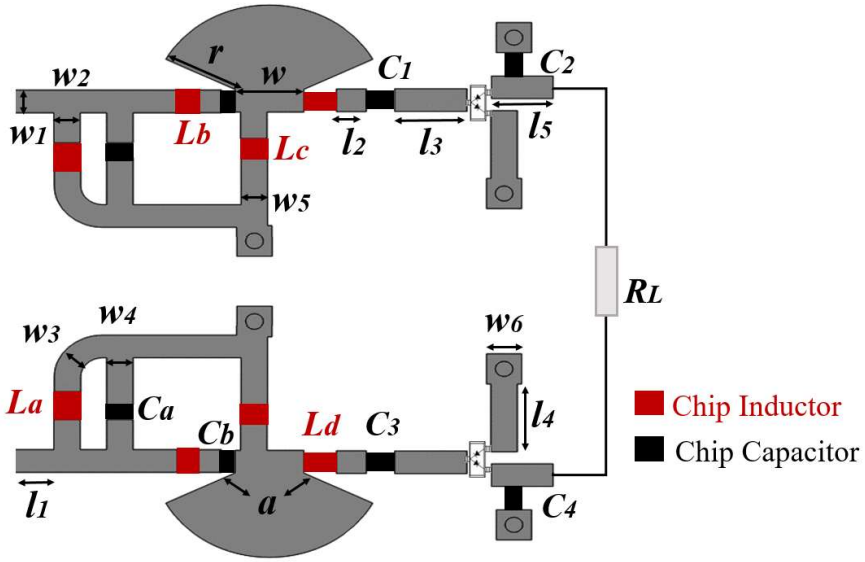

Fig. 5-13: Layout of the rectifying circuit for the proposed system.

Table 5-2: Optimised Circuit Dimensions (Millimetre)

Parameter	Value	Parameter	Value	Parameter	Value
l_1	1.2	w_4	1.5	L_c	43 nH
l_2	1.7	w_5	1.5	L_d	18 nH
l_3	4.1	w_6	2	C_a	36 pF
l_4	4.5	w	3.9	C_b	9.9 pF
l_5	3.5	r	4.4	C_1	100 nF
w_1	1.5	a	126°	C_2	100 nF
w_2	1.5	L_a	6.8 nH	C_3	100 nF
w_3	1.5	L_b	16 nH	C_4	100 nF

5.5 IRR Realisation and Measurements

5.5.1 Validation of IRR for SS Technique

The final topology of the proposed SS IRR is demonstrated in Fig. 5-14. The overall dimension of the optimised design is $L \times W = 51.7 \times 49.3$ mm^2 and the inner space of the rat-race coupler is used to house the rectifier miniaturising the board size. The antenna is excluded from the design because the main goal here is to investigate the proposed SS receiving topology standalone.

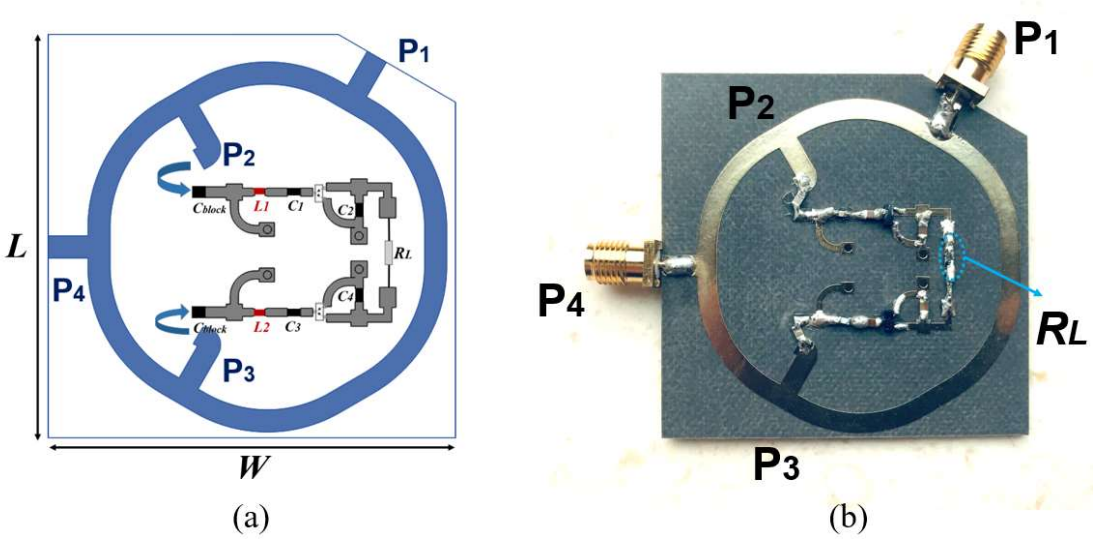

Fig. 5-14: Topology and fabricated prototype of the proposed IRR system.

The validation setup is given in Fig. 5-15. Input Port P_1 of the system is connected to a signal generator (Keysight EXG N5173B analogue signal generator or Agilent E4438C signal generator), and a Rohde & Schwarz RTO2044 oscilloscope is connected to the isolation port P_4 for the purpose of observing the output waveforms of the information-carrying components. A digital multi-meter is used across the load to measure the output DC voltage allowing the PCE to be calculated using Eq. (5.1).

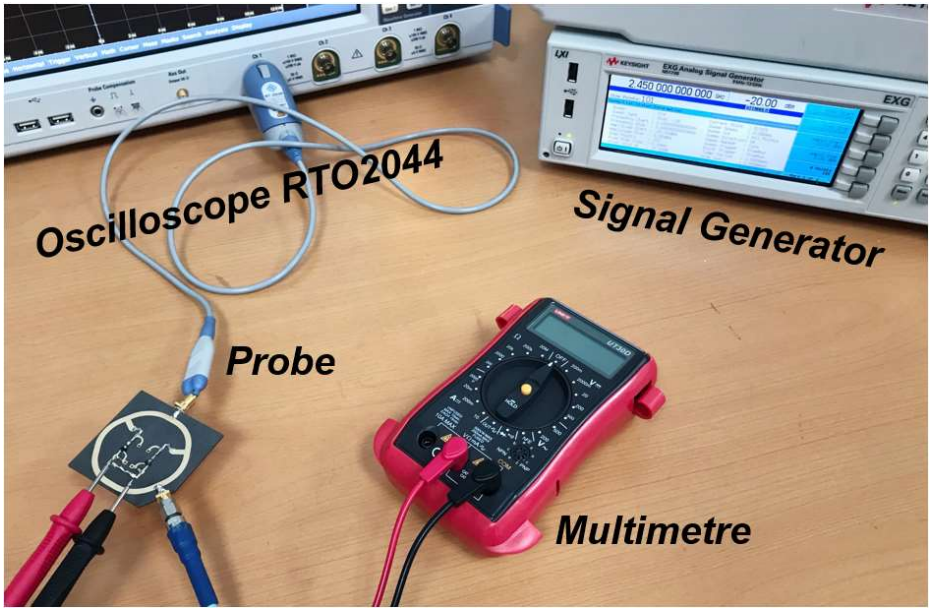

Fig. 5-15: Realisation of experimental validation setup with the fabricated prototype.

A. Data Detection Ability

The same BPSK base sequence is used in both simulation and measurement (programmable from the signal generator) '010110'. The power of the input modulated signal is set to 0.2 mW (-7 dBm). According to the working principle of the coupler ($S_{21} \approx S_{31} \approx$ -3 dB), the actual waves arrive at ports P_2 and P_3 depicted in Fig. 5-16(c) with a power of ≈ 0.1 mW (-10 dBm). Fig. 5-16(d) and Fig. 5-16(e) demonstrate the simulated and measured output waveforms captured at port P_4 of the rat-race coupler, respectively. Both simulated and measured waveforms from port P_4 only contain phase changes compared with the transmitted modulated waveform. The measured voltage level of the output waveform is 0.142 V at the transition point, which is around half of that of the transmitted signal.

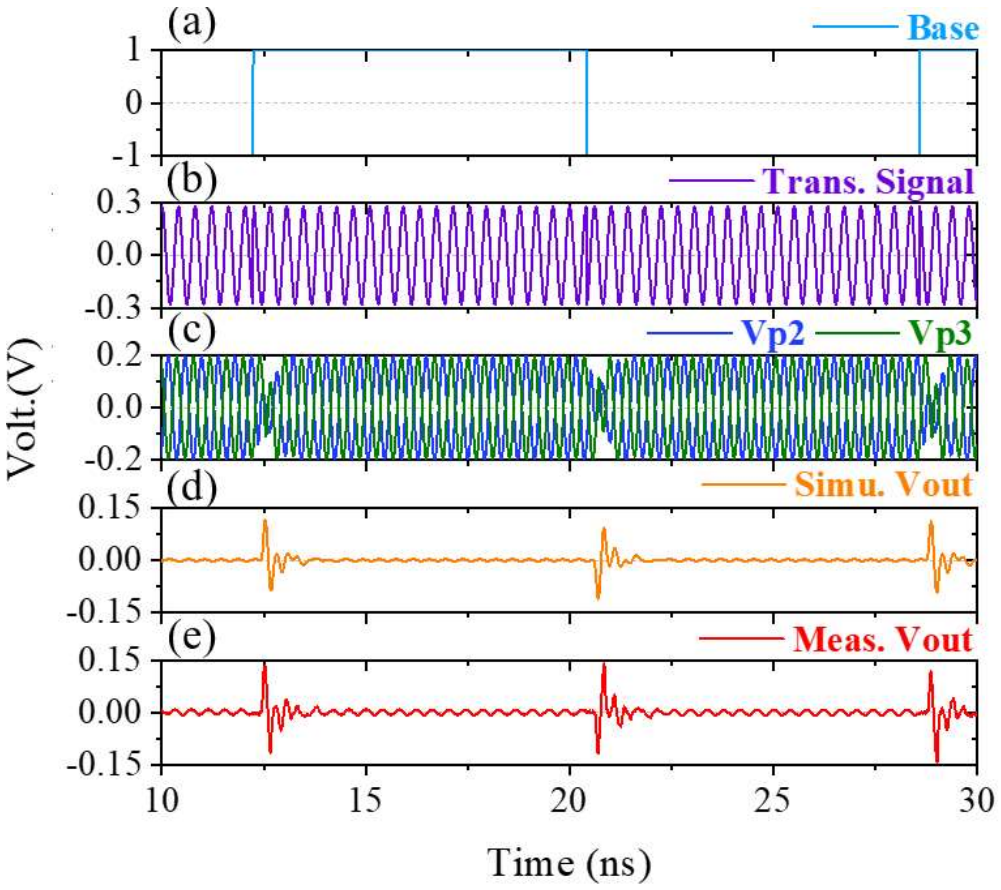

Fig. 5-16: Voltage waveforms of the (a) simulated base signal, (b) simulated transmitted signal, (c) simulated incoming signal at ports P_2 & P_3, (d) simulated output signal from port P_4 and (e) measured output signal from port P_4 within 20 ns.

B. System PCE Performance

The simulated and measured PCE of the proposed circuit as a function of input power level is demonstrated in Fig. 5-17 when receiving a CW wave. PCE increases with increasing input power up to the point where the reverse breakdown voltage of the diodes is reached, with the maximum results for simulation and measurement being 64.95% at -4 dBm and 64.60% at -3 dBm respectively. At this point, the efficiencies start to decrease due to the reverse voltage breakdown. In general, it remains over 40% for input powers $>$ -15 dBm. The slight differences between simulation and measurement results are likely due to fabrication errors (*e.g.*, manual soldering), the tolerance in parasitic behaviour of the SMD components, or higher loss of the components than the loss of the values set for the product models used in the simulation.

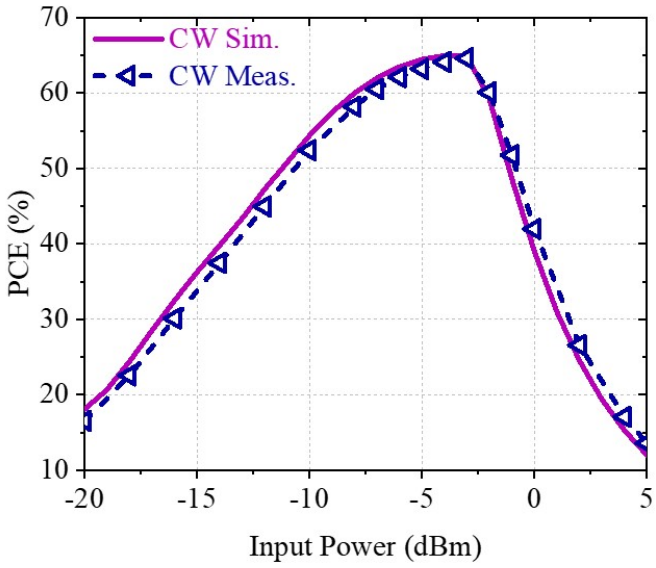

Fig. 5-17: Simulated and measured PCEs versus input power level for CW case.

The measured PCE of the proposed system as a function of the input power level at bit rates of R_b = 49 Mbps, 81.6 Mbps, and 245 Mbps are demonstrated in Fig. 5-18 when BPSK signals are applied. Overall, PCEs for modulated signals are lower than those for CW signals. Maximum PCE occurs when P_{in} is set to be -4 dBm and is summarised for each R_b in Table 5-3. In addition, both Fig. 5-18 and Table 5-3 also show that the PCE of BPSK signals increases as the data rate decreases. PCE values remain over 40% for suitable input powers > -12 dBm for all three data rate cases before the reverse breakdown voltage of the diodes is reached.

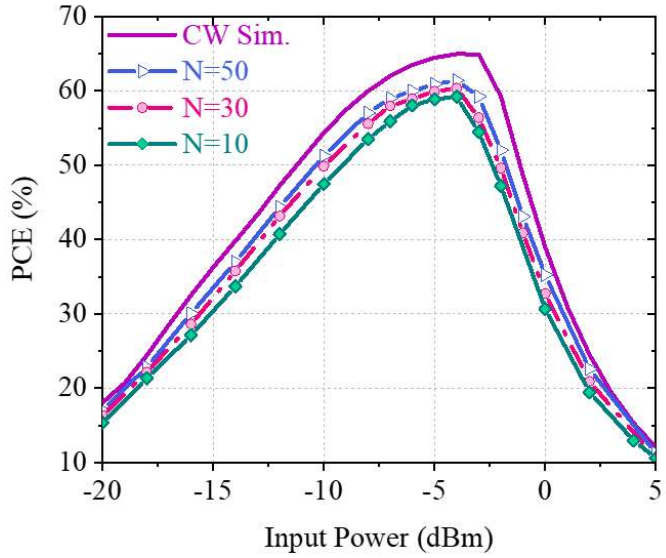

Fig. 5-18: Measured PCEs versus input power level and three data rates for BPSK cases.

Table 5-3: Relation of PCEs versus R_b with the same Input Power Level

N	R_b (Mbps)	Max. PCE (%)
10	245	59.19
30	81.6	60.34
50	49	61.39

The proposed SS splitting technique presented here is a novel solution to the SWIPT receiver. A comparison with some recent reported SWIPT designs is summarised in Table 5-4 where the key parameters such as frequency, input power range, waveform types, PCE, and output voltage are presented for a better evaluation. Overall, the proposed system topology has a relatively high output voltage at low input powers, which can be regarded as good performance. Although PCE in this work is slightly lower than that in [32], a lower input power range (i.e. better power sensitivity) has been achieved in this work.

Table 5-4: Comparison with Other Published SWIPT Systems

Ref.	f (GHz)	P_{in} (dBm)	Waveform Type	Measured PCE (maximum)	Published Year
[30]	2.40	-15 to 20	CW Pulse wave	52% (-8 dBm)	2019
[31]	2.45	-10	PSK	NA	2018
[32]	2.58	6 to 26	CW QPSK	74.9% 67% (10 MHz BW)	2017
This work	**2.45**	**-20 to 5**	**CW BPSK**	**64.6% 59.19~61.39% (N=10/30/50)**	**2020**

(*NA: not available)

5.5.2 IRR Realisation for Recycling Third Harmonics

The fabricated branch-line coupler with two voltage doublers connected to ports P_2 and P_3 is shown in Fig. 5-19 where the packaged Schottky diode SMS7630 is utilised. The antenna is also excluded from this analysis as the goal is again to investigate the ability of the third harmonic recycling receiver topology proposed.

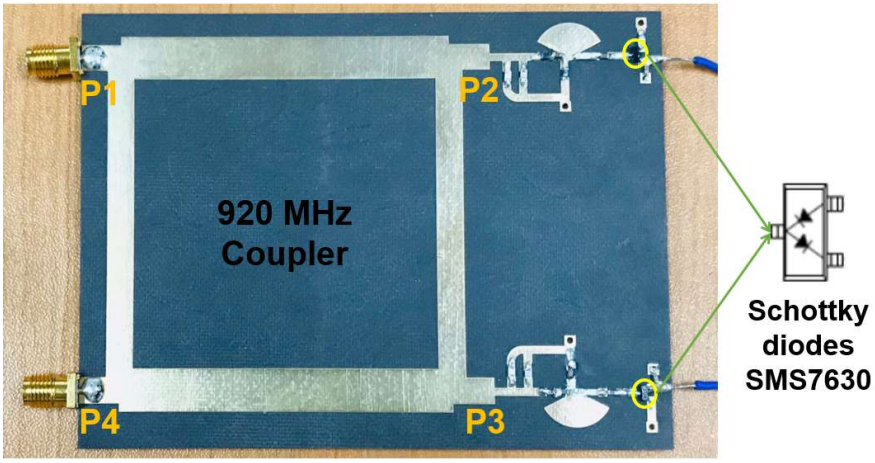

Fig. 5-19: fabricated prototype of the proposed IRR system.

The validation setup is given in Fig. 5-20. The pre-calibrated RF signal generator Keysight EXG-N5173B is connected to port P_1 of the prototype and a Rohde & Schwarz RTO2044 digital oscilloscope is connected to port P_4 to observe the output waveform. A digital multi-meter is used across the load to measure the output DC voltage allowing the PCE to be calculated using Eq. (5.1).

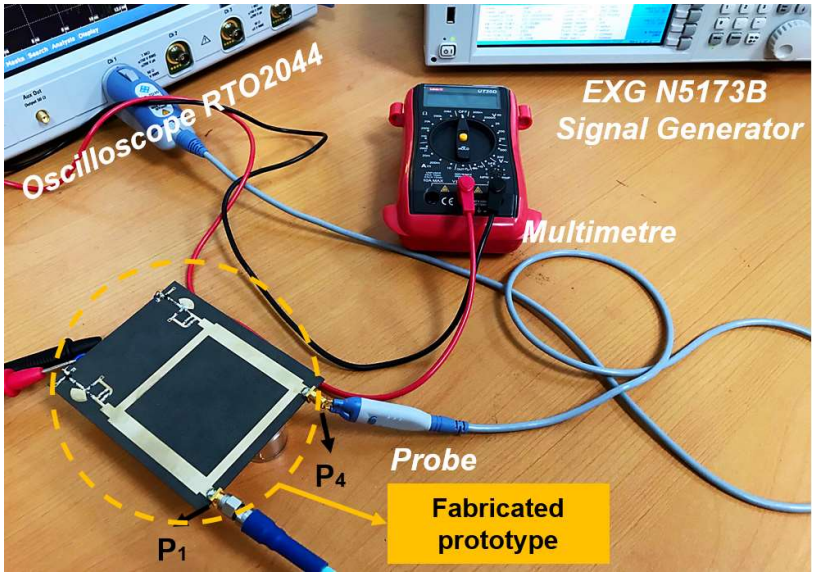

Fig. 5-20: Measurement setup of the fabricated system for validation.

A. Detection of the Third Harmonic

To validate the theoretical deductions about the third harmonic generation and recycling, an incident signal $r(t) = A\cos(2\pi ft)$ with $P_{in} = 0$ dBm is provided to the input port P_1 of the hybrid coupler. Waveforms of the incident signal and the output signal detected from the isolation port of the coupler are presented in Fig. 5-21. This shows that the third harmonic generated from the rectifiers flows back through the branch-line coupler and can be detected at the isolation port P_4. Since the third harmonic is generated from the incident signal, it contains the same modulated information. This provides a solid basis for the application of the ASK modulation scheme and associated data recovery processes at the coupler isolation port for future work.

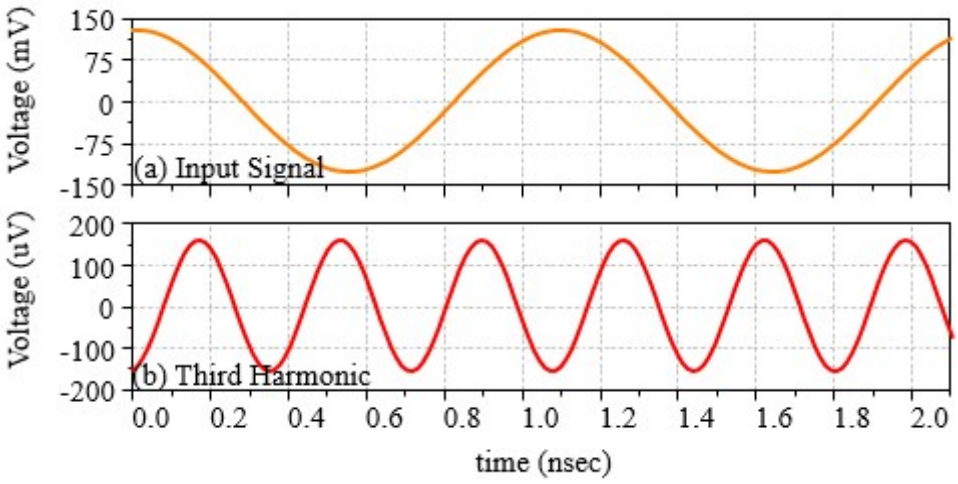

Fig. 5-21: Measured voltage waveforms of (a) the incoming signal and (b) the third harmonic in a transient period.

B. System PCE Performance

The simulated and measured PCE as a function of frequency at three input power levels are given in Fig. 5-22. Overall, the maximum PCE of the proposed topology occurs in the desired frequency band. The maximum simulated PCEs of the proposed topology at the desired frequency band are around 66.5%, 57.4%, and 44.8% when P_{in} is -5 dBm, -10 dBm, and -15 dBm, respectively. The maximum measured PCEs are around 66%, 56%, and 43% for the same input powers, respectively. Therefore, a good agreement between the simulations and measurements is achieved.

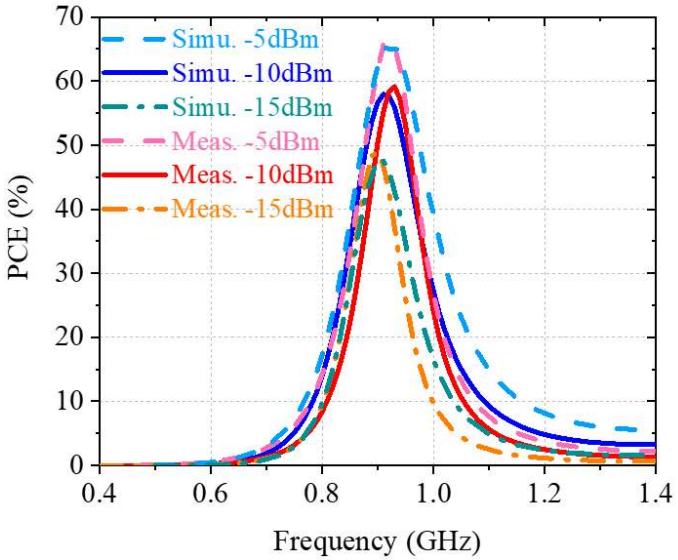

Fig. 5-22: Measured and simulated PCE at three input power levels.

In addition, the simulated and measured PCE versus varying input power levels is shown in Fig. 5-23. The measured PCE is slightly lower than that of the simulated results up to the point where the reverse breakdown voltage of the diodes is reached. Possible reasons may be due to fabrication errors and the unknown parasitic behaviour of the SMD components used in the design. The maximum measured PCE is around 66% when the input power level reaches -5 dBm, which fits the result obtained in Fig. 5-22. PCE increases from around 27% at an input power level of -20 dBm to around 66% at -5 dBm, which illustrates the proposed topology has a good power sensitivity and a relatively good performance over a relatively low range of input powers.

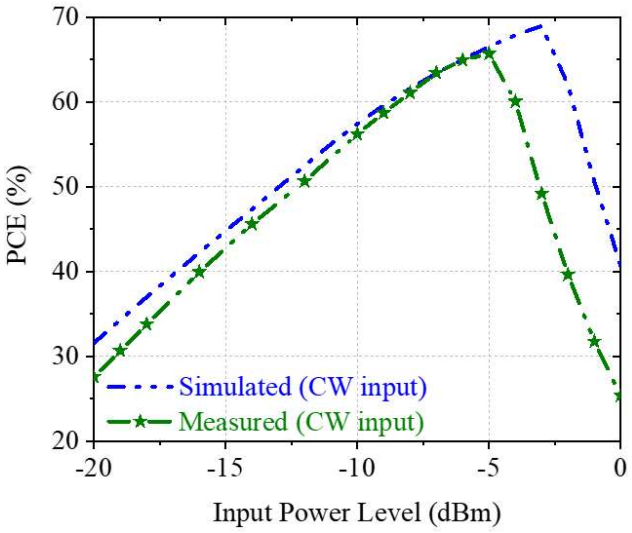

Fig. 5-23: Simulated and measured PCE vs. CW at varying input power levels.

5.6 Summary

This chapter has focused on the development of SWIPT, and two novel receiver hardware implementations have been proposed and demonstrated as viable solutions. The first proposed technique uses symbol splitting (SS). The possibility of extracting data (e.g., phase information) using this technique has been presented, starting with a theoretical analysis. The BPSK modulation type is selected as an example because it is one of the main modulation schemes which has been used for low-rate wireless networks. The proposed splitting idea and the hardware design could be adopted to any modulation types with a spectral response with similar characteristics to BPSK (e.g.,

analogue AM signals are also suitable for the system since the information concentrates on the side bands).

The hardware implementation was fulfilled using a rat-race coupler and a Greinacher rectifier. Overall, experimental investigations support the simulation outcomes. The maximum measured PCE approximates 65% and 60% for CW waves and BPSK signals of varying data rates, respectively. Moreover, the communication capability has been verified by monitoring the information extracted from the isolation port of the rat-race coupler. Data is clearly extractable from the received wave whose voltage amplitude is about half that of the incident wave.

The performance of this IRR has also been evaluated by comparison with other published papers in terms of input power range, waveform types, PCE, and output voltage. The implementation of this system configuration offers several advantages over the conventional circuits for simultaneous wireless power and information transfer, by means of a compact passive circuit topology. The ability to extract information from the received modulated signal for data detection, and a reduction in the loss of the non-information carrying components for energy harvesting, certify that the proposed system design can be adapted as a promising candidate for simultaneous wireless communications and powering for WBAN/WPAN applications.

The second SWIPT receiver was based on recycling the third harmonics generated by the RF rectification for ID. Due to the intrinsic nonlinearity of diodes, high-order harmonics are always generated during rectification. A directional branch-line coupler can pass the incoming fundamental frequency power to the rectifier and then couple the reflected third harmonic signals back to its isolation port. This isolated third harmonic signal carries the same information as is on the originally received signal, just shifted to the higher harmonic frequency.

A branch-line coupler based IRR system has been designed and fabricated for validation. The generation and recycling of third harmonics have been shown through simulation and measurement. The maximum measured PCEs were around 66%, 56%,

and 43% when P_{in} is -5 dBm, -10 dBm, and -15 dBm, respectively. Due to equipment limitations, data detection with modulated signals becomes future work.

5.7 References

[1] Y. Yao *et. al*, "Analysis, design, and implementation of a wireless power and information transmission system using capacitive coupling and double-sided LCC compensation topology," in *IEEE Trans. Industry Applications*, vol. 55, no. 1, pp. 541–551, Jan. 2019.

[2] T. Perera *et. al*, "Simultaneous wireless information and power transfer (SWIPT): recent advances and future challenges," in *IEEE Commun Surveys & Tutorials*, vol. 20, no. 1, pp. 264–302, Dec. 2017.

[3] X. Zhou, R. Zhang, and C. K. Ho, "Wireless information and power transfer in multiuser OFDM systems," in *IEEE Trans. Wireless Commun.*, vol. 13, no. 4, pp. 2282–2294, Apr. 2014.

[4] K. W.Choi, S. I. Hwang, A. A. Aziz, H. H. Jang, J. S. Kim, D. S. Kang, and D. I. Kim, "Simultaneous wireless information and power transfer (SWIPT) for internet of things: novel receiver design and experimental validation," in *IEEE Internet of Things Journal*, vol. 7, no. 4, pp. 2996-3012, Apr. 2020.

[5] I. Krikidis, S. Timotheou, and S. Sasaki, "RF energy transfer for cooperative networks: Data relaying or energy harvesting?" in *IEEE Commun. Lett.*, vol. 16, no. 11, pp. 1772–1775, Nov. 2012.

[6] A. A. Nasir, H. D. Tuan, D. T. Ngo, T. Q. Duong, and H. V. Poor, "Beamforming design for wireless information and power transfer systems: Receive power-splitting versus transmit time-switching," in *IEEE Trans. Commun.*, vol. 65, no. 2, pp. 876–889, Feb. 2017.

[7] N. Janatian, I. Stupia, and L. Vandendorpe, "Joint multi-objective transmit precoding and receiver time switching design for MISO SWIPT systems," in *Proc. IEEE SPAWC*, Jul. 2016, pp. 1–5.

[8] S. Wang, L. Ma, and W. Wu, “Joint TS beamforming and hybrid TS-PS receiving design for SWIPT systems,” in *IEEE Access*, vol 9, pp. 50686-50699, Mar. 2021.

[9] H. Lee, K. J. Lee, H. Kim, and I. Lee, “Joint transceiver optimization for MISO SWIPT systems with time switching,” in *IEEE Trans. Wireless Commun.*, vol. 17, no. 5, pp. 3298–3312, Mar. 2018.

[10] S. Kang, H. Lee, S. Jang, H. Kim, and I. Lee, “Dynamic time switching for MIMO wireless information and power transfer,” in *IEEE Trans. Commun.*, vol. 67, no. 6, pp. 3978-3990, Jun. 2019.

[11] C. Peng *et al.*, “Optimal power splitting in two-way decode-and-forward relay networks,” in *IEEE Commun. Lett.*, vol. 21, no. 9, pp. 2009-2012, Sep. 2017.

[12] D. W. K. Ng, E. S. Lo, and R. Schober, “Wireless information and power transfer: energy efficiency optimization in OFDMA systems,” in *IEEE Trans. Wireless Commun.*, vol. 12, no. 12, pp. 6352–6370, Dec. 2013.

[13] M. Abedi, H. Masoumi and M. J. Emadi, “Power splitting-based SWIPT systems with decoding cost,” in *IEEE Wireless Commun. Lett.*, vol. 8, no. 2, pp. 432-435, Apr. 2019.

[14] D. W. K. Ng, E. S. Lo, and R. Schober, “Robust beamforming for secure communication in systems with wireless information and power transfer,” in *IEEE Trans. Wireless Commun.*, vol. 13, no. 8, pp. 4599–4615, Aug. 2014.

[15] F. Benkhelifa, K. Tourki, and M. S. Alouini, “Proactive spectrum sharing for SWIPT in MIMO cognitive radio systems using antenna switching technique,” in *IEEE Trans. Green Commun. & Networking*, vol. 1, no. 2, pp. 204-222, Apr. 2017.

[16] F. Benkhelifa and M. S. Alouini, “Prioritizing data/energy thresholding-based antenna switching for SWIPT-enabled secondary receiver in cognitive radio networks,” in *IEEE Trans. Cognitive Commun. & Networking*, vol. 3, no. 4, pp. 782-800, Dec. 2017.

[17] R. Zhang and C. K. Ho, “MIMO broadcasting for simultaneous wireless information and power transfer,” in *IEEE Trans. Wireless Commun.*, vol. 12, pp. 1989–2001, May 2013.

[18] P. Lu, X. S. Yang, and B. Z. Wang, “A two-channel frequency reconfigurable rectenna for microwave power transmission and data communication,” in *IEEE Trans. Antennas Propag.*, vol. 65, no. 12, pp. 6976-6985, Dec. 2017.

[19] H. H. Jang, K. W. Choi, and D. I. Kim, “Novel frequency-splitting SWIPT for overcoming amplifier nonlinearity,” in *IEEE Wireless Commun. Lett.*, vol. 9, pp. 826-829, Jun. 2020.

[20] M. Wagih, A. S. Weddell, and S. Beeby, “Rectennas for radio-frequency energy harvesting and wireless power transfer: a review of antenna design,” in *IEEE Antennas Propag. Mag.*, vol. 62, no. 5, pp. 95-107, Oct. 2020.

[21] J. P. Curty, N. Joehl, F. Krummenacher, C. Dehollain, and M. J. Declercq, “A model for u-power rectifier analysis and design,” in *IEEE Trans. Circuits Syst.*, vol. 52, no. 12, pp. 2771–2779, Dec. 2005.

[22] M. Gozel *et al*. “Design of an efficiency-enhanced greinacher rectifier operating in the GSM 1800 band by using rat-race coupler for RF energy harvesting applications,” in *International Journal of RF and Microwave Computer-Aided Engineering*, Dec. 2018.

[23] *Surface Mount Mixer and Detector Schottky Diodes*, Data sheet, Skyworks Solutions, Inc., Jul. 2017.

[24] E. H. Fooks and R. A. Zakarevicius, “Microwave engineering using microstrip circuits,” ISBN: 978-0724809158, Prentice-Hall (Australia), 1999.

[25] D. M. Pozar, Microwave Engineering, Hoboken, NJ, USA: Wiley, 2009.

[26] IEEE Std 802.15.4: IEEE Standard for Low-Rate Wireless Networks, Apr. 2016. [Online]. Available: https://ieeexplore.ieee.org/document/7460875.

[27] Y. Xiao, Z. Du, and X. Zhang, “High-efficiency rectifier with wide input power range based on power recycling,” in *IEEE Trans. on Circuits and Systems II: Express Briefs*, vol. 65, no. 6, pp. 744-748, Jun. 2018.

[28] S. Faruque, “Radio frequency modulation made easy,” URL: https://popularelectronics.technicacuriosa.com/2017/03/08/radio-frequency-modulation-made-easy/

[29] D. M. Cortés-Hernández *et al*., “Extraction of frequency-dependent characteristic impedance and complex permittivity in single-ended and edge-coupled transmission lines using the calculated series parasitic effects,” in *IEEE Trans. Microw. Theory Techn*., vol. 65, no. 9, pp. 3116–3122, Sep. 2017.

[30] G. L. Zhu *et al*, “P. A. Howher, “FSK-based simultaneous wireless information and power transfer in inductively coupled resonant circuits exploiting frequencies splitting,” in *IEEE Access*, vol. 7, pp. 141978-141986, Sept. 2019.

[31] R. Ibrahim *et al.*, “Novel design for a rectenna to collect pulse waves at 2.4 GHz,” in *IEEE Transactions on Microwave Theory and Techniques*, vol. 66, no. 1, pp. 357-365, Jan. 2018.

[32] S. Claessens *et al.*, “Measurement-based analysis of the throughput-power level trade-off with modulated multisine signals in a SWIPT system,” in *ARFTG Microwave Measurement Conference (ARFTG)*, Jun. 2017.

CHAPTER 6. CONCLUSIONS & FUTURE WORK

The purpose of this chapter is to amalgamate all the essential outcomes of this research, to define what has been gained as a result of the work and to show how the aims and objectives originally identified have been addressed in terms of their achievement. Based upon the findings, a discussion of the direction in which this work can be taken forward and where the findings may be applied are presented as future work.

6.1 Conclusions

Driven by the rapid expansion in the use of distributed sensor networks and in particular those used for on- or in-body applications as elements of WBANs or WPANs this thesis has centred on the research and development of sensor and network enabling technologies that can complement or improve current capabilities. Common bottlenecks for the development of WBAN and WPAN devices, in particular for implantable or ingestible devices, are the limited energy provided by their finite energy storage capacity and the limited RF coverage of their antennas for communication and other needs have been identified. In addition, the lack of a miniaturised multi-band and multi-polarisation antenna that can support several simultaneous desirable functions such as data communication and localisation via GPS has also been identified as an area for improvement.

Through the work in this thesis, two novel antennas have been designed. One utilising SRRs to meet the requirements developed through a detailed analysis for an implantable/ingestible antenna. The other one based on a compact crossed dipole structure is able to offer LP and CP spectral bands over an operating bandwidth that covers all licenced bands of interest for WPAN networks. This novel design offers excellent performance for its compact size, comparative to similar antennas published in the literatures.

SWIPT has been identified as the key technology for WBAN/WPAN devices, allowing their operating lifetime to be extended beyond that of the capability of their energy storage capacity. Two new passive receiver architectures have been proposed and realised based on novel splitting techniques to facilitate a high-efficiency SWIPT functionality.

To achieve these contributions the thesis set out by reviewing the state-of-the-art technologies relating to the designs of implantable/ingestible antennas and antennas equipped with tracking capability, as well as current techniques used for SWIPT in Chapter 2. Five requirements, namely operating frequency selection, size miniaturisation, detuning desensitisation for the body environment (through bandwidth enhancement), biocompatibility, and user safety, essential in the design of WBAN antennas were identified and discussed. Moreover, the limitations of current WPAN antennas in relation to these requirements were established, offering an underpinning of the research challenges and needs. Four commonly used splitting techniques for SWIPT were also explained with their merits and demerits discussed, highlighting potential areas for improvement.

For WBAN applications, implantable and ingestible devices for biomedical telemetry have attracted a large amount of research interest. However, most of the published designs fail to satisfy all five requirements with stable and robust performance due to the complex body environment in which they operate. The styles of structures for implantable and ingestible antennas are many and varied. Designing a single antenna that can satisfy all the requirements and is versatile in its use for both implantable and ingestible applications is desirable from both performance and cost perspectives.

A flexible compact loop antenna with SRRs that can operate over multiple bands of interest with good radiation performance has been designed in Chapter 3. A thin layer of a low-loss biocompatible polyamide was wrapped around the outer surface of this antenna to isolate it from body tissues. The working frequency band was from 307 MHz to 3500 MHz, which covers all licensed frequency bands for implantable and ingestible

antennas. This sufficient operational bandwidth which extends beyond the licenced regions allows for the accommodation of any frequency detuning resulting from the dynamically variable operating environment. Hence the antenna retains good and robust performance inside the body environment.

Use of the antenna for ingestible and implantable devices has been examined by evaluating the influence of the material properties of different organs (specifically in the GI tract) and other body tissues such as muscle. Whilst the operating bandwidth of the antenna was maintained the resonant frequencies experience slight shifts as the dielectric properties of the organs vary. Overall, observations indicate that this antenna structure is suitable for application within any region of soft body tissue.

Investigations of using metamaterials (SRRs in this work) were conducted. Improvements in impedance matching, radiation efficiency, and a general decrease in SAR have been realised. Such observations offer beneficial insight into the use of metamaterials on implantable/ingestible antennas.

An upsurge in the trend to equip antennas for WPAN applications with indoor and outdoor location tracking functionality has been witnessed in recent years. The main challenges for this include providing a sufficient AR beamwidth in the GNSS bands and the ability to communicate data for health monitoring applications with the same antenna. Chapter 4 proposed a novel wideband dual-polarised antenna for medical telemetry and indoor/outdoor localisation. This novel work is the first time an antenna for indoor/outdoor location tracking has been designed with an additional operation band reserved for medical telemetry. This antenna can operate in the WMTS band (1.395 GHz~1.4 GHz) for medical services, the Global Navigation Satellite System (GNSS) L1/E1 band (1.57 GHz) and Global Positioning System (GPS) L5 band (1.17 GHz) for outdoor localisation, and an ISM band (2.45 GHz) for indoor localisation.

The miniaturised dimensions of the antenna designed are $0.25\lambda_0 \times 0.25\lambda_0 \times 0.006\lambda_0$ on FR4 PCB at a freespace wavelength of λ_0=256 mm. The measured operational

bandwidth obtained by the design was from 1.15 GHz to 2.62 GHz, which is wide in comparison to other published works. Simulated and experimental outcomes were in good agreement, which illustrates this design operates with LP radiation at 1.4 GHz for wireless medical telemetry, and CP radiation over 1.17, 1.57, and 2.4 GHz for indoor and outdoor localisation. Meanwhile, the AR beamwidth was 120° which meets the required AR beamwidth for GPS usage. Therefore, this antenna is capable of continuous and integrated communication and tracking for WBAN/WPAN applications.

In Chapter 5 two novel splitting techniques were proposed to achieve SWIPT with compact hardware implementations. The SS technique separates the non-information carrying components from the information-carrying components of the received signal streams with aid of a rat-race coupler with each component then used for EH and ID. The hardware implementation was completed with a rat-race coupler and a Greinacher rectifier. BPSK was selected to validate the proposed idea. The observed waveform at the isolation port of the rat-race coupler only contained the phase changes signifying the data content was preserved and could be decoded. The measured PCE for EH was around 65% and 60% when CW waves and BPSK waves were applied separately. Overall, experimental investigations support the simulation outcomes, which supported the proposed SS technique.

The other proposed technique took advantage of the unexploited third harmonics generated during the rectification process. Instead of rejecting or suppressing the unavoidable third harmonics generated, they were channelled for data decoding. This was achieved using a branch-line coupler which halves the incident waves to the full-wave rectifier inputs and then couples the reflected third harmonics generated by the rectifier back to its isolation port where data can be detected. Mathematical deduction verified the generation of the third harmonics and practical measurements further confirmed this idea. Overall, practical outcomes for the proposed two splitting techniques in this chapter confirmed the proposed ideas. The two compact hardware implementations are able to passively decouple received signals into the information-

carrying and non-information-carrying spectral components in an efficient manner making them suitable for application in self-sustainable WBAN/WPAN devices.

The elements and technologies developed during this research allow the systems described in Fig. 1-2 and Fig. 1-3 to be realised in a way that would not have been possible using existing published works. The WBAN antenna designed in Chapter 3 can be applied for use in any implantable or ingestible device as it covers all currently licenced frequency bands, operates in all human body environments and is within typical size requirements. In particular, for the system described by Fig. 1-2, the antenna developed in Chapter 4 would satisfy the needs of a network server, providing sufficient bandwidth to communicate with the other devices in the network whilst at the same time being able to offer both indoor and outdoor localisation functionality. Finally, either of the two SWIPT receiver designs could be used at the WBAN device to allow power transfer to be achieved at the same time as communication. Both of the antennas developed offer sufficient bandwidth and bands to allow for such a system to be created.

6.2 Original Contributions

The motivation behind this work was derived from the desire to develop enabling technologies for WBAN and WPAN communications. The contributions of this research to date have been published in two journal papers and two conference papers. These are summarised as follows:

1. A novel flexible compact loop antenna with SRRs for WBAN

A compact loop antenna with SRRs that can operate over multiple bands of interest with good radiation performance has been proposed, designed, and verified through implementation and measurement. The bandwidth achieved was 307 to 3500 MHz which outperforms other antennas in the published work reviewed. A good radiation efficiency performance was achieved, and the radiation pattern of the antenna is near to omnidirectional. Hence this antenna is an excellent candidate for use in implantable or ingestible WBAN applications.

This work has been published in the following places:

Z. Jiang, Z. Wang, M. Leach, Y. Huang, E. G. Lim, J. Wang, and R. Pei, "Wideband loop antenna with split ring resonators for wireless medical telemetry," in *IEEE Antennas Wireless Propag. Lett.*, vol. 18, pp. 1415–1419, Jul. 2019.

2. A novel wideband dual-polarised antenna for WPAN

A crossed dipole-based antenna exploiting elliptical loop elements was designed for WPAN applications offering multi-band, multi- polarisation capabilities. Allowing a single antenna on a device to provide access to GNSS services for outdoor localisation, 2.4 GHz ISM for indoor localisation and a set of other bands appropriate for PAN on which data can be communicated. The novel dipole design utilises a vacant-quarter printed ring to achieve the desired CP behaviour.

Other antennas in the literature for WPAN applications do not offer such an overall wide bandwidth and AR bandwidth with such a compact size. They either focus on providing CP for localisation or data communication but not both and do not meet the beamwidth requirements for GPS application. These abilities make this antenna an excellent choice for WPAN applications in comparison to other works.

This work has been submitted for publication in the following places:

Z. Jiang, Z. Wang, M. Leach, Y. Huang, E. G. Lim, J. Wang, and R. Pei, "A compact dual polarised antenna for WPANs with indoor/outdoor localisation," under review in *IEEE Access*, Apr. 2020.

3. A novel symbol-splitting technique for SWIPT

Traditional SWIPT methods used to provide data and power to distributed sensors and devices employ a splitting mechanism to separate the received signal into two parts. There are immediate inefficiencies in all of the methods employed as the received signal content is not divided into the data and non-data carrying signal components. For example, in the PS method, the signal is divided by a power ratio. This means that when

demodulating the data from the ID stream, the power contained in this signal is automatically wasted. Here a novel splitting method based around dividing the received signal by spectral component function allows almost all of the power carrying components to be used for energy harvesting, whilst data components are detected which could be demodulated to obtain the communicated information.

To achieve this novel splitting process a novel hardware implementation that makes use of the common rat-race coupler has been developed. Modelling and measurement of the system design confirm the feasibility of such a receiver to achieve SWIPT and the power transfer efficiencies achieved are comparable to other published works at comparable data rates. This technique and implementation provide an excellent alternative, choice to accomplishing SWIPT functionality for typical distributed sensors and devices in WBANs and WPANs based on a compact simple receiver design.

This work has been published in the following places:

Z. Jiang, Z. Wang, M. Leach, E. G. Lim, H. Zhang, R. Pei, and Y. Huang, "Symbol-splitting-based simultaneous wireless information and power transfer system for WPAN applications," in *IEEE Microw. and Wireless Compon. Lett.*, vol. 30, no. 7, pp. 713–716, Jul. 2020.

Z. Jiang, Z. Wang, M. Leach, E. G. Lim, and Y. Huang, "Modelling and performance analysis of an efficient compact integrated rectifier-receiver for SWIPT," in *2020 IEEE MTT-S International Microwave Workshop Series on Advanced Materials and Processes for RF and THz Applications (IMWS-AMP)*, Jul. 2020. DOI: 10.1109/IMWS-AMP49156.2020.9199660.

4. A novel third harmonic recycling technique for SWIPT

A second novel SWIPT splitting mechanism has been developed and a hardware implementation has been designed and tested. In this case, the third harmonic unavoidably generated by the rectifier, a required component of any power transfer system, is recycled rather than suppressed or rejected as it is shown to contain the

modulated data in the received signal. This third harmonic can, if appropriately isolated, be demodulated to provide the communication data.

The theoretical basis for this process and a passive hardware implementation again based on a common RF component, the branch-line coupler, is developed to provide the desired SWIPT functionality. Once again, the modelling and measurement of an optimised circuit design show the feasibility of the technique. The measurements show that comparable power transfer efficiencies to other methods in the literature are attainable. This technique and implementation provide an excellent alternative to accomplishing SWIPT functionality for typical distributed sensors and devices in WBANs and WPANs based on a compact simple receiver design

This work has been published in the following places:

Z. Jiang, Z. Wang, M. Leach, E. G. Lim, H. Zhang, and Y. Huang, "Simultaneous wireless power transfer and communications by recycling third harmonics for WPAN applications," in *2020 IEEE MTT-S International Microwave Workshop Series on Advanced Materials and Processes for RF and THz Applications (IMWS-AMP)*, Jul. 2020. DOI: 10.1109/IMWS-AMP49156.2020.9199669.

6.3 Future Work

Outcomes presented throughout this thesis have highlighted the novelty and value of the research undertaken. Considering the limitations of the current work, some future research directions have been indicated throughout the thesis and are considered in more detail here as follows:

1. Biocompatible structures for ingestible/implantable antennas

As discussed in Chapter 3, any antenna used inside the human body needs to be biocompatible with the body tissues. In this work, to achieve biocompatibility, an additional coating is applied to the antenna to isolate the non-biocompatible materials from the human body. Whilst the antenna achieves comparable performance with and

without the coating, this is an extra potentially unnecessary manufacturing step and could be avoided with a different selection of materials for the antenna structure.

A full investigation of available biocompatible substrates (such as Al_2O_3 ceramic) and conductive materials (such as silver palladium Ag-Pd) could be made, and optimised designs produced and tested. If comparable performance can be obtained using such materials with lower manufacturing costs, these would offer a sensible alternative to the current design.

2. Metamaterials for bio-applications

The current work has only investigated the use of SRRs in reducing electric field strength and enhances radiation efficiency by reducing SAR. However, CSRRs or other metamaterial structures have not yet been explored in this manner. The potential of these structures to positively influence the characteristics of antenna designs for in-body applications could be investigated regarding the five requirements set out in Chapter 2.

3. Reflective metasurfaces for on-body antenna applications

The WPAN antenna presented in Chapter 4 provides excellent performance for off-body devices but has not been optimised for use in on-body applications. To realise on-body functionality, the radiation directed towards the body should be either reflected or absorbed over a short distance from the antennas radiating planes to maximise useful out of body radiation and minimise SAR effects. Such functionality could be achieved through the application of metasurfaces such as electrical band gap (EBG) designs, artificial magnetic conductor (AMC) surface designs or high impedance surface (HIS) designs. These have been used together with other on-body LP antenna designs but could also be adaptable to the antenna designed for this work. Hence an investigation of these types of surfaces as reflectors could prove an invaluable addition to this antenna's operating characteristics and therefore expand its potential application.

4. Data recovery for the novel SWIPT mechanisms developed

For the two SWIPT mechanisms developed in Chapter 5, full receiver realisations should be developed that can provide demodulation of the modulated data stream components isolated. In both the SS and third harmonic techniques, the ability of the hardware implementation to separate power components and data components has been demonstrated; however, the integrated demodulation of the received data has not been realised. In each case, an appropriate modulation scheme that works with the SWIPT mechanism should be paired with an appropriate demodulator integrated into the SWIPT receiver to fully realise the SWIPT system.